

Integrated Fabry-Perot Optical Space Switches

Michaël Ménard

Department of Electrical and Computer Engineering
McGill University
Montréal, Québec, Canada
July 2009

A thesis submitted to McGill University in partial fulfillment of the requirements
of the degree of Doctor of Philosophy

© Michaël Ménard, 2009

Abstract

As information technologies are adopted by more people to accomplish a greater variety of tasks, the need for optical telecommunication networks with higher capacity and flexibility grows. In addition to improving throughput by increasing transmission rates and the number of wavelength channels, novel network architectures using optical burst or packet based switching are investigated because they allow a more efficient use of transmission capacity and they enable the reorganisation of wavelength connections according to traffic demands. The implementation of such networks requires fast, broadband, transparent, and scalable optical space switches. Although research on optical space switches has been on going for decades, no solution that meets all of the above requirements has been reported yet. The work presented in this thesis introduces a novel optical space switch configuration based on tuneable integrated Fabry-Perot filters working at oblique incidence and investigates their performance.

A design method to implement this new switch concept is described and demonstrated with the fabrication and characterisation of optical prototypes. The prototypes are implemented in GaAs/AlGaAs planar waveguides and they are designed to be operated using the electro-optic effect. Deep etching is used to create the switch features and a comprehensive optimization of the waveguide structure is conducted to minimize radiation losses. To maximize the number of wavelength channels that can be controlled with a small refractive index modulation, the switches have a 200 GHz comb frequency response that transmits/reflects one out of every two channels on the ITU 100 GHz grid. Thus, shifting their frequency response by one channel spacing is sufficient to change the state of every channel. Furthermore, four Fabry-Perot cavities are coupled to obtain a flat and wide theoretical passband of more than 50 GHz. A Gaussian beam propagation analysis is performed to determine the minimum beam waist required to avoid distortion. Wavelength response measurements and bit error rate tests at 10 Gb/s are presented. To assess the scalability of this switch design, crossbar and shuffle Beneš layouts were optimized.

Sommaire

Alors que de plus en plus de gens utilisent les technologies de l'information pour accomplir une variété croissante de tâches, le besoin pour des réseaux de télécommunication optique plus flexibles et de plus grande capacité est grandissant. En plus d'augmenter la vitesse de transmission et le nombre de canaux disponibles, de nouvelles architectures utilisant la commutation optique par rafale ou par paquet sont en développement puisqu'elles permettent une utilisation plus efficace de la capacité de transmission et qu'elles rendent possible la réorganisation du réseau en fonction des variations des demandes de service. L'implémentation de tels réseaux nécessite des commutateurs optiques rapides, transparents, à large bande et extensibles. Bien que la recherche sur les commutateurs optiques est cours depuis des décennies, aucune des solutions proposées jusqu'à maintenant ne possède toutes ces qualités. Le travail présenté dans cette thèse décrit une nouvelle configuration de commutateurs optiques utilisant des filtres Fabry-Perot intégrés et accordables qui fonctionnent à incidence oblique et explore leur performance.

L'approche utilisée pour concevoir ce nouveau commutateur est expliquée et démontrée par la fabrication et la caractérisation de prototypes optiques. Ces prototypes sont construits dans un guide d'onde planaire en arsenic de gallium et ils sont conçus pour être opérés à l'aide des effets électro-optiques. De profondes gravures sont utilisées pour créer les composantes du commutateur et une étude sur l'optimisation de la structure du guide d'onde est faite dans le but de minimiser les pertes par radiation. Afin de maximiser le nombre de canaux opérables avec une faible modulation de l'indice de réfraction, les commutateurs possèdent une réponse en peigne espacée de 200 GHz qui transmet/réfléchit un canal sur deux de la grille de 100 GHz de l'ITU. Donc, il est seulement nécessaire de déplacer la réponse du filtre par l'équivalent de l'espacement entre deux canaux afin de pouvoir modifier l'état de n'importe quel canal. De plus, quatre cavités Fabry-Perot sont couplées pour obtenir une bande passante plate et large qui peut en théorie dépasser 50 GHz. Une limite pour la largeur minimum d'un faisceau gaussien qui permet d'éviter au filtre de causer de la distorsion est

établie. Des mesures de la réponse en fréquence et du taux d'erreur sur les bits à 10 Gb/s du commutateur sont présentés. Afin de déterminer l'extensibilité du nouveau commutateur, des matrices basées sur l'architecture en barres croisées et Beneš sont conçues.

Acknowledgements / Remerciements

First and foremost I want to thank my supervisor Professor Andrew G. Kirk for giving me the opportunity to pursue graduate studies. He gave me the freedom to carry on research in my own way yet he was always available to provide guidance and support when required. He also took time to consider my ideas and suggestions regarding every aspect of research.

The fabrication of the devices presented in this thesis would not have been possible without the support of Donald Berry, Dr Matthieu Nannini, and Dr Aju Jugessur who taught me how to use the tools of the microfab. The aluminum sputtering recipe was provided by Dominique Lemoine. I also want to acknowledge the help of Professor Lawrence R. Chen and of Dr Pegah Seddighian with the testing of the devices.

Over the years I made many friends amongst the graduate students in Electrical Engineering who, although they were not directly involved in this research project, contributed through technical advices and more importantly moral support. Rhys Adams, Cristina Marinescu, Frédéric Thomas-Dupuis, Jean-Philippe Thibodeau, Éric Bisailon, Madeleine Mony, Dominik Pudo, Frédéric Nabki, Colin Alleyne, Lidija Malic, Christian Habib, Reuven Gordon, Zeeshan Khalid, Nicolas Bélanger, and all the others with whom I had the chance to work along during my time at McGill: thank you, it has been a fun and rewarding experience. Furthermore, the Photonic Systems Group is a great environment to do research in and that is due to the close collaboration of all the professors involved in the group. Another important factor of the group success is the great work accomplished by Christopher Rolston who takes care of all that is not directly related to research but that must be done.

The support and advices of Amy Beierholm during the time I spent in grad school was much appreciated. Having the opportunity to share about life as a grad student with someone going through the same experience at a different institution was very helpful and motivating.

Finale­ment, je désire remercier sincère­ment ceux qui m'ont per­mit de me rendre jus­qu'ici: mes pa­rents, Ray­monde Breton et Marcel Mé­nard, qui m'ont ap­puyé sans ré­serve dans mes am­bitions aca­démiques. Je suis aus­si redevable à mes amis Patrick-Alexandre Gilbert, Francis Pichette et David Émond qui depuis l'en­fance sont à la fois ma mo­ti­va­tion pour aller de l'avant et ceux qui m'aide à garder l'équilibre.

This work has received financial support from the National Sciences and Engineering Research Council (NSERC) of Canada through the Agile All-pho­tonic Network (AAPN) strategic research initiative, the Idea to Innovation (I2I) program, and the eMPOWER program. Le Fonds Québécois de la recherche sur la nature et les technologies (FQRNT) provided funding through its graduate scholarship programs. The Canadian Microsystem Corporation (CMC) subsidized the GaAs wafers, which were fabricated by the Canadian Photonics Fabrication Centre (CPFC).

Table of Contents

CHAPTER 1: INTRODUCTION.....	1
1.1 WHY OPTICAL SPACE SWITCHING?	1
1.2 THE AGILE ALL-PHOTONIC NETWORKS RESEARCH INITIATIVE.....	4
1.3 INTEGRATED FABRY-PEROT OPTICAL SPACE SWITCHES.....	7
1.4 ORIGINAL CONTRIBUTIONS.....	11
1.5 THESIS ORGANIZATION.....	12
REFERENCES	13
CHAPTER 2: OPTICAL SPACE SWITCH TECHNOLOGIES.....	15
2.1 INTRODUCTION	15
2.2 MEMS SWITCHES.....	16
2.3 THERMO-OPTIC SWITCHES	18
2.4 ELECTRO-OPTIC SWITCHES	21
2.5 SEMICONDUCTOR OPTICAL AMPLIFIER SWITCHES.....	28
2.6 RESONATOR BASED SWITCHES	30
2.6.1 <i>Fabry-Perot Switches</i>	31
2.6.2 <i>Micro-ring Resonator Switches</i>	32
2.7 CONCLUSION.....	34
REFERENCES	37
CHAPTER 3: DESIGN CHALLENGES IN INTEGRATED FABRY- PEROT OPTICAL SPACE SWITCHES.....	47
3.1 INTRODUCTION	47
3.2 WORKING PRINCIPLES	48
3.3 DESIGN CHALLENGES	49
3.4 CONCLUSION.....	52
CHAPTER 4: PLANAR WAVEGUIDE OPTIMIZATION.....	53
4.1 INTRODUCTION	53
4.2 SIMULATION TECHNIQUE.....	54
4.3 RESULTS AND ANALYSIS.....	56
4.4 CONCLUSION.....	62
REFERENCES	63
CHAPTER 5: INTEGRATED OFF-AXIS FABRY-PEROT FILTER DESIGN	65
5.1 INTRODUCTION	65
5.2 FILTER REQUIREMENTS.....	66
5.3 FILTER DESIGN	67
5.4 IMPACT OF FABRICATION CONSTRAINTS.....	72
5.5 BEAM PROPAGATION IN INTEGRATED OFF-AXIS FILTERS	74
5.6 COMPARISON WITH EXPERIMENTAL RESULTS	78
5.7 CONCLUSION.....	79
REFERENCES	81

CHAPTER 6: OPTICAL PROTOTYPE LAYOUT AND CHARACTERISATION.....	83
6.1 INTRODUCTION	83
6.2 PROTOTYPE LAYOUT	84
6.2.1 <i>Planar Waveguide</i>	84
6.2.2 <i>Input and Output Channel Waveguides</i>	86
6.2.3 <i>Collimating Mirrors</i>	87
6.2.4 <i>Filter</i>	90
6.3 PROTOTYPE CHARACTERIZATION	91
6.3.1 <i>Wavelength Response</i>	93
6.3.2 <i>Transmission Experiments</i>	100
6.4 CONCLUSION.....	104
REFERENCES	105
CHAPTER 7: SCALABILITY ANALYSIS.....	107
7.1 INTRODUCTION	107
7.2 POSSIBLE SWITCH FABRIC LAYOUTS	107
7.3 OPTIMISATION TECHNIQUE AND RESULTS	108
7.4 DESIGN TRADE-OFFS.....	110
7.5 CONCLUSION.....	113
REFERENCE.....	113
CHAPTER 8: CONCLUSION.....	115
8.1 SUMMARY.....	115
8.2 COMPARISON WITH EXISTING TECHNOLOGIES.....	117
8.3 FUTURE WORK	119
REFERENCES	122
APPENDIX A: 1-D GAUSSIAN BEAM WAIST VS. FILTER ANGULAR SPECTRUM.....	123
A.1 INTRODUCTION	123
A.2 BEAM WAIST AND ANGULAR SPECTRUM.....	123
A.3 FRACTION OF POWER IN AN GIVEN ANGULAR RANGE	125
REFERENCES	126
APPENDIX B: FABRICATION PROCESS.....	127
B.1 INTRODUCTION	127
B.2 PHOTOMASKS.....	127
B.3 FABRICATION PROCESS.....	133
REFERENCES	134

List of Figures

FIG. 1.1: AGILE ALL-PHOTONIC NETWORK STAR TOPOLOGY	6
FIG. 1.2: SCHEMATIC OF A SIMPLE 2X2 OPTICAL SPACE.....	7
FIG. 1.3: SCHEMATIC ILLUSTRATING THE OPERATION OF AN INTEGRATED FABRY- PEROT OPTICAL SPACE SWITCH WITH THE ELECTRO-OPTIC EFFECT	9
FIG. 1.4: ILLUSTRATION OF AN ELECTRO-OPTIC COMB FABRY-PEROT SWITCH RESPONSE.....	9
FIG. 1.5: WAVELENGTH TRANSMISSION RESPONSE FOR FABRY-PEROT FILTERS WITH A SINGLE CAVITY AND WITH MULTIPLE COUPLED CAVITIES.....	10
FIG. 2.1: TYPICAL LAYOUT FOR 2-D AND 3-D MEMS SWITCHES USING MICRO- MIRRORS	17
FIG. 2.2: SCHEMATIC OF THE MOST COMMON THERMO-OPTIC SWITCH CONFIGURATIONS.....	20
FIG. 2.3: PLANAR ELECTRO-OPTIC SWITCH CONFIGURATIONS	25
FIG. 2.4: SCHEMATICS OF DIRECTIONAL COUPLER SWITCHES	27
FIG. 2.5: SEMICONDUCTOR OPTICAL AMPLIFIER 4X4 SWITCH FABRICS.....	30
FIG. 2.6: FREE-SPACE FABRY-PEROT SWITCH SCHEMATICS.	32
FIG. 2.7: SCHEMATICS OF MICRO-RING SWITCHES	33
FIG. 3.1: SCHEMATIC OF THE INTEGRATED FABRY-PEROT OPTICAL SPACE SWITCH	48
FIG. 4.1: VARIABLES USED IN THE PLANAR WAVEGUIDE OPTIMIZATION.....	54
FIG. 4.2: RADIATION LOSS VS. REFRACTIVE INDEX CONTRAST AND WAVEGUIDE CORE THICKNESS.....	57
FIG. 4.3: OPTIMUM TOP CLADDING THICKNESS VS. REFRACTIVE INDEX CONTRAST AND WAVEGUIDE CORE THICKNESS	58
FIG. 4.4: TWO INTENSITY PROFILES WITH THE SAME $1/e^2$ WIDTH AND THEIR ANGULAR SPECTRUM.....	59
FIG. 4.5: MINIMUM RADIATION LOSSES VS. ETCH DEPTH FOR A FIRST ORDER TRENCH.....	60
FIG. 4.6: MINIMUM RADIATION LOSSES VS. TRENCH WIDTH FOR DIFFERENT ETCH DEPTH.	60
FIG. 4.7: RADIATION LOSSES VS. ETCH DEPTH FOR THE OPTIMUM WAVEGUIDE CONFIGURATIONS.....	61
FIG. 5.1: SCHEMATIC OF A 3X3 SWITCH WITH TUNEABLE COUPLED CAVITY FABRY- PEROT FILTERS IN A CROSSBAR CONFIGURATION.	66
FIG. 5.2: NORMALIZED TRANSMISSION RESPONSE OF THE FILTER AS A FUNCTION OF THE ERROR IN TRENCH WIDTH	69
FIG. 5.3: TRANSMISSION RESPONSE AND CHROMATIC DISPERSION FOR FILTERS WITH DIFFERENT MIRROR REFLECTIVITY CALCULATED WITH THE TMM.....	71
FIG. 5.4: WAVELENGTH RESPONSE IN TRANSMISSION AND REFLECTION FOR FILTERS WITH FIRST AND SECOND ORDER MIRRORS.	73
FIG. 5.5: SCHEMATIC SHOWING GAUSSIAN BEAM PROPAGATION IN AN INTEGRATED FABRY-PEROT FILTER	75
FIG. 5.6: TRANSMISSION EFFICIENCY VS. WAVELENGTH FOR INPUT BEAMS WITH DIFFERENT FRACTIONS OF THEIR ANGULAR SPECTRUM WITHIN THE CLEAR BANDWIDTH OF THE FILTER ANGULAR SPECTRUM.....	75

FIG. 5.7: MINIMUM $1/e$ GAUSSIAN BEAM WIDTH FOR UNDISTORTED PROPAGATION THROUGH THE FOUR CAVITY FILTER.....	77
FIG. 5.8: PROTOTYPE WAVELENGTH RESPONSE MEASURED EXPERIMENTALLY AND SIMULATED WITH THE EIGENMODE EXPANSION	79
FIG. 6.1: PICTURES OF A SWITCH PROTOTYPE.....	85
FIG. 6.2: EXPERIMENTAL RESULTS FROM THE LOSS MEASUREMENTS WITH THE CUT-BACK METHOD.	86
FIG. 6.3: SCHEMATIC ILLUSTRATING THE PARABOLIC MIRROR LAYOUT	89
FIG. 6.4: PICTURE OF A TIR PARABOLIC MIRROR TAKEN WITH VISIBLE LIGHT ILLUMINATION AND WITHOUT EXTERNAL ILLUMINATION.....	89
FIG. 6.5: SCHEMATIC OF THE EXPERIMENTAL SET-UP USED FOR THE WAVELENGTH RESPONSE MEASUREMENTS.	92
FIG. 6.6: PICTURE SHOWING A SWITCH PROTOTYPE ON A CUSTOM HOLDER.....	92
FIG. 6.7: MEASURED WAVELENGTH RESPONSE OF THE FIRST PROTOTYPE.	94
FIG. 6.8: MEASURED WAVELENGTH RESPONSE OF THE SECOND PROTOTYPE	94
FIG. 6.9: EXPECTED WAVELENGTH RESPONSE FOR THE SWITCH PROTOTYPE	95
FIG. 6.10: PICTURES OF A FILTER TAKEN WITH VISIBLE LIGHT ILLUMINATION AND WITH INFRARED LIGHT TRANSMITTED OR REFLECTED BY THE FILTER.....	96
FIG. 6.11: FIRST PROTOTYPE WAVELENGTH CHANNEL PERFORMANCE.	98
FIG. 6.12: SECOND PROTOTYPE PERFORMANCE.....	99
FIG. 6.13: EXPECTED WAVELENGTH CHANNEL PERFORMANCE.	100
FIG. 6.14: BER MEASUREMENT TEST SETUP.....	101
FIG. 6.15: BIT ERROR RATE CURVES FOR A 10 GB/S SIGNAL REFLECTED AND TRANSMITTED BY THE SWITCH PROTOTYPE	102
FIG. 6.16: EYE DIAGRAMS	103
FIG. 6.17: MEASURED OPTICAL SPECTRA AFTER THE SWITCH AND THE SOA	103
FIG. 7.1: SCHEMATICS OF INTEGRATED FABRY-PEROT SWITCH FABRICS	109
FIG. 7.2: AREA AS A FUNCTION OF FILTER CLEAR BANDWIDTH FOR A 4X4 CROSSBAR SWITCH FABRIC.	111
FIG. 7.3: MINIMUM SWITCH AREA FOR 4X4 CROSSBAR AND SHUFFLE BENEŠ FABRICS VS. THE REFRACTIVE INDEX USED TO IMPLEMENT THE FILTERS.	112
FIG. 8.1: POSSIBLE GAAS EPITAXIAL CONFIGURATIONS TO OBTAIN ELECTRO-OPTIC EFFECTS.	121
FIG. B.1: SCHEMATIC SHOWING THE TWO CENTRAL ROWS OF THE FILTERS PHOTOMASK.....	129
FIG. B.2: SCHEMATIC SHOWING THE FILTER AND CHANNEL WAVEGUIDE MASK PATTERNS FOR A SINGLE DEVICE.	130
FIG. B.3: SCHEMATIC SHOWING THE ELECTRODE, CHANNEL WAVEGUIDES, AND FILTER MASK PATTERN FOR A SINGLE DEVICE.	131
FIG. B.4: SCHEMATIC OF THE ALIGNMENT MARKS USED TO OVERLAY THE PHOTOMASKS	132
FIG. B.5: SCANNING ELECTRON MICROGRAPHS SHOWING THE CROSS-SECTION OF A FILTER MIRROR AND THAT OF A COLLIMATING MIRROR.....	133

List of Tables

TABLE 2.1: PERFORMANCE COMPARISON OF DIFFERENT TYPE OF OPTICAL SPACE SWITCHES.....	36
TABLE 4.1: OPTIMUM GaAs/AlGaAs WAVEGUIDE CONFIGURATIONS VS. TRENCH DEPTH	56
TABLE 5.1: CHARACTERISTICS OF FOUR CAVITY FILTERS AT NORMAL INCIDENCE .	73
TABLE 5.2: DESIGNED AND MEASURED TRENCH WIDTH.....	78
TABLE 6.1: CHARACTERISTICS OF THE FREQUENCY RESPONSE OF THE FABRICATED FILTERS	96
TABLE 6.2: AVERAGE LOSS, CROSSTALK AND EXTINCTION RATIOS OF THE PROTOTYPES. THE VALUES IN PARENTHESIS ARE THE STANDARD DEVIATIONS.	98
TABLE 7.1: SWITCH FABRICS WITH MINIMUM AREA	110
TABLE B.1: VARIATIONS FROM THE DESIGN VALUES OF THE DEVICES ON THE FILTER MASK	130

List of Abbreviations

2-D	Two Dimensional
3-D	Three Dimensional
AAPN	Agile All-photonic Network
AiAs	Aluminum Arsenide
AlGaAs	Aluminum Gallium Arsenide
BCB	Benzocyclobutane
BER	Bit Error Rate
BERT	Bit Error Rate Tester
Cl ₂	Chlorine
CMOS	Complementary Metal-oxide Semiconductor
DC	Directional Coupler
DOS	Digital Optical Switch
DWDM	Dense Wavelength Division Multiplexing
EDFA	Erbium Doped Fibre Amplifier
EO	Electro-optic
FP	Fabry-Perot
FSR	Free-spectral Range
GaAs	Gallium Arsenide
InGaAsP	Indium Gallium Arsenide Phosphide
InP	Indium Phosphide
ITU	International Telecommunication Union
LiNbO ₃	Lithium Niobate
MEMS	Micro-electro-mechanical Systems
Mod	Modulator
MQW	Multiple Quantum Wells
MZI	Mach-Zehnder Interferometer
NSERC	National Sciences and Engineering Research Council
OEO	Optical-electrical-optical
OTDM	Optical Time Division Multiplexing
PC	Polarization Controller
PDL	Polarization Dependent Loss
PECVD	Plasma-enhanced Chemical Vapour Deposition
PLC	Planar Lightwave Circuit
PLZT	Lead-lanthanum-zirconate-titanate
PM	Polarization Maintaining
PPG	Pulse Pattern Generator
QCSE	Quantum-confined Stark Effect
RF	Radio Frequency
ROADM	Reconfigurable Optical Add/Drop Multiplexer
SDH	Synchronous Digital Hierarchy
SF ₆	Sulfur Hexafluoride
SiCl ₄	Silicon Tetrachloride
SiO ₂	Silicon Dioxide
SOA	Semiconductor Optical Amplifier
SOI	Silicon-on-insulator
SONET	Synchronous Optical Network
TE	Transverse Electric
TEC	Thermo-electric Cooler
TIR	Total Internal Reflection
TM	Transverse Magnetic
TMM	Transfer Matrix Method
TO	Thermo-optic
UV	Ultra-violet
WDM	Wavelength Division Multiplexing

Chapter 1

Introduction

1.1 Why Optical Space Switching?

In telecommunications, the advent of semiconductor lasers and optical fibres made light the preferred information carrier on medium and long distances [1, 2]. The wide bandwidth of optical fibres, which in theory could transmit half a billion telephone conversations simultaneously [3], moved the bottlenecks of data transmission to the network nodes. Today, the majority of routing operations necessary to establish connections between nodes are carried out electronically. This requires the conversion of incoming optical signals to electrical ones, which must be converted back to light after processing. This process is referred to as optical-electrical-optical (OEO) switching.

The role of OEO switches goes beyond the simple routing of data: they are used to amplify, retime, and reshape optical signals; they can perform wavelength conversion; they allow data management and performance monitoring at the bit level; and they can perform tasks specific to a transmission protocol, such as data aggregation and synchronization in SDH or SONET networks [4, 5]. This versatility is what makes OEO switches attractive and hard to replace. Nevertheless, the increase in capacity of optical networks, motivated by the ever growing demand generated by novel Internet services [6-8], is constantly increasing the pressure on electronic components. For instance, successful transmission at 100 Gb/s on a single wavelength channel has already been

demonstrated in a field trial [9]. To put that in perspective, in 1992 the aggregate bandwidth for a whole switching office was less than 15 Gb/s [10]. Moreover, the introduction of dense wavelength division multiplexing (DWDM) multiplied the number of electronic processing units required at each node [11]. The combination of high bit rates and increasing number of wavelength channels led to expensive switching systems that require copious amount of power. For example, a fully configured CISCO CRS-1 multi-shelf router can handle up to 1152 line cards running at 40 Gb/s and consumes 0.86 MW of power [8]. This is equivalent to the power generated by a small industrial wind turbine [12].

The development of optical techniques to compensate for signal degradation, such as optical amplifiers and dispersion compensating fibres, extended the reach of optical networks to thousands of kilometres without need for electronic regeneration. This opened the door to the concept of “all-photonic” networks in which optical signals are transmitted between their ingress and egress points without ever being converted to electrical ones.

Before going further, it is necessary to define some terminology since the words optic and photonic are often used interchangeably but they can mean different things to different people [1]. In this work, the terms all-photonic networks and optical switching refers to networks or devices in which data signals always remain in the optical domain but that have electrical control signals. On the other hand, the expression all-optical refers to networks and switches in which light is used for both data and control signals.

The most cited argument for eliminating OEO in optical networks is that all-photonic networks are transparent [1, 4-8, 11, 13, 14], i.e. they can transmit data without knowledge of the bit rate or the protocol used. In theory, this makes all-photonic networks easy and affordable to upgrade because only the electronic components at edge nodes need to be modified to implement new protocols or faster bit rates. However, in practice network transparency is limited by the characteristics of its components [1]. For instance, possible modulation formats

could be limited by the passband of optical filters present in a network. Even if full transparency is not achieved, which could be the case if some OEO is kept to perform traffic grooming or monitoring, introducing optical switching can improve a node performance by increasing its throughput, decreasing its size, power consumption, heat dissipation, and cost [1, 5, 11, 15, 16]. Furthermore, optical switching provides control at the wavelength level, which service providers could take advantage of to offer new services [6]. Therefore, the main motivation for incorporating optical switching in telecommunication networks is to reduce both capital expenditure (by reducing the need for fast electronics) and operational expenditure (by decreasing the transmission cost per bit).

Research in optical switching for telecommunication applications started in the 1970s but it began to attract considerable interest in the late 1980s, after optical fibres were introduced in transmission systems [1]. Despite the numerous potential solutions proposed and investigated, few optical space switching technologies are commercially available today. Those that have reached the market are limited either in their switching speed, such as micro-electro-mechanical (MEMS) devices, or in their port count, such as electro-optic (EO) switches [7]. This thesis investigate a novel optical space switch configuration aimed at combining the scalability of MEMS with the fast switching times of EO switches. The proposed device relies on a tuneable Fabry-Perot filter implemented in a planar waveguide, and its principle of operation and main characteristics are described in section 1.3. However, before providing more details on the switch, it is necessary to define requirements against which the new configurations and existing technologies can be evaluated. This is done in the next section, which explains the context in which the research reported in this thesis was conducted.

1.2 The Agile All-Photonic Networks Research Initiative

Optical networks can be classified into four categories based on their ability to reconfigure their wavelength connections [8, 16]:

- *Static networks* in which wavelength connections are fixed. These include networks that perform routing using exclusively OEO switching.
- *Circuit-switched networks* in which wavelength connections are established between nodes before they begin exchanging information. Such connections require round-trip signaling and the reservation of the resources.
- *Burst switching networks* in which electronic routers at the network edges assemble incoming data into bursts before sending them into the network with a header cell allowing intermediary nodes to route the bursts properly. Once the egress node is reached, the information contained in the burst is disassembled and forwarded to the intended receivers.
- *Packet switching networks* in which packets are sent on the network as soon as they arrive to the ingress node. The main difference between burst switching and packet switching is the speed requirements they impose on header processors and switches. Since there is no data aggregation in packet switching, they need faster processing speeds.

Each of the network types described above has different switching speed requirements. Obviously, static networks do not possess any optical switches and their wavelength paths must be reconfigured manually, which may require days or weeks. Circuit-switched networks maintain their light path for a relatively long time and thus they can be implemented with devices that have milliseconds switching times, such as MEMS and thermo-optic switches (further

details on switching technologies are given in chapter 2). Burst switching networks typically need switches faster than a millisecond whereas packet switching networks have the most stringent requirement since they cannot tolerate switching delays longer than a few nanoseconds [8].

In terms of maturity, static and circuit-switched networks are already commercially available. However, significant technological issues still need to be solved before burst and packet switching networks can be deployed. Burst and packet switching are advantageous because they enable statistical multiplexing since they use resources only when data is being transferred [15, 16]. Thus they can increase the degree of utilisation of wavelength channels by sharing them between multiple users or nodes according to the traffic demands.

To address these challenges, the National Sciences and Engineering Research Council of Canada (NSERC) launched in 2003 the Agile All-Photonic Networks' (AAPN) strategic research network. The work presented in this thesis was supported in part by this research initiative. The AAPN goal was to develop a flexible transparent optical network capable of reconfiguring its light paths in a microsecond. The data transmitted through the network is aggregated in 10 μ s frames and, unlike burst switching networks, a variant of optical time division multiplexing (OTDM) called slot by slot switching is used as a basis for its scheduling algorithm. Synchronization is implemented to avoid contention issues since no optical buffering is available in the network. The decision of excluding optical buffers was motivated by the lack of practical solutions to implement that function in the near future. Wavelength conversions were not included for the same reason. A star topology with a 64x64 optical space switching fabric at its centre (see Fig. 1.1) was chosen for its compatibility with OTDM scheduling and its robustness to various traffic distributions [14].

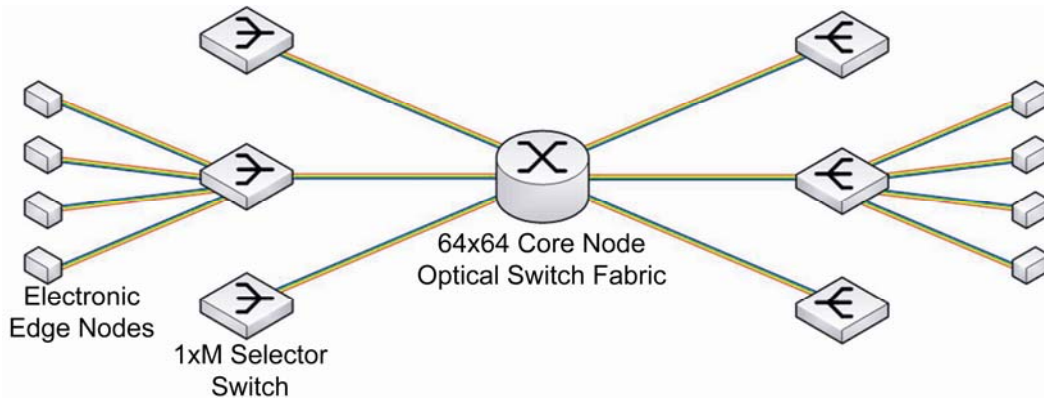


Fig. 1.1: Agile All-Photonic Network star topology (adapted from [17])

In the AAPN, electrical to optical conversions occur only in edge nodes, which also perform all traffic management tasks. A single wavelength is used within the star but multiple stars working at different wavelengths can be overlaid to increase network capacity. To create an efficient network with the topology described above, the core switch must meet the following requirements:

- 64x64 port count
- Switching time less than a microsecond
- Insertion loss below 10 dB
- Low crosstalk and signal distortion (since there is no OEO regeneration)
- Capable of working at multiple wavelengths (for overlaid star topologies)

These requirements served as a starting point to define the research presented in this thesis. They led to a novel optical space switch based on tuneable integrated Fabry-Perot filters used at oblique incidence. The main objective of the investigation conducted here was to determine if these filters could be used to form switch fabrics that are both fast and scalable. Switch fabrics meeting these requirements represent a key enabling technology for the development of the next generation of optical networks.

1.3 Integrated Fabry-Perot Optical Space Switches

A simple optical space switch can be obtained by moving a mirror in and out of the propagation path of a light beam (see Fig. 1.2). However, this requires mechanical movement to modify the direction of propagation of light. The speeds required in optical burst and packet networks are extremely challenging, if not impossible, to achieve with mechanical actuation no matter what is the size of the mirror. Nonetheless, a moveable mirror presents multiple characteristics that are desirable in an optical space switch. First, it creates transparent switch fabrics since reflections of a mirror are not bit rate or modulation dependent. Most mirrors are broadband. Furthermore, they can be low loss and have limited crosstalk with proper beam collimation. Therefore, a device relying on a fast actuation mechanism and that possess the same advantages as a mirror would be an efficient building block for space switch fabrics.

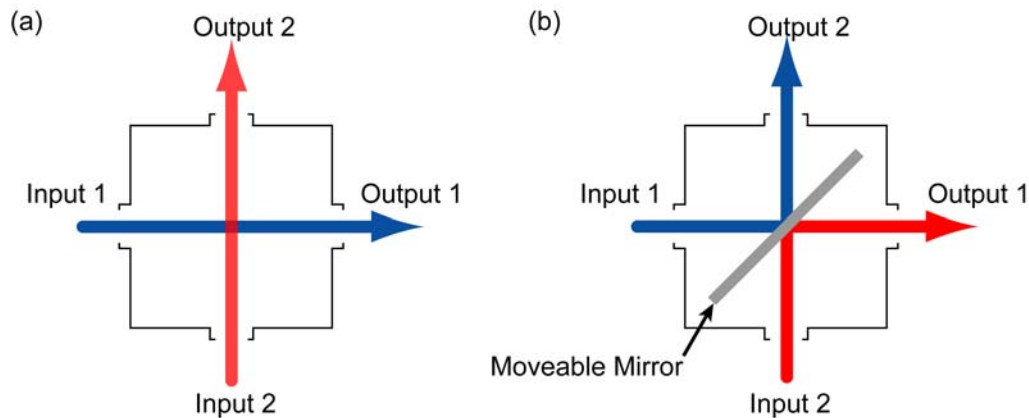


Fig. 1.2: Schematic of a simple 2x2 optical space switch in (a) bar state and in (b) cross state.

The fastest way to control optical beams with electrical signals is to modulate a material refractive index by altering the density or disposition of its charge carriers. Depending on the material used, this can be achieved through a number of phenomena, including electro-optic (EO), Franz-Keldysh, or plasma effects [18], and in certain materials, such as III-V semiconductors, multiple effects can interact [19]. However, the refractive index modulation provided by

these effects is relatively small, especially when those involving an increase in optical absorption are avoided. For the purpose of this project, index modulations obtainable solely with the linear EO effect were considered. The linear EO effect creates a change in refractive index by redistributing bond charges inside a material upon the application of an electric field [20]. Since no extra charges are injected, EO effects do not cause absorption losses and they can be modulated at several gigahertz.

Once the actuation mechanism is chosen, the challenge is to figure out a way to use it to perform space switching in a way that provides the same benefits as those described for a perfect mirror. This is the goal pursued in the development of the optical space switch presented here. In addition to the criteria mentioned above, the switch is expected to work over an entire wavelength band; to provide over 20 dB of crosstalk isolation and extinction ratio; and to be compatible with the 100 GHz ITU grid. Since EO effects are polarization dependent, the switch is designed to work with only one polarization state.

To create the equivalent of a fast moveable mirror, it must be possible to change the device response with the small refractive index change provided by EO effects. Both Bragg mirrors and Fabry-Perot (FP) cavities can be tuned by changing their refractive index. How this can be used to create an optical space switch is illustrated in Fig. 1.3 with an integrated Fabry-Perot filter. Depending on the voltage applied across the filter, it will either transmit or reflect an incident beam. An overview of the salient features of integrated Fabry-Perot optical space switches is given below.

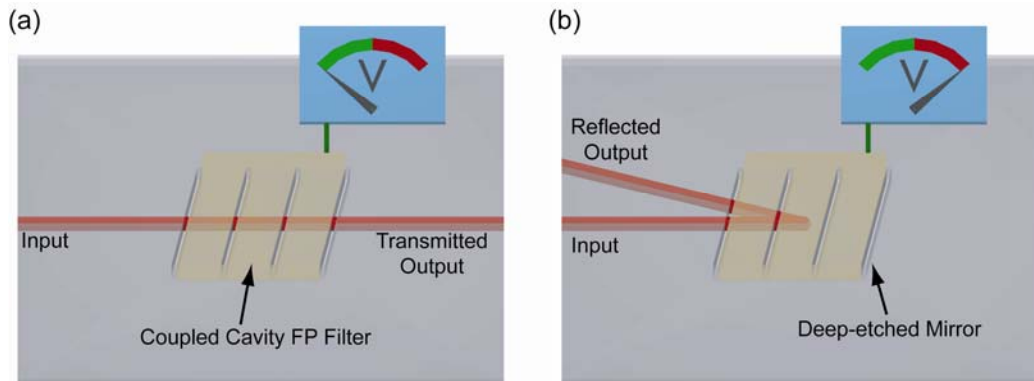


Fig. 1.3: Schematic illustrating the operation of an integrated Fabry-Perot optical Space switch with the electro-optic effect. In (a) no voltage is present and the switch transmits the input beam whereas in (b) a voltage is applied, which modulate the filter refractive index, and the switch reflects the input beam.

The small index change achievable with EO effects allows the tuning of the wavelength response of Bragg mirrors or FP cavities by about only 1 nm. However, that bandwidth can be extended in FP cavities by decreasing their free-spectral range to create a comb response that transmits/reflects one out of every two channels of the grid targeted for the switch (see Fig. 1.4). This way, tuning the FP cavity response by the equivalent of one channel spacing is sufficient to redirect any channels covered by the comb response.

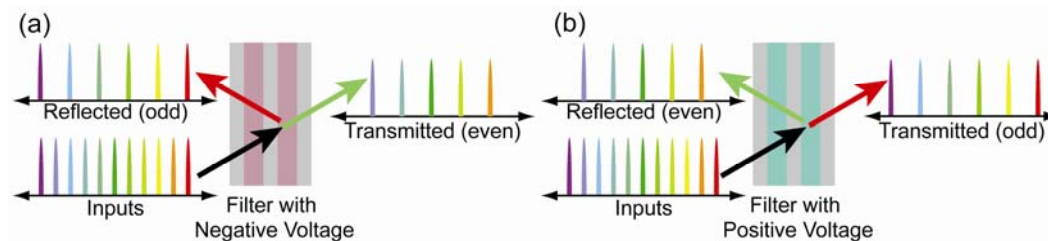


Fig. 1.4: Illustration of an electro-optic comb Fabry-Perot switch response when (a) a negative voltage is applied and (b) when a positive one is applied.

A single high-order FP cavity with mirror reflectivity high enough to form a comb filter with at least a 20 dB contrast between adjacent channels has a Lorentzian wavelength response, as shown in Fig. 1.5. The transmission peaks are very narrow and this can cause distortion in signals modulated at high bit rates. As mentioned above, the ideal wavelength response would be like that of a perfect mirror, which is flat and wide. To increase the passband width, multiple

high-order FP cavities are coupled to form the comb filter. Fig. 1.5 shows an example of the improvement possible with coupled cavities.

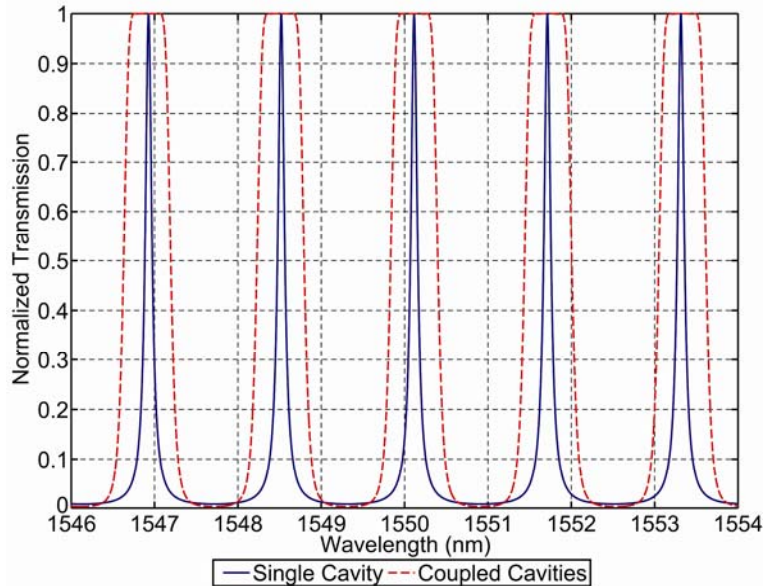


Fig. 1.5: Wavelength transmission response for Fabry-Perot filters with a single cavity and with multiple coupled cavities.

Since EO effects are dependent on the strength of the applied electric field, reducing the volume over which the refractive index must be changed lowers the required voltage. This decreases the power needed to actuate the switch and facilitate the design of the controlling electronics. Therefore, the FP filter is implemented in a planar waveguide to confine light vertically, which reduces the distance between electrodes. The absence of confinement in the horizontal direction simplifies the switch layout since light beams can overlap without suffering losses, as is the case with channel waveguides crossing.

A high index contrast is required to form broadband cavity mirrors, which maximize the bandwidth of the comb filter. This is achieved by deep etching the planar waveguide. However, deep etching eliminates vertical confinement and creates regions where radiation losses can be significant. Thus, the planar waveguide structure must be optimized to limit these losses.

1.4 Original Contributions

The work done over the course of the research project described in this thesis led to the following original contributions. The information in parenthesis indicates the relevant thesis chapters.

- Development of a simulation and optimization methodology for the design of integrated filters with deep-etch features working at oblique incidence. (chapters 3 & 5)
- First study of losses in deep etched waveguides that simultaneously considered the layer structure of the waveguide, its index contrast, and the depth of the etched features. (chapter 4)
- First analysis establishing a lower limit on the Gaussian beam waist required to preserve the plane wave response of integrated coupled cavity Fabry-Perot filters as a function of incidence angle. (chapter 5 and appendix A)
- Design of the first integrated Fabry-Perot optical space switch. (chapter 6)
- First implementation of integrated Fabry-Perot optical space switch prototypes. (chapter 6 and appendix B)
- First characterisation of 2x2 integrated Fabry-Perot optical space switches, including their wavelength response, temperature sensitivity, and their ability to transmit 10 Gb/s data signals. (chapter 6)
- First scalability analysis of integrated Fabry-Perot optical space switch fabrics. (chapter 7)

These contributions are reported in various published and submitted conference proceedings and journal articles, as well as a US provisional patent [21-28].

1.5 Thesis Organization

The remaining of the thesis is organised as follows. Chapter 2 reviews optical space switch technologies that are relevant to this project, either because they share some features with or because they are competing solutions to the design introduced here. In chapter 3, an overview of the design challenges faced during this project is presented along with the solutions that are proposed. Chapter 4 explains the planar waveguide optimization method developed to minimize radiation losses in deep-etched features and shows the results that were obtained. Chapter 5 discusses the filter design and the impact fabrication constraints have on its performance. It also includes the derivation of a lower limit on the input beam waist that maintains the plane wave response of the filter.

In chapter 6, the layout of a 2x2 optical prototype is explained and experimental results of its characterisation are presented. They include its wavelength response; measurements of loss, crosstalk and extinction ratio for 50 channels on the ITU 100 GHz grid; and bit error rate measurements for a 10 Gb/s signals propagating through the prototype switch. Chapter 7 investigates the scalability of integrated Fabry-Perot optical space switch fabrics for both crossbar and shuffle Beneš architectures. Lastly, chapter 8 concludes with an analysis comparing integrated Fabry-Perot optical space switches with other switch implementations and discusses future work and possible improvements.

References

- [1] T. S. A. El-Bawab, "Preliminaries and Terminologies," in *Optical switching* Boston: Springer, 2006, pp. 3-35.
- [2] J. E. Midwinter, "Photonics in Switching-the Next 25 Years of Optical Communications," *IEE Proc-J*, vol. 139, no. 1, pp. 1-12, Feb. 1992.
- [3] L. Thylen, G. Karlsson, and O. Nilsson, "Switching technologies for future guided wave optical networks: Potentials and limitations of photonics and electronics," *IEEE Commun. Mag.*, vol. 34, no. 2, pp. 106-113, Feb. 1996.
- [4] H. S. Hinton, *An introduction to photonic switching fabrics*. New York: Plenum Press, 1993.
- [5] R. Izmailov, S. Ganguly, T. Wang, Y. Suemura, Y. Maeno, and S. Araki, "Hybrid hierarchical optical networks," *IEEE Commun. Mag.*, vol. 40, no. 11, pp. 88-94, Nov. 2002.
- [6] B. Hirotsaki, K. Emura, S. Hayano, and H. Tsutsumi, "Next-generation optical networks as a value creation platform," *IEEE Commun. Mag.*, vol. 41, no. 9 pp. 65-71, Sep. 2003.
- [7] M. J. Potasek, "All-optical switching for high bandwidth optical networks," in *Optical Networks Magazine*. vol. 3, no. 6, pp. 30-43, Nov. 2002.
- [8] S. J. B. Yoo, "Optical Packet and Burst Switching Technologies for the Future Photonic Internet," *J. Lightwave Technol.*, vol. 24, no. 12, pp. 4468-4492, Dec. 2006.
- [9] P. J. Winzer, G. Raybon, S. Haoyu, A. Adamiecki, S. Corteselli, A. H. Gnauck, D. A. Fishman, C. R. Doerr, S. Chandrasekhar, L. L. Buhl, T. J. Xia, G. Wellbrock, W. Lee, B. Basch, T. Kawanishi, K. Higuma, and Y. Painchaud, "100-Gb/s DQPSK Transmission: From Laboratory Experiments to Field Trials," *J. Lightwave Technol.*, vol. 26, no. 20, pp. 3388-3402, Oct. 2008.
- [10] H. S. Hinton, "Switching to Photonics," *IEEE Spectrum*, vol. 29, no. 2, pp. 42-45, Feb. 1992.
- [11] G. I. Papadimitriou, C. Papazoglou, and A. S. Pomportsis, "Optical switching: Switch fabrics, techniques, and architectures," *J. Lightwave Technol.*, vol. 21, no. 2, pp. 384-405, Feb. 2003.
- [12] Vestas Wind Systems A/S, *V52-850 kW: The turbine that goes anywhere*, 2009.
- [13] P. E. Green, "Optical networking update," *IEEE J Sel. Areas Comm.*, vol. 14, no. 5, pp. 764-779, Jun. 1996.
- [14] L. Mason, A. Vinokurov, N. Zhao, and D. Plant, "Topological design and dimensioning of Agile All-Photonic Networks," *Comput. Netw.*, vol. 50, no. 2 pp. 268-287, Feb. 2006.
- [15] T. S. A. El-Bawab, A. Agrawal, F. Poppe, L. B. Sofman, D. Papadimitriou, and B. Rousseau, "The Evolution to Optical-switching-based Core Networks," in *Optical Networks Magazine*. vol. 4, no. 2, pp. 7-18, Mar. 2003
- [16] J. P. Jue, W. H. Yang, Y. C. Kim, and Q. Zhang, "Optical packet and burst switched networks: a review," *Iet Commun.*, vol. 3, no. 3, pp. 334-352, Mar. 2009.
- [17] M. Mony, "Reprogrammable Optical Phase Array," Ph.D. dissertation, Dept. Elect. and Comp. Eng., McGill Univ. Montreal, Canada, 2007.
- [18] M. Fukuda, *Optical semiconductor devices*. New York: Wiley, 1999.
- [19] C. Glingener, D. Schulz, and E. Voges, "Modeling of Optical Waveguide Modulators on III-V Semiconductors," *IEEE J. Quantum Elect.*, vol. 31, no. 1, pp. 101-112, Jan. 1995.
- [20] A. Yariv and P. Yeh, *Optical Waves in Crystals: Propagation and Control of Laser Radiation*, New York: Wiley, 2003.
- [21] A. G. Kirk and M. Ménard, "A Comparison of Beam Deflection Electro-Optic Switches," presented at *Photonics in Switching Sapporo*, Japan, 2008.

- [22] M. Ménard and A. G. Kirk, "Integrated Fabry-Perot Comb Switches: Transmission Experiments and Scalability," submitted to *The 22nd Annual Meeting of the IEEE Photonics Society* Belek-Antalya, Turkey, 2009.
- [23] A. G. Kirk, M. Ménard, E. Bisailon, A. Jafari, and A. Khorshidahmad, "Wavefront Engineering in Integrated Planar Waveguides for Multiplexing and Switching," presented at Photonics North, Québec, Canada, 2009.
- [24] M. Ménard and A. G. Kirk, "On the Application of the Transfer Matrix Method to Integrated Optics Simulations," in *Integrated Photonics Research and Applications*, 2006, Uncasville, CT, p. JWB2.
- [25] M. Ménard and A. G. Kirk, "Broadband Optical Space Switch," U.S. provisional patent, application 60/859,497, filed in 2006.
- [26] M. Ménard and A. G. Kirk, "Broadband Integrated Fabry-Perot Electro-Optic Switch," presented at *Photonics in Switching*, Sapporo, Japan, 2008.
- [27] M. Ménard and A. G. Kirk, "Design of Off-axis Fabry-Perot Filters in Planar Waveguides with Deep-etched Features," submitted to *Opt. Express*, 2009.
- [28] M. Ménard and A. G. Kirk, "Integrated Fabry-Perot Optical Space Switches," submitted to *J. Lightwave Technol.*, 2009.

Optical Space Switch Technologies

2.1 Introduction

Research in optical switching has been on going for several decades, and numerous approaches have been proposed and investigated. The amount of literature on the subject is tremendous and therefore this review is limited to the approaches relevant to the work presented in this thesis. Micro-electro-mechanical and thermo-optic switches are discussed because they are currently the most common technologies deployed in commercial networks. Also, the architectures used for the scalability study reported in chapter 7 are based on the layout of micro-electro-mechanical switches. Electro-optic switches and semiconductor optical amplifier based ones are included because they are promising candidates for the next generation of optical space switches since they can achieve sub-microsecond response times. Lastly, resonator based switches are presented because their operating principles are similar to integrated Fabry-Perot optical space switches. Descriptions of other switch technologies not covered in this review, including acousto-optic, opto-mechanical and liquid-crystal switches, can be found in these references [1-5]. The following sections explain the operating principles, material platforms, and common configurations of the technologies mentioned above. A table compiling the performance of

typical implementations of the different switching technologies is presented in the conclusion along with a discussion of each approach merits and drawbacks.

2.2 MEMS Switches

Micro-electro-mechanical systems (MEMS) are miniature devices fabricated on silicon wafers with processes similar to those employed to build electronic circuits. Moveable micro-mirrors are by far the most common MEMS devices used in optical space switches [5-29]. Other configurations have been proposed, including devices that use diffraction gratings [30], prisms [31], or the displacement of optical fibres [32] to perform switching. However, only switches based on micro-mirrors are discussed here because they are the most mature optical MEMS technology and some have layouts compatible with integrated Fabry-Perot optical space switches.

The first MEMS mirror was fabricated at IBM in 1980 [20] but it took 15 years before research on their use in telecommunication began [17]. Different actuation mechanisms have been demonstrated, including piezoelectric [7], electromagnetic [23, 31], and electro-thermal [26] but electrostatic actuation is the most used [2, 10-12, 14, 16, 18, 22, 24, 29]. Electrostatic forces are created between conductors having different electric potentials. Thus, the position of a MEMS mirror can be adjusted by varying the voltage applied across its electrodes. Electrostatic actuators are advantageous in large port-count switch fabric because they dissipate little power and electrostatic fields are easily shielded with materials commonly used in MEMS fabrication processes. Most MEMS switches have response times between 10 μ s and 10 ms [2].

Optical MEMS switches are often classified in two categories: two-dimensional (2-D) and three-dimensional (3-D) switches. Typical layouts for 2-D and 3-D switches are shown in Fig. 2.1. Two-dimensional switches establish connections between a line of inputs and a line of outputs whereas 3-D switches work with planes of inputs and outputs.

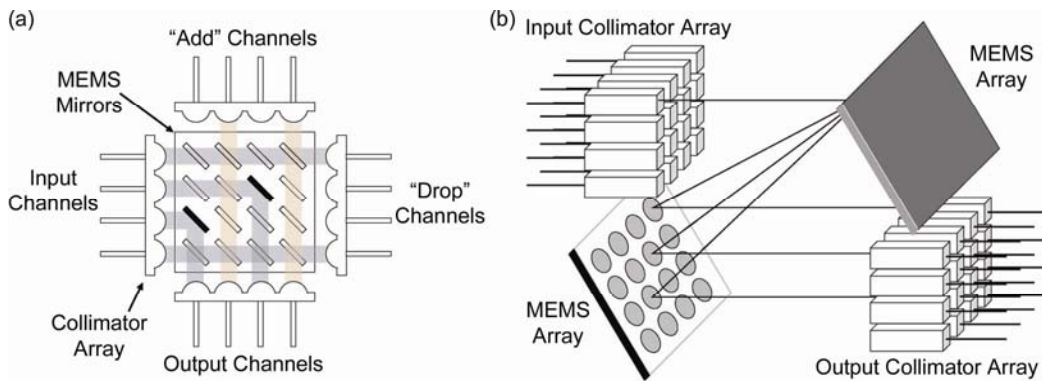


Fig. 2.1: Typical layout for (a) 2-D and (b) 3-D MEMS switches using micro-mirrors (adapted from [24])

In 2-D MEMS switches, collimated input beams propagate above and parallel to the MEMS chip surface. Light beams are controlled by inserting mirrors in and out of their path, usually at 45° with respect to the direction of propagation of light. The main advantage of 2-D MEMS switches is their digital operation, which simplifies control. In the common crossbar configuration, the number of switching elements scales as the square of the number of ports and thus the MEMS array size increases rapidly. Furthermore, since MEMS switches are free-space systems, the input beam size must also increase with the number of ports because the propagation distances inside the switches get larger. Thus, bigger input beams, which diverge less rapidly, are needed to limit insertion loss and crosstalk. This requires larger mirrors which are harder to fabricate. Mirror curvature can be a significant source of losses in MEMS switches. Another issue with crossbar switches is that the optical path length inside the switch varies depending on the connection being setup. Assuming a pitch p between adjacent micro-mirrors, the shortest path in the switch is $2p$ whereas the longest one is $(2N-1)p$ where N is the number of ports [18]. As a result, insertion losses are also connection dependent. This combination of factors limits 2-D MEMS crossbar switches to about 32 input and output ports [2, 19, 24]. Other layouts have been proposed to mitigate these issues, including Beneš, Spanke-Beneš [15], and shuffle Beneš [18] architectures, but none have been implemented.

Three-dimensional MEMS switches, also called beam steering switches, use analog tilting mirrors to connect two fibre arrays. In a typical switch (see Fig. 2.1(b)), a collimated input is reflected off a first mirror towards a second mirror associated with the desired output [2, 5, 12, 19, 21, 24, 25, 28]. The second mirror compensates the angular deviation induced by the first one in order to maximize coupling with the output fibre. This configuration requires only two mirrors per port and is highly scalable. A fabric with over a thousand ports has been demonstrated [12].

The main factors limiting the scalability of 3-D MEMS switches is beam diffraction and mirror tilt angle [2]. To work around these issues, systems including a Fourier lens [9], a concave mirror [13], or a roof top mirror [27] were designed. However, the most challenging aspect of 3-D MEMS switches is the precise control that is required on the mirror tilt angle. The angular repeatability must be within 0.1° [5]. This means that the hundreds of volts typically required to actuate tilt mirrors must be controlled with 10 mV precision [8].

2.3 Thermo-optic Switches

A simple way to modulate a material refractive index is to change its temperature. Variations in temperature affect a material refractive index by changing its electronic polarizability and its density [2]. For instance, changes in temperature modify the electronic polarizability of silica by shifting its resonant frequencies [33] (i.e. the same resonant frequencies that are associated with chromatic dispersion [34]). In the case of polymers, the decrease in density due to thermal expansion is the main cause of the refractive index change. In thermo-optic switches there is a trade-off between switching speeds and power efficiency since the speed of a switch is limited by its ability to generate and dissipate heat. A fast switch will dissipate heat rapidly and thus requires the continuous generation of large amounts of heat to remain in certain states. A switch requiring less power can be obtained with materials that have a low thermal conductivity since they

can capture heat more efficiently but that comes at the cost of slower switching speeds. Moreover, heating in thermo-optic switches is achieved with electrical micro-heaters and therefore switching times are limited by the speed of the electrical-thermal conversion and by the diffusion time.

Today, three material systems are commonly used to implement TO switches: polymers, silica waveguides and silicon-on-insulator [2]. Polymers have a large thermo-optic coefficient and a low thermal conductivity, which make them very efficient. Thus, they provide the largest index modulation of the three material platforms. Furthermore, they are cheap and can easily be deposited in thin-films on glass or silicon substrates by spin coating.

Silica waveguides, also referred to as planar lightwave circuits (PLC), are fabricated through flame hydrolysis deposition or chemical vapour deposition [35]. Their TO coefficient is approximately an order of magnitude less than polymers but their thermal conductivity can be ten times larger [2]. Therefore, switch configurations that require large index contrasts are implemented with polymers but those that can be operated with small index changes are built in PLC to achieve faster switching times thanks to the high thermal conductivity. Moreover, PLCs have lower propagation losses than polymer waveguides. Silica waveguides with losses lower than 0.01 dB/cm [35] have been demonstrated whereas the lowest propagation loss achieved in polymer waveguides is 0.1 dB/cm at 1550 nm [36].

In recent years, TO switches were demonstrated in silicon photonics [37-40]. The high index contrast achievable with silicon-on-insulator (SOI) structures allows for sharp waveguide bends, which lead to compact devices, and it is possible to integrate CMOS circuits with optical switches on the same chip [40]. Furthermore, silicon has a TO coefficient comparable to that of polymers [37] and a thermal conductivity a hundred times larger than silica [2]. This makes possible the implementation of TO switches with sub-microsecond switching times [40]. Silicon also has the unique capability of being used as an optical waveguide and

resistive electrode simultaneously by adjusting its doping. This ability was used to design a TO switch with a 600 ns switching time [38]. However, coupling and propagation losses are higher in silicon waveguides than in PLC or polymer waveguides.

Although a bulk thermo-optic beam deflector has been reported [41], the majority of TO switches are channel waveguide devices. The most common configurations include digital optical switches (DOS) [42-47], and Mach-Zehnder interferometers (MZI) [37-39, 48-54]. A DOS consists of a Y-junction with heaters on each of its branch, as shown in Fig. 2.2(a). The split angle is small (typically between 0.1° and 0.15°), which leads to switches that are millimetres long [42, 44, 45]. DOS are based on adiabatic mode evolution and switching is controlled by increasing the refractive index of the desired output waveguide [2] with respect to the other waveguide branch. The refractive index difference required in DOS is relatively large and thus they are usually implemented with polymers. Their main advantage is their digital response, which does not require precise control of the temperature. Also, they are wavelength and polarization independent [45]. The largest switch fabric built with DOS is 16x16 [43]. Scalability is limited by the DOS length.

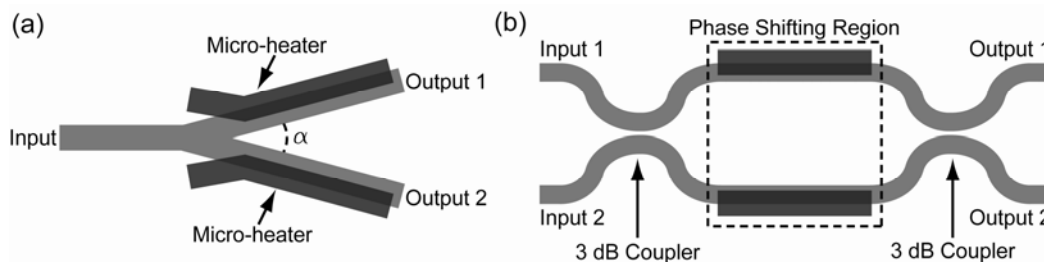


Fig. 2.2: Schematic of the most common thermo-optic switch configurations: (a) digital optical switch and (b) Mach-Zehnder Interferometer switch.

A Mach-Zehnder Interferometer consists of two 3 dB couplers, which can be directional couplers or multi-mode interferometers, and of a phase shifting region made of two decoupled waveguides (see Fig. 2.2(b)). Switching is achieved by controlling the phase difference between the two signals in the phase

shifting region by modulating the refractive index of the waveguides. Depending on the phase difference, constructive interference will occur in one of the two output waveguides [2]. Because they are based on interference, MZI requires smaller refractive index change than DOS and are the switch configuration most often used in silica waveguides [49, 50, 52-54]. The largest TO switch fabrics demonstrated so far is a 32x32 PLC switch with 2048 MZI [53]. MZI have also been implemented with polymers [48, 51], which results in devices with low power consumption. The drawback of the great sensitivity of MZI switches is that they require precise temperature control. Furthermore, their performance can be wavelength and polarization dependent [2].

2.4 Electro-optic Switches

A faster way to modulate a material refractive index than changing its temperature is to modify the position and/or density of charge carriers inside it. Depending on the nature of the material, this can be achieved in a number of ways. In noncentrosymmetric crystals [55] and specially designed polymers [56], applying an electric field can change the refractive index by redistributing the bonded charges, and it can also cause slight deformations of the ion lattice. This is called the electro-optic (EO) effect. It can either be linear or quadratic according to the index modulation dependence on the applied electric field. The quadratic effect is also referred to as the Kerr effect and it is usually ignored in the presence of the linear EO effect (also called Pockels effect) since the linear effect is much stronger. Furthermore, EO effects are anisotropic and thus the refractive index change they create varies with the direction of propagation of light with respect to the crystal lattice and with the light polarization. Generally, the modulation of the effective refractive index in an optical device is obtained from an electric field applied in a specific direction, and it couples with only one of the electro-optic coefficients of a material. Thus, the refractive index change can be estimated with this simple equation (see [55] for more details):

$$\Delta n = \frac{1}{2} n^3 r E \quad (2.1)$$

where r , n and E are the appropriate electro-optic coefficient, refractive index and electric field component, respectively. Linear EO coefficients are usually on the order of tens of pm/V in the most active materials, which lead to maximum refractive index modulation of about ± 0.001 . This is an order of magnitude less than thermo-optic effects. However, EO effects are extremely fast and they can achieve switching times of less than a nanosecond [4].

The most used EO material is lithium niobate (LiNbO_3) [57-73] because of its high EO coefficient ($r_{33} = 32.6$ pm/V [74]) and because low loss waveguides can be created in it by titanium diffusion or proton exchange [2]. Furthermore, it is possible to invert domains by electrical poling to maximize the refractive index contrast and simplify control [62, 69-71]. The drawback is that titanium and proton exchange waveguides have a low index contrast, and thus they require large bending radii which lead to large devices. Also, careful electrodes fabrication is required to avoid voltage drifts and pyroelectric effects [2].

EO switches have also been demonstrated in polymers [56, 75-78], which can have EO coefficients higher than LiNbO_3 [56]. However, most of them are proprietary, which limits their availability. Unlike TO polymers, stability is an issue with EO polymers [60, 79]. Another material than has interesting EO properties is lead-lanthanum-zirconate-titanate (PLZT) [80-82]. Its EO coefficient is high (612 pm/V [83]) and it can be polarization independent [80]. However, it presents serious fabrication challenges [84].

Linear electro-optic effects are present in compound semiconductors but their EO coefficients are smaller than LiNbO_3 [55]. Nevertheless, since the refractive index change induced with the linear electro-optic effect is proportional to the cube of the material refractive index, it is possible to obtain index modulation of the same order as LiNbO_3 thanks to the high refractive index of semiconductors. In III-V semiconductors, the EO effect is typically obtained with a P-I-N structure that is reverse biased [85] and several other electronic

phenomena can contribute to the refractive index modulation. The presence of an electric field changes the depletion region width, which results in a modification of the refractive index due to, in order of importance, electro-optic, band filling, Franz-Keldysh, and plasma effects when the incident wavelength is far from the absorption edge of the material [86]. The band-filling effect causes a change in the effective band-gap energy due to variations in carrier density [87]. As a result, the absorption edge shifts and this creates a refractive index change through the Kramers-Kronig relation. The absorption edge is also displaced by an increase in the tunnelling probability resulting from the tilt in the band edges caused by the application of an electric field [86]. This is called the Frank-Keldysh or electrorefractive effect. As in the case of the band filling effect, the refractive index modulation is a consequence of a change in absorption. The plasma effect, sometimes referred to as the free carrier effect, is another way to obtain a refractive index change by varying the optical absorption coefficient of a material. The change in absorption is obtained by varying the quantity of free carriers with which photons can interact. In reversed bias P-I-N structures, free carriers are removed from the depletion region and thus are less likely to absorb incoming photons [86].

A refractive index modulation can also be obtained by injecting carriers into a waveguide [79]. In this case, the refractive index change can be two orders of magnitude larger than with EO effects. The drawbacks are that speed is limited by carrier recombination times and that insertion losses increase when a current is present. Current modulation is often used in InP devices [88-93] because of the large index contrast it provides. Moreover, it is used in silicon photonics [94, 95] since silicon is a centrosymmetric crystal and thus it does not exhibit the linear electro-optic effect.

In devices with multiple quantum wells, the quantum-confined stark effect (QCSE) can create refractive index modulations. The presence of an electric field perpendicular to the quantum wells structure shifts the wells excitonic peaks,

which modifies the absorption coefficient and lead to a refractive index change [85]. Switches were built based on this phenomenon [96, 97] but it is used mostly in modulators [87].

Several electro-optic space switch configurations have been demonstrated in bulk or planar waveguides, including prism deflectors [62, 70, 71, 75, 80, 82, 98, 99], Bragg diffraction switches [65, 66, 69], and phase arrays [64, 91, 100-103]. Prism deflectors use the EO effect to create triangular regions of alternating high and low refractive index (see Fig. 2.3(a)). Refraction occurs at each interface, causing an angular deviation of the beam. The amount of deviation is controlled by varying the strength of the applied electric field, which sets the index contrast between the triangular regions. In LiNbO_3 , the triangular regions can be permanently poled (as long as the crystal remains below its Curie temperature) to increase the index contrast between them [70]. The shape of the electrode envelope can be optimized to maximize beam deflection for a given electric field. Horn-shaped [98] and parabolic [71] electrodes have been proposed. Prism deflectors have been demonstrated in ferroelectric crystals both in bulk [70, 71] and in planar waveguide configurations [104]. Planar waveguide devices were implemented in PLZT [80, 82], polymers [75], and InP [99]. In the InP devices, current injection was used instead of the EO effect.

Bragg diffraction switches use a thick phase grating generated with interdigitated electrodes or poled domains to deflect incoming beams, as shown in Fig. 2.3(b). Unlike prism deflectors they can only change the beam direction by a specific angle. Planar waveguide switch fabrics were reported in LiNbO_3 [65, 66] as well as a free-space implementation [69].

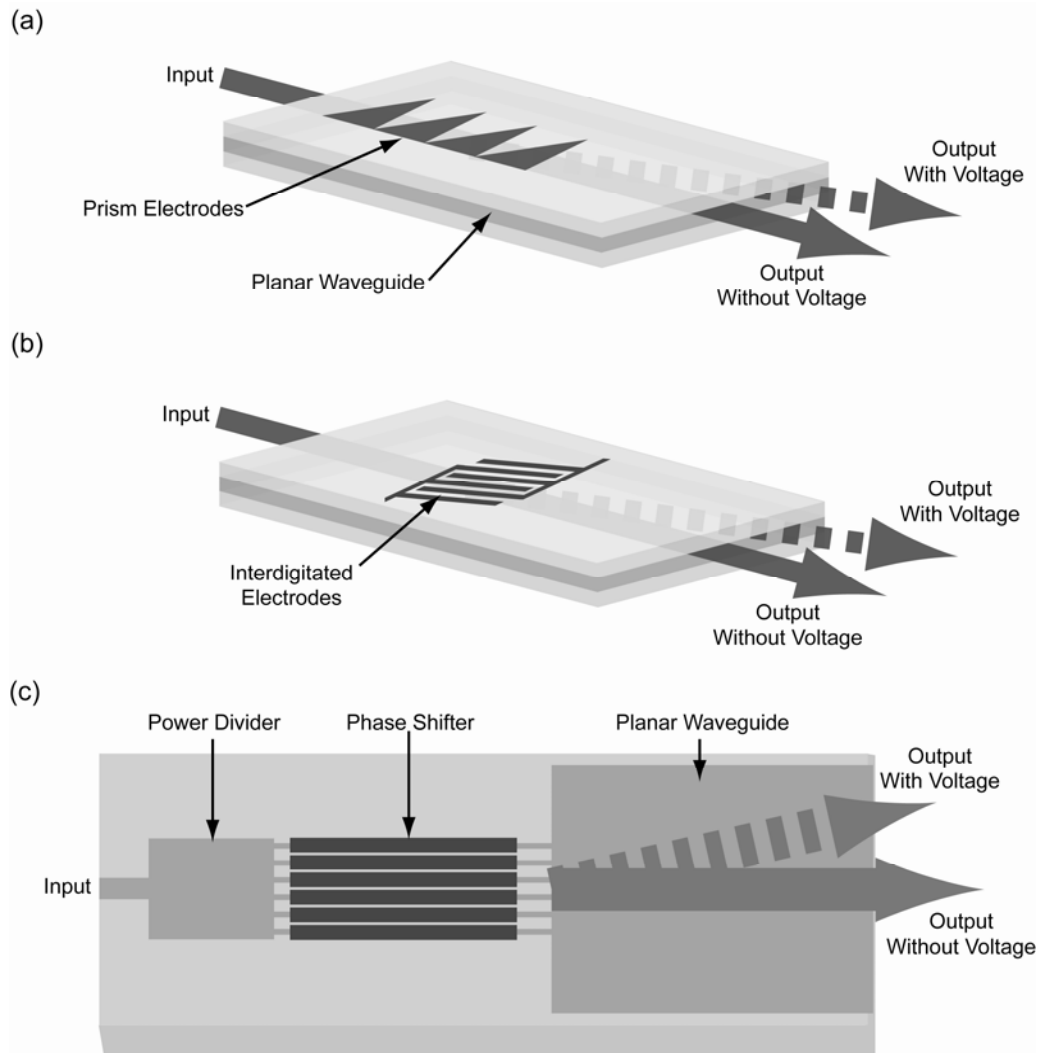


Fig. 2.3: Planar electro-optic switch configurations: (a) prism deflector, (b) Bragg diffraction switch, and (c) phase array.

In phase arrays, the input beam is steered by controlling its spatial phase profile. This is achieved with an array of electrodes that samples the beam at different points, as illustrated in Fig. 2.3(c). The beam propagation can be perpendicular or parallel to the electrodes [102]. The perpendicular configuration can only be implemented in free-space. In that case, the beam incident on the EO substrate experiences a varying phase change at different locations, thereby creating the equivalent of a phase diffraction grating that can be electrically tuned. Thus, it is possible to steer the light beam by changing the grating effective

period. In the more common parallel configuration, phase arrays are similar to Bragg switches in the sense that they work like thick phase gratings. However, the phase change across the beam is varied either by applying different voltages to the electrodes [101, 102] or by having electrodes of different lengths [64, 100, 103]. As a result, it is possible to steer the beam over a continuous range of angles, as with prism deflectors. Parallel phase arrays were implemented as free-space switches in ferroelectric crystals [101, 102]. Guided-wave configurations usually combine planar and channel waveguides [64, 91, 100, 105]. The input beam is coupled to an array of channel waveguides over which the electrodes are located. The channel waveguides end into a planar waveguide where the different beam components (each now having a different phase) recombine, leading to the desired beam deflection. Guided-wave phase arrays based on the linear EO effect were demonstrated in LiNbO₃ [64] and GaAs [103, 105]. A device using the QCSE to modulate the refractive index of GaAs quantum wells [100] and another one using current injection in InP [91] were reported.

The first EO switches using channel waveguides were directional couplers (DC) because of their simple structure and low loss characteristics [106]. DC consists of two single mode waveguides placed close to each other so that their mode overlaps, as shown in Fig. 2.4. This couples the waveguides, and as a consequence, power launched into one waveguide will transfer to the other after propagation over a certain distance called the coupling length. Light will transfer back into the first waveguide after propagating for another coupling length and this process will repeat itself as long as the separation between the waveguides is not changed. In a directional coupler switch, the device length is equal to one coupling length, such that light from one input appears at the opposite output. The switch is then in a cross state. To put it in a bar state, a refractive index contrast is created between the waveguides with the EO effects. This modifies the waveguides coupling and with the appropriate index contrast it is possible to avoid power transfer into the second waveguide.

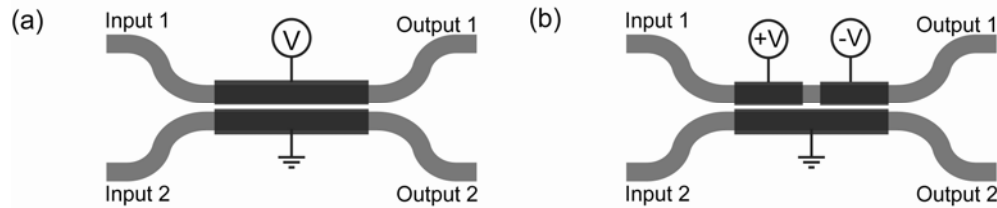


Fig. 2.4: Schematics of directional coupler switches with: (a) conventional electrodes and (b) $\Delta\beta$ electrodes

Although there are conceptually simple, DC switches are difficult to build because of the tight fabrication requirements needed to obtain devices of exactly one coupling length. Nevertheless, DC switch fabrics based on the linear EO effect have been demonstrated in LiNbO₃ [81, 84, 107], III-V semiconductors [108-110] and polymers [77, 78]. Current injection [93] and the QCSE [96] have also been used to control directional couplers. By splitting the electrodes in at least two sections (see Fig. 2.4(b)), it is possible to relax fabrication tolerances and reduce crosstalk [59]. This configuration is called a reversed $\Delta\beta$ directional coupler. The added degree of freedom obtained with the split electrodes allows electro-optic control of the coupling coefficient over a wide range. This approach was used in switch fabrics implemented in PLZT [81], GaAs [110], and LiNbO₃ [58].

Fabrication can also be simplified by using Mach-Zehnder interferometer switches since the coupling and phase shifting regions are separated, as explained in section 2.3. Furthermore, the small index modulation needed to operate MZI switches makes them suitable for EO implementation, which leads to devices much faster than those relying on the thermo-optic effect. Switching times as fast as 200 ps have been reported in EO MZI [79]. They have been demonstrated in LiNbO₃ [57, 68, 72] and III-V semiconductors [111-113]. Devices using current injection were fabricated in InP [92, 114] and silicon [95]. One implementation relying on the QCSE was also reported [97]. Electro-optic effects were also used to actuate digital optical switches. The devices implemented in polymer [76] or LiNbO₃ [61, 63, 67, 73] relied solely on the linear EO effect whereas those built in InP used current injection [88-90].

2.5 Semiconductor Optical Amplifier Switches

A semiconductor optical amplifier (SOA) can be viewed as a laser cavity with low or no optical feedback. They are usually made of InGaAsP epitaxial layers grown on InP substrates, and it is possible to integrate different passive and active components, such as lasers [115] or arrayed-waveguide gratings [116], on the same chip. Current injection in the SOA generates free carriers and creates a population inversion, which provides optical gain through stimulated emission [79]. When no current is present, light is absorbed. This ability to switch between gain and absorption enables SOAs to achieve extinction ratios larger than 40 dB. Polarization independent operation can be obtained with careful design of the gain region in bulk SOAs or appropriate strain in multiple quantum well structures [2]. When a small level of feedback is present, usually from reflections of the cavity facets, the SOA is a Fabry-Perot amplifier, which has multiple peaks in its gain spectrum. In the absence of feedback, the SOA is called a travelling-wave amplifier and it has a broad and smooth gain profile. Therefore, travelling-wave amplifiers are the preferred configuration for switching applications. The reflectivity at the end facets of an SOA can be reduced with anti-reflection coatings, tilting the SOA waveguide, or using buried facets.

The advantages of using SOAs as switching elements are their high extinction ratio, the possibility of compensating losses, and their broad bandwidth [117]. However, SOAs introduce noise, nonlinearities, and they can have significant power consumption. Furthermore, gain variations with changes in injected power can lead to signal distortion, reduction in extinction ratio, and generate crosstalk due to cross-gain modulation in WDM signals [79]. This can be mitigated with gain-clamping the SOAs [118].

SOA switch fabrics typically have a broadcast and select architecture in which multiple $1 \times N$ tree switches made of passive 3 dB couplers are interconnected [115, 118-123], as shown in Fig. 2.5(a). SOAs are located between the input and output tree switches where they act as on/off gates and

compensate for splitting losses. Input signals are split and sent to every output switches, where the SOA corresponding to the desired signal is turned on. This architecture enables the broadcast of signals to many outputs but this is achieved at the cost of high splitting losses. Moreover, the number of SOAs required in broadcast and select switches based on the tree architecture scales as the square of the number of ports. The largest monolithic switches reported are 4x4 fabrics [120, 122]. Silica waveguides have been integrated with SOA arrays to reduce propagation losses [121, 123]. An optical fibre shuffle network was used with 1x8 hybrid silica-InP switches with gain-clamped SOAs to build an 8x8 fabric [118]. The largest broadcast and select switch built to date is a 32x32 fabric but it was designed for radio over fibre applications [124] and it used an hybrid tree-Beneš architecture to reduce the number of SOAs. Monolithic 1x8 switches were designed for a 256x256 fabric but the fabric performance has not been reported yet [125]. The switch size can be significantly reduced if waveguide crossings are integrated in the SOAs. This has been demonstrated with quantum dot SOAs [119].

It is also possible to build crossbar switches with SOAs [126, 127]. As illustrated in Fig. 2.5(b), active couplers are used to interconnect passive waveguides laid out as a grid. When current is injected in the couplers, their refractive index matches that of the passive waveguides and light is transferred into them. When no current is present, there is not only an index mismatch between the waveguides but any light that couples in the SOAs is absorbed. Furthermore, the gain of the couplers can be adjusted to equalize the differential path losses typical of crossbar switches. Two implementations have been reported so far and both are 4x4 switches. In the first, passive and active waveguides were fabricated side-by-side using regrowth and a curved waveguide was used to connect active couplers [127]. In the second (shown in Fig. 2.5(b)), an active layer was grown over a passive guiding layer, creating vertical couplers

[126]. Total internal reflection mirrors were etched to connect the two SOAs forming active couplers.

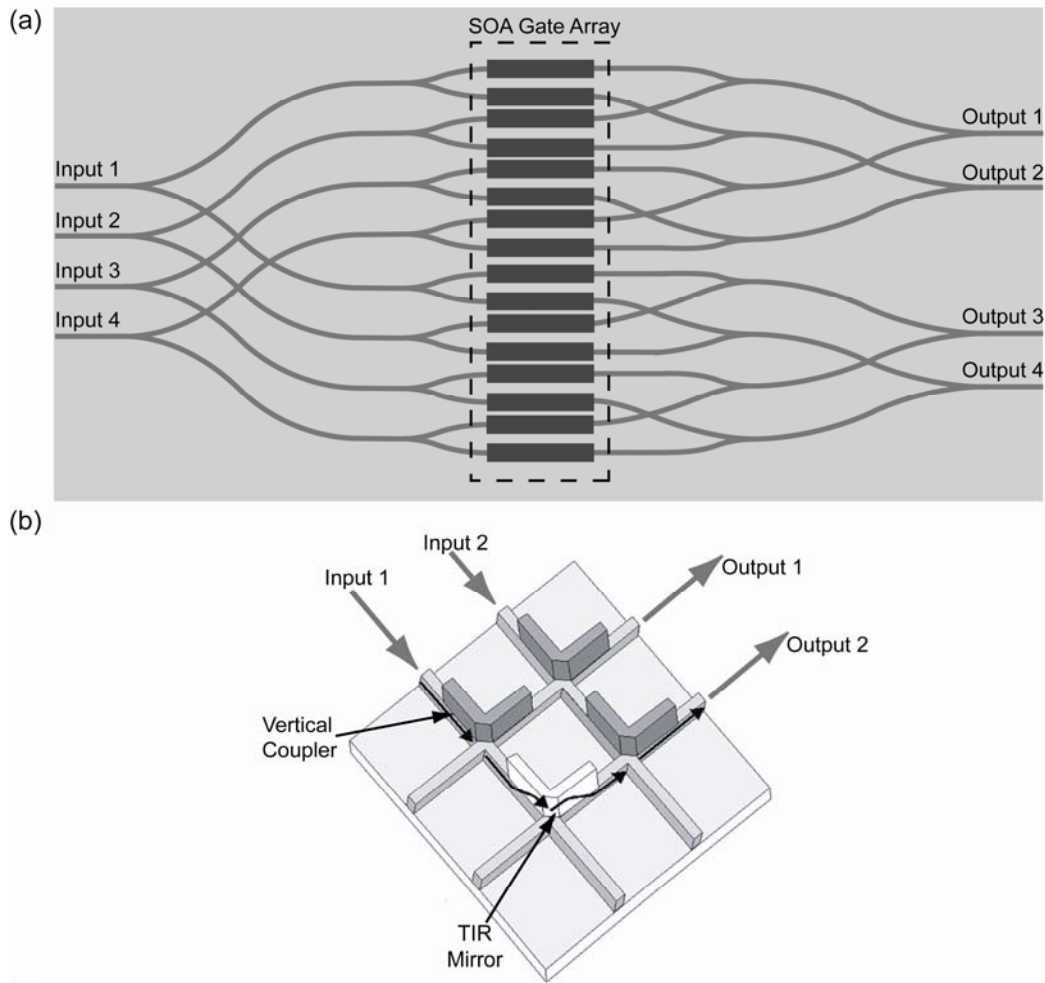


Fig. 2.5: Semiconductor optical amplifier 4x4 switch fabrics: (a) broadcast and select, and (b) active vertical-coupler (adapted from [126]).

2.6 Resonator Based Switches

This section presents optical space switches based on wavelength tuning of resonators. These devices often use the same actuation mechanisms as the switches described above but they have been grouped together in a separate section because they share the same optical working principles as the switch introduced in this thesis. Therefore, they are the switch configurations that are the

most similar to integrated Fabry-Perot optical space switches. The first category of resonator switches consist of previous implementations of space switches based on Fabry-Perot filters whereas the other one describes the latest integrated resonator switches made with micro-rings.

2.6.1 Fabry-Perot Switches

A typical Fabry-Perot (FP) filter consists of two partially reflecting mirrors separated by a small gap. Light incident on a FP filter will experience multiple reflections within that gap. If the optical length of the cavity formed by the two mirrors is an even multiple of the light half-wavelength, it will be transmitted through the cavity. If the cavity optical length corresponds to odd multiples of the light half-wavelength, then the light is completely reflected by the filter. The resonant wavelengths (λ_R) of an ideal FP filter are given by:

$$\lambda_R = \frac{2nL}{M} \quad (2.2)$$

where n is the cavity refractive index, L is its length, and M is a positive integer representing the resonance order. At a specific wavelength, switching between reflection and transmission can be achieved by changing the FP cavity optical length either by moving the mirrors, modulating the cavity refractive index, or varying the angle of incidence.

Because of their bistable response, Fabry-Perot filters with cavities made of nonlinear materials are often used as gate switches in all-optical logic [128, 129] and modulation experiments [130-132]. Optical space switches based on FP filters have been proposed, the simplest configuration being a 1x2 free-space device in which a collimated monochromatic input beam is projected at oblique incidence onto a tuneable FP cavity made through thin-film deposition on a transparent substrate (see Fig. 2.6) [133-135]. The FP cavity can be made of semiconductor, ferroelectric, or liquid crystal material and its refractive index can be modulated through electro-optic, thermo-optic, piezoelectric, or all-optical effects. The number of ports can be increased to form an 1xN switch by using

multiple non-coupled FP cavities [136]. Switches with light propagating at normal incidence on FP cavities have also been reported but they require circulators to separate the input and reflected beams [137]. Normal incidence devices with filters fabricated in channel waveguides were demonstrated [138, 139]. To avoid using circulators, FP switches working at normal incidence were used as gate switches in a broadcast and select architecture [140]. However, unlike SOAs they cannot compensate for splitting losses.

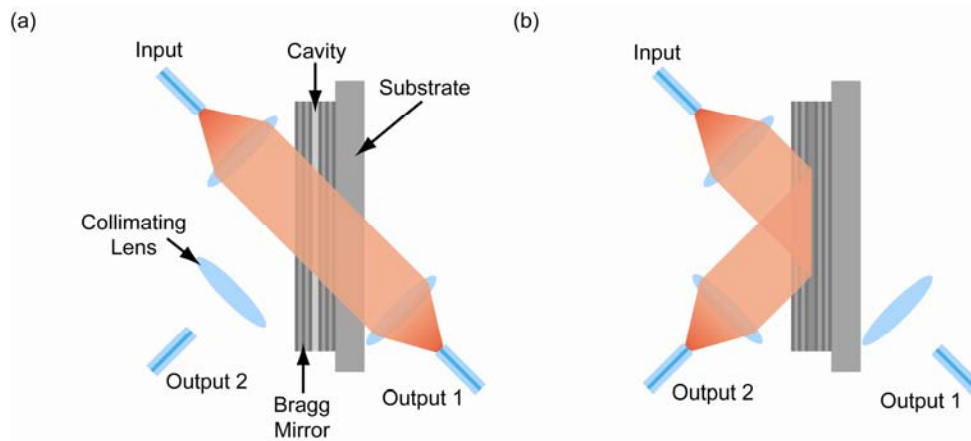


Fig. 2.6: Free-space Fabry-Perot switch schematics with cavity in (a) transmission and in (b) reflection.

2.6.2 Micro-ring Resonator Switches

Waveguide rings form travelling-wave resonators with wavelength responses similar to Fabry-Perot resonators. Fig. 2.7 shows typical layouts for 1x2 and 2x2 switches using micro-rings. The resonant wavelengths of a ring can be found in the same way as those of a FP filter except that the length L and the refractive index n in equation 2.2 must be replaced by the ring half-circumference and the group index of its guided mode, respectively [141]. Furthermore, matrix methods similar to those used with FP filters have been developed to optimize the wavelength response of micro-ring filters [142, 143]. Micro-rings are usually tens of micrometers in diameter and thus they must be implemented with high contrast waveguides to minimize bending loss. Silicon-on-insulator is the most used

platform to demonstrate micro-ring devices [142-148] but devices built in silicon nitride [149, 150] and III-V semiconductors [151] have also been reported. The drawback of high contrast waveguides for telecommunication applications is that their large modal mismatch with optical fibres makes coupling challenging. Moreover, the tight confinement of high index contrast waveguides means that the separations between micro-rings and channel waveguides or other micro-rings must be small (on the order of hundreds of nanometres) to achieve evanescent coupling. This leads to stringent fabrication requirements.

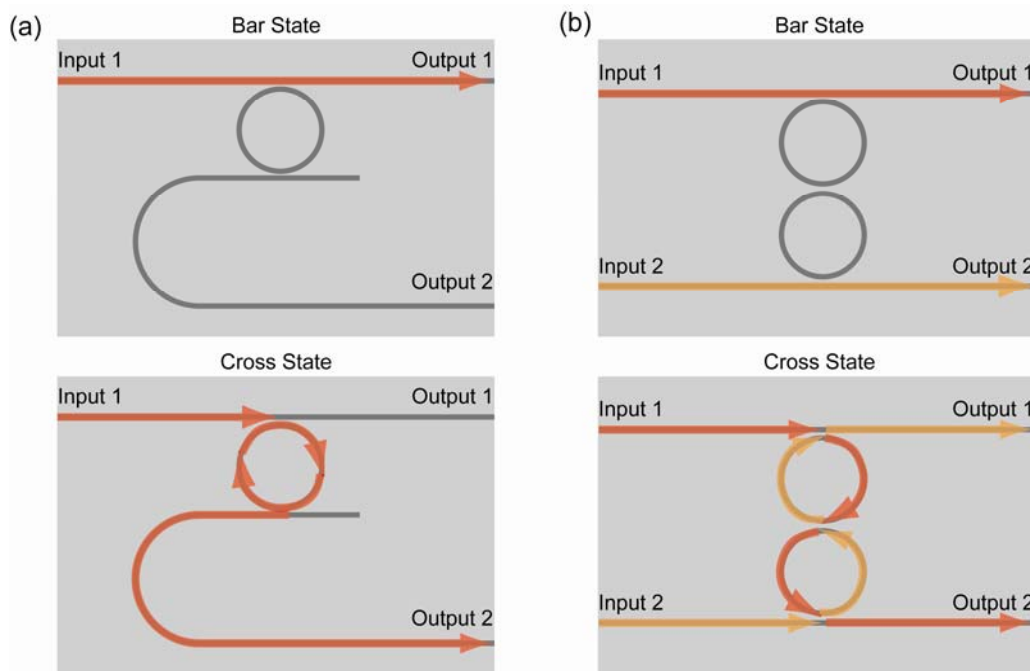


Fig. 2.7: Schematics of micro-ring switches: (a) single and (b) double ring layouts. Note that for the double ring switch, the inputs are shown in different colours only for clarity. Usually they have the same wavelength.

In micro-ring switches, the output port is selected by controlling the coupling between the input waveguide and the ring. If the input wavelength resonates with the ring, the signal is transferred to the waveguide on the opposite side of the ring. When this is not the case, the signal continues to propagate in the input waveguide. Tuning of the wavelength response of micro-rings can be achieved with plasma effects obtained either electrically [142, 147, 151] or

optically [142, 144, 148], thermo-optic effects [145, 146, 149], or by moving a membrane [150] or the coupling waveguides [152] with MEMS actuators. Tuning over 20 nm has been reported with the TO effect [145].

The coupling of multiple rings was realized to improve the passband shape of micro-ring filters [153], improve temperature tolerance [148], and reduce switching jitter and speed [147]. Filters with up to 11 coupled rings were implemented to achieve a flat passband with very sharp edges [153]. To extend the number of wavelength channels over which a micro-ring switch can operate, its free spectral range was reduced to about 0.85 nm by increasing the ring diameter to 200 μm , which created a comb response [144]. This switch was tested with 20 different 100-GHz channels in the C-band modulated at 10 Gb/s [142].

2.7 Conclusion

Table 2.1 below lists the insertion loss, crosstalk, polarization dependent loss (PDL) and switching time for typical implementations of the switches described above. MEMS switches are the most scalable and they have low insertion loss, crosstalk and PDL. Since MEMS mirrors have been used in commercial displays for several years, their reliability has been proven and packing technologies are mature. Unfortunately, MEMS have the longest switching times of all approaches reviewed here. Furthermore, as their number of port increases, MEMS switches become bulky since they are free-space devices.

Reliable integrated switches using the thermo-optic effect have been demonstrated with up to 32x32 ports. Their insertion losses and crosstalk levels are higher than MEMS devices but they are still acceptable for commercial applications. Their switching time is slightly faster but most devices require more than a millisecond, which is too slow for optical burst networks. Nevertheless, switches built in SOI waveguides have achieved sub-microsecond switching times. This could make TO switches an attractive solution for optical burst

network if coupling loss between optical fibres and high index waveguides are improved.

Although the switching time is not reported for many of the electro-optic devices listed in Table 2.1, the response time of most EO switches is limited by the driving electronics and thus they can be used in burst and packet switched networks. However, they have high insertion loss and crosstalk levels, and, with the exception of DOS, they exhibit strong polarization dependence. Therefore, EO switches can provide speed but much work is still required to improve their optical performance.

Because of their gating behaviour, semiconductor optical amplifier switches provide low crosstalk. With careful design, it is possible to obtain net gain after propagation through the switch and they have response times almost as fast as EO switches. The issue with SOA switches is scalability. In simple tree architectures, the number of SOAs required increase rapidly. In other architectures in which multiple SOAs share the same optical paths, the accumulation of amplified spontaneous emission noise can be problematic. Integration, which is required to reduce cost, is difficult because of the need for passive and active waveguides on the same layer. Vertical coupling can be used to avoid that but the SOAs must be carefully design to minimize facet reflectivity to preserve the bandwidth of the amplifiers.

Despite the numerous Fabry-Perot switch configurations proposed, none of them has been thoroughly characterised for operation in an optical telecommunication network. The free-space implementations suggested so far are too bulky to be scalable and the integrated ones require circulators to separate the input and reflected beams. Lastly, micro-rings are compact and they can be actuated rapidly. However, they need to be fabricated with high contrast waveguides, which have high coupling losses to fibres, and they have very tight fabrication requirements.

Therefore, even the most mature and promising optical space switching technologies available at this time are not able to meet the requirements for optical burst and packet switching networks. In general, the technologies with the appropriate optical performances are not fast enough whereas the fast ones have excessive loss, crosstalk or they are polarization dependent.

Table 2.1: Performance comparison of different type of optical space switches

Switch Type	Port Count	Insertion Loss (dB)	Crosstalk (dB)	PDL (dB)	Switching Time
MEMS					
2-D	8x8 [10]	5.0	< -40	N/A	< 6 ms
	16x16 [29]	3.1	< -50	0.4	7 ms
3-D	64x64 [13]	1.9	< -60	N/A	<10 ms
	1100x1100 [12]	2.1	N/A	<0.1	~10 ms
Thermo-Optic					
DOS	8x8 [47]	10.7	-30	0.5	1.0 ms
	16x16 [43]	6.0	< -30	Low	N/A
MZI	8x8 [54]	5.1	< -43	0.3	2.0 ms
	32x32 [53]	6.6	-55 ¹	< 0.5	0.7 ms
Electro-Optic					
Prism	8x8 [82]	15.0	N/A	Small	< 1 μ s
Phase Array	64x64 [105]	14.5	< -25	Pol. Dep.	20 ns ²
DC	8x8 [108]	8.7	< -21	Pol. Dep.	N/A
	16x16 [107]	~10.5	-20	Pol. Dep.	N/A
MZI	4x4 [113]	5.0	< -15	\pm 0.5	200 ps
	8x8 [72]	<11.4	< -20	< 1.0	N/A
DOS	4x4 [79]	15.0	< -13	Pol. Indep.	N/A
	8x8 [73]	8.0	< -16	Pol. Indep.	N/A
SOA					
Active coupler	4x4 [126]	0-5 dB gain	< -65	Pol. Dep.	1.5 ns
Broadcast	8x8 [118]	< 14.0	< -32	< 0.9	N/A
Micro-ring	1x2 [144]	10.0	< -15	Pol. Dep.	1 ns

¹ Extinction ratio² Includes drive electronics

References

- [1] A. K. Dutta, N. K. Dutta, and M. Fujiwara, *WDM technologies: passive optical components* vol. II. Boston: Elsevier Academic Press, 2003.
- [2] T. S. A. El-Bawab, *Optical switching*. New York: Springer, 2006.
- [3] X. H. Ma and G. S. Kuo, "Optical switching technology comparison: optical MEMS vs. other technologies," *IEEE Commun. Mag.*, vol. 41, no. 11, pp. S16-S23, Nov. 2003.
- [4] G. I. Papadimitriou, C. Papazoglou, and A. S. Pomportsis, "Optical switching: Switch fabrics, techniques, and architectures," *J. Lightwave Technol.*, vol. 21, no. 2, pp. 384-405, Feb. 2003.
- [5] M. J. Potasek, "All-optical switching for high bandwidth optical networks," *Optical Networks Magazine*, vol. 3, no.6, pp. 30-43, Nov. 2002
- [6] S. S. Lee, L. Y. Lin, and M. C. Wu, "Surface-micromachined free-space fiber-optic switches," *Electron. Lett.*, vol. 31, no. 17, pp. 1481-1482, Aug. 1995.
- [7] V. Barua, H. Nayim, and B. Mahmud Abdul Matin, "A 2x2 MEMS optical switch based on piezoelectric actuation," in *International Conference on Electrical and Computer Engineering*, Dhaka, Bangladesh, 2006, pp. 52-55.
- [8] A. S. Morris, "In search of transparent networks," *IEEE Spectrum*, vol. 38, no. 10, pp. 47-51, Oct 2001.
- [9] V. A. Aksyuk, S. Arney, N. R. Basavanhally, D. J. Bishop, C. A. Bolle, C. C. Chang, R. Frahm, A. Gasparyan, J. V. Gates, R. George, C. R. Giles, J. Kim, P. R. Kolodner, T. M. Lee, D. T. Neilson, C. Nijander, C. J. Nuzman, M. Paczkowski, A. R. Papazian, F. Pardo, D. A. Ramsey, R. Ryf, R. E. Scotti, H. Shea, and M. E. Simon, "238x238 micromechanical optical cross connect," *Photon. Tech. Lett.*, vol. 15, no. 4, pp. 587-589, Apr. 2003.
- [10] C. P. Jia, J. R. Zhou, W. Dong, and W. Y. Chen, "Design and fabrication of silicon-based 8x8 MEMS optical switch array," *Microelectron. J.*, vol. 40, no. 1, pp. 83-86, Jan. 2009.
- [11] S. A. Khan and N. A. Riza, "Demonstration of the MEMS digital micromirror device-based broadband reconfigurable optical add-drop filter for dense wavelength-division-multiplexing systems," *J Lightwave Techno.*, vol. 25, no. 2, pp. 520-526, Feb. 2007.
- [12] J. Kim, C. J. Nuzman, B. Kumar, D. F. Lieuwen, J. S. Kraus, A. Weiss, C. P. Lichtenwalner, A. R. Papazian, R. E. Frahm, N. R. Basavanhally, D. A. Ramsey, V. A. Aksyuk, F. Pardo, M. E. Simon, V. Lifton, H. B. Chan, M. Haeis, A. Gasparyan, H. R. Shea, S. Arney, C. A. Bolle, P. R. Kolodner, R. Ryf, D. T. Neilson, and J. V. Gates, "1100 x 1100 port MEMS-based optical crossconnect with 4-dB maximum loss," *IEEE Photon. Tech. Lett.*, vol. 15, no. 11, pp. 1537-1539, Nov. 2003.
- [13] M. Kozhevnikov, N. R. Basavanhally, J. D. Weld, Y. L. Low, P. Kolodner, C. A. Bolle, R. Ryf, A. R. Papazian, A. Olkhovets, E. Pardo, J. Kim, D. T. Neilson, V. A. Aksyuk, and J. V. Gates, "Compact 64x64 micromechanical optical cross connect," *IEEE Photon. Tech. Lett.*, vol. 15, no. 7, pp. 993-995, Jul. 2003.
- [14] J. N. Kuo, G. B. Lee, and W. F. Pan, "A high-speed low-voltage double-switch optical crossconnect using stress-induced bending, micromirrors," *IEEE Photon. Tech. Lett.*, vol. 16, no.9, pp. 2042-2044, Sep. 2004.
- [15] C. Y. Li, G. M. Li, V. O. K. Li, P. K. A. Wai, H. Xie, and X. C. Yuan, "Using 2x2 switching modules to build large 2-D MEMS optical switches," in *Global Telecommunications Conference*, 2003, San Francisco, CA, USA, vol.5, pp. 2798-2802.
- [16] L. Y. Lin, E. L. Goldstein, and R. W. Tkach, "Free-space micromachined optical switches for optical networking," *IEEE J Sel. Top. Quant.*, vol. 5, no. 1, pp. 4-9, Jan-Feb 1999.

- [17] L. Y. Lin, S. S. Lee, K. S. J. Pister, and M. C. Wu, "Micro-machined 3-dimensional microoptics for integrated free-space optical-system," *IEEE Photon. Tech. Lett.*, vol. 6, no. 12, pp. 1445-1447, Dec. 1994.
- [18] X. H. Ma and G. S. Kuo, "A novel integrated multistage optical MEMS-mirror switch architecture design with shuffle Benes inter-stage connecting principle," *Opt. Commun.*, vol. 242, no. 1-3, pp. 179-189, Nov. 2004.
- [19] T. S. A. El-Bawab, A. Agrawal, F. Poppe, L. B. Sofman, D. Papadimitriou, and B. Rousseau, "The Evolution to Optical-switching-based Core Networks," in *Optical Networks Magazine*. vol. 4, no. 2, pp. 7-18, Mar. 2003
- [20] K. E. Petersen, "Silicon Torsional Scanning Mirror," *IBM J Res Dev*, vol. 24, no. 5, pp. 631-637, 1980.
- [21] R. R. A. Syms, "Scaling laws for MEMS mirror-rotation optical cross connect switches," *J Lightwave Technol.*, vol. 20, no. 7, pp. 1084-1094, Jul. 2002.
- [22] H. Toshiyoshi and H. Fujita, "Electrostatic micro torsion mirrors for an optical switch matrix," *J Microelectromech S*, vol. 5, no. 4, pp. 231-237, Dec. 1996.
- [23] H. Toshiyoshi, D. Miyauchi, and H. Fujita, "Electromagnetic torsion mirrors for self-aligned fiber-optic crossconnectors by silicon micromachining," *IEEE J Sel. Top. Quant.*, vol. 5, no. 1, pp. 10-17, Jan-Feb 1999.
- [24] M. C. Wu, A. Solgaard, and J. E. Ford, "Optical MEMS for lightwave communication," *J Lightwave Technol.*, vol. 24, no. 12, pp. 4433-4454, Dec. 2006.
- [25] T. Yamamoto, J. Yamaguchi, N. Takeuchi, A. Shimizu, E. Higurashi, R. Sawada, and Y. Uenishi, "A three-dimensional MEMS optical switching module having 100 input and 100 output ports," *IEEE Photon. Tech. Lett.*, vol. 15, no. 10, pp. 1360-1362, Oct. 2003.
- [26] Y. J. Yang, B. T. Liao, and W. C. Kuo, "A novel 2x2 MEMS optical switch using the split cross-bar design," *J Micromech. Microeng.*, vol. 17, no. 5, pp. 875-882, May 2007.
- [27] M. Yano, F. Yamagishi, and T. Tsuda, "Optical MEMS for photonic switching-compact and stable optical crossconnect switches for simple, fast, and flexible wavelength applications in recent photonic networks," *IEEE J Sel. Top. Quant.*, vol. 11, no. 2, pp. 383-394, Mar-Apr 2005.
- [28] X. Z. Zheng, V. Kaman, S. F. Yuan, Y. J. Xu, O. Jerphagnon, A. Keating, R. C. Anderson, H. N. Poulsen, B. Liu, J. R. Sechrist, C. Pularla, R. Helkey, D. J. Blumenthal, and J. E. Bowers, "Three-dimensional MEMS photonic cross-connect switch design and performance," *IEEE J Sel. Top. Quant.*, vol. 9, no. 2, pp. 571-578, Mar-Apr 2003.
- [29] P. De Dobbelaere, K. Falta, L. Fan, S. Gloeckner, and S. Patra, "Digital MEMS for optical switching," *IEEE Commun. Mag.*, vol. 40, no. 3, pp. 88-95, Mar 2002.
- [30] M. Simard, Z. Khalid, and A. G. Kirk, "Digital optical space switch based on micromotor grating scanners," *IEEE Photon. Tech. Lett.*, vol. 18, no. 1-4, pp. 313-315, Jan-Feb 2006.
- [31] W. Li, J. Q. Liang, Z. Z. Liang, X. Q. Li, W. B. Wang, Y. C. Zhong, and D. G. Sun, "Design and fabrication of a micro-optic switch," *Opt. Express*, vol. 16, no. 9, pp. 6324-6330, Apr. 2008.
- [32] Y. J. Yang, W. C. Kuo, K. C. Fan, and W. L. Lin, "A 1x2 optical fiber switch using a dual-thickness SOI process," *J Micromech Microeng.*, vol. 17, no. 5, pp. 1034-1041, May 2007.
- [33] C. Z. Tan, "Review and analysis of refractive index temperature dependence in amorphous SiO₂," *J Non-cryst Solids*, vol. 238, no. 1-2, pp. 30-36, Sept. 1998.
- [34] M. Born and E. Wolf, *Principles of optics: electromagnetic theory of propagation, interference and diffraction of light*, 7th expanded ed. New York: Cambridge University Press, 1999.
- [35] K. Okamoto, *Fundamentals of optical waveguides*, 2nd ed. Burlington, MA: Elsevier Academic Press, 2006.
- [36] L. Eldada and L. W. Shacklette, "Advances in polymer integrated optics," *IEEE J Sel. Top. Quant.*, vol. 6, no. 1, pp. 54-68, Jan-Feb 2000.

- [37] A. Densmore, D. X. Xu, S. Janz, P. Waldron, T. Mischki, G. Lopinski, A. Delage, J. Lapointe, P. Cheben, B. Lamontagne, and J. H. Schmid, "Spiral-path high-sensitivity silicon photonic wire molecular sensor with temperature-independent response," *Opt. Lett.*, vol. 33, no. 6, pp. 596-598, Mar. 2008.
- [38] M. W. Geis, S. J. Spector, R. C. Williamson, and T. M. Lyszczarz, "Submicrosecond submilliwatt silicon-on-insulator thermo-optic switch," *IEEE Photon. Tech. Lett.*, vol. 16, no. 11, pp. 2514-2516, Nov. 2004.
- [39] Z. Y. Li, J. H. Yu, S. W. Chen, and J. W. Liu, "Novel folding 8x8 silicon-based optical matrix switch with tapered waveguides and self-aligned corner mirrors," *J Lightwave Technol.*, vol. 24, no. 12, pp. 5008-5012, Dec 2006.
- [40] J. F. Song, Q. Fang, S. H. Tao, T. Y. Liow, M. B. Yu, G. Q. Lo, and D. L. Kwong, "Fast and low power Michelson interferometer thermo-optical switch on SOI," *Opt. Express*, vol. 16, no. 20, pp. 15304-15311, Sep. 2008.
- [41] M. Haruna and J. Koyama, "Thermo-Optic Deflection and Switching in Glass," *Appl. Optics*, vol. 21, no. 19, pp. 3461-3465, Oct. 1982.
- [42] Y. T. Han, J. U. Shin, S. H. Park, S. P. Han, C. H. Lee, Y. O. Noh, H. J. Lee, and Y. Baek, "Crosstalk-Enhanced DOS Integrated with Modified Radiation-Type Attenuators," *Etri J*, vol. 30, no. 5, pp. 744-746, Oct 2008.
- [43] F. L. W. Rabbering, J. F. P. van Nunen, and L. Eldada, "Polymeric 16x16 digital optical switch matrix," in *European Conference on Optical Communication*, Amsterdam, Netherlands, 2001, vol.6 pp. 78-79
- [44] C. Ma and E. Van Keuren, "New design of a beam-steering thermo-optic multimode polymer waveguide switch," *Appl Phys B-Lasers O*, vol. 85, no. 4, pp. 619-623, Dec. 2006.
- [45] Y. O. Noh, H. J. Lee, Y. H. Won, and M. C. Oh, "Polymer waveguide thermo-optic switches with -70 dB optical crosstalk," *Opt. Commun.*, vol. 258, no. 1, pp. 18-22, Feb. 2006.
- [46] D. M. Yeo and S. Y. Shin, "Polymer-silica hybrid 1x2 thermo-optic switch with low crosstalk," *Opt. Commun.*, vol. 267, no. 2, pp. 388-393, Nov. 2006.
- [47] A. Borreman, T. Hoekstra, M. Diemeer, H. Hoekstra, and P. Lambeck, "Polymeric 8x8 digital optical switch matrix," in *European Conference on Optical Communication*, Oslo, Norway, 1996, vol.5 pp. 59-62
- [48] A. M. Al-Hetar, A. S. M. Supa'at, A. B. Mohammad, and I. Yuhanti, "Crosstalk improvement of a thermo-optic polymer waveguide MZI-MMI switch," *Opt. Commun.*, vol. 281, no. 23, pp. 5764-5767, Dec 2008.
- [49] M. P. Earnshaw, M. A. Cappuzzo, E. Chen, L. Gomez, and A. Wong-Foy, "Ultra-low power thermo-optic silica-on-silicon waveguide membrane switch," *Electron. Lett.*, vol. 43, no. 7, pp. 393-394, 2007.
- [50] Q. Lai, W. Hunziker, and H. Melchior, "Low-power compact 2x2 thermo-optic silica-on-silicon waveguide switch with fast response," *IEEE Photon. Tech. Lett.*, vol. 10, no. 5, pp. 681-683, May 1998.
- [51] M. C. Oh, H. J. Lee, M. H. Lee, J. H. Ahn, and S. G. Han, "Asymmetric X-junction thermo-optic switches based on fluorinated polymer waveguides," *IEEE Photon. Tech. Lett.*, vol. 10, no. 6, pp. 813-815, Jun. 1998.
- [52] T. Shibata, M. Okuno, T. Goh, T. Watanabe, M. Yasu, M. Itoh, M. Ishii, Y. Hibino, A. Sugita, and A. Himeno, "Silica-based waveguide-type 16x16 optical switch module incorporating driving circuits," *IEEE Photon. Tech. Lett.*, vol. 15, no. 9, pp. 1300-1302, Sep. 2003.
- [53] S. Sohma, T. Watanabe, N. Ooba, M. Itoh, T. Shibata, and H. Takahashi, "Silica-based PLC Type 32x32 Optical Matrix Switch," in *European Conference on Optical Communications*, Cannes, France, 2006, pp. 1-2.

- [54] T. Goh, A. Himeno, M. Okuno, H. Takahashi, and K. Hattori, "High-extinction ratio and low-loss silica-based 8x8 strictly nonblocking thermo-optic matrix switch," *J Lightwave Technol.*, vol. 17, no. 7, pp. 1192-1199, Jul. 1999.
- [55] A. Yariv and P. Yeh, *Optical waves in crystals: propagation and control of laser radiation*, Hoboken, N.J.: Wiley, 2003.
- [56] L. Eldada, "Polymer integrated optics: promise versus practicality," in *the Society of Photo-Optical Instrumentation Engineers (SPIE) Conference*, 2002, pp. 11-22.
- [57] A. Chiba, T. Kawanishi, T. Sakamoto, K. Higuma, and M. Izutsu, "Low-crosstalk LiNbO₃ optical switch with embedded sub Mach-Zehnder structures," in *Annual Meeting of the Lasers and Electro-Optics Society*, Montreal, Canada, 2006, pp. 757-758.
- [58] P. Granstrand, B. Stoltz, L. Thylen, K. Bergvall, W. Doldissen, H. Heinrich, and D. Hoffmann, "Strictly nonblocking 8x8 integrated optical switch matrix," *Electron. Lett.*, vol. 22, no. 15, pp. 816-818, Jul. 1986.
- [59] R. C. Alferness, "Waveguide Electrooptic Switch Arrays," *IEEE J Sel. Areas Comm.*, vol. 6, no. 7, pp. 1117-1130, Aug. 1988.
- [60] H. Nakajima, "Development on guided-wave switch arrays," *IEICE T Electron.*, vol. E82C, no. 2, pp. 297-304, Feb. 1999.
- [61] R. Krahenbuhl, M. M. Howerton, J. Dubinger, and A. S. Greenblatt, "Performance and modeling of advanced Ti:LiNbO₃ digital optical switches," *J Lightwave Technol.*, vol. 20, no. 1, pp. 92-99, Jan. 2002.
- [62] J. F. Lotspeic, "Electrooptic Light-Beam Deflection," *IEEE Spectrum*, vol. 5, no. 2, pp. 45-52, Feb. 1968.
- [63] H. Okayama, T. Arai, and T. Tsuruoka, "Arrayed 1 x N switch for wavelength routing," *IEICE T Electron.*, vol. E83C, no. 6, pp. 920-926, Jun 2000.
- [64] H. Okayama and M. Kawahara, "Experiment on deflector-selector optical switch matrix," *Electron. Lett.*, vol. 28, no. 7, pp. 638-639, Mar 1992.
- [65] C. H. Peng, R. J. Falster, and W. S. C. Chang, "NxM planar optical-waveguide switch for computer communications," *J Opt Soc Am*, vol. 70, no. 12, pp. 1577-1578, Dec. 1980.
- [66] E. M. Philipp-rutz, R. Linares, and M. Fakuda, "Electrooptic Bragg-diffraction switches in low cross-talk integrated-optics switching matrix," *Appl. Optics*, vol. 21, no. 12, pp. 2189-2194, Jun. 1982.
- [67] Y. Silberberg, P. Perlmutter, and J. E. Baran, "Digital Optical Switch," *Appl. Phys. Lett.*, vol. 51, no. 16, pp. 1230-1232, Oct. 1987.
- [68] K. Suzuki, T. Yamada, M. Ishii, T. Shibata, and S. Mino, "High-speed optical 1x4 switch based on generalized Mach-Zehnder interferometer with hybrid configuration of silica-based PLC and lithium niobate phase-shifter array," *IEEE Photon. Tech. Lett.*, vol. 19, no. 9-12, pp. 674-676, May-Jun. 2007.
- [69] M. Yamada, "Electrically induced Bragg-diffraction grating composed of periodically inverted domains in lithium niobate crystals and its application devices," *Rev Sci. Instrum.*, vol. 71, no. 11, pp. 4010-4016, Nov. 2000.
- [70] Y. Zuo, B. Bahamin, E. J. Tremblay, C. Pulikkaseril, E. Shoukry, M. Mony, P. Langlois, V. Aimez, and D. V. Plant, "1x2 and 1x4 electrooptic switches," *IEEE Photon. Tech. Lett.*, vol. 17, no. 10, pp. 2080-2082, Oct. 2005.
- [71] Y. Y. Zuo, M. Mony, B. Bahamin, E. Grondin, V. Aimez, and D. V. Plant, "Bulk electro-optic deflector-based switches," *Appl. Optics*, vol. 46, no. 16, pp. 3323-3331, Jun. 2007.
- [72] Y. Nakabayashi, M. Kitamura, and T. Sawano, "DC-drift free polarization independent Ti:LiNbO₃ 8x8 optical matrix switch," in *European Conference on Optical Communication*, Oslo, Norway, 1996, vol.4 pp. 157-160.
- [73] H. Okayama and M. Kawahara, "Ti:LiNbO₃ digital optical switch matrices," *Electronics Letters*, vol. 29, pp. 765-766, 1993.
- [74] M. J. Weber, *Handbook of optical materials*. Boca Raton: CRC Press, 2003.
- [75] L. Sun, J. H. Kim, C. H. Jang, D. C. An, X. J. Lu, Q. J. Zhou, J. M. Taboada, R. T. Chen, J. J. Maki, S. N. Tang, H. Zhang, W. H. Steier, C. Zhang, and L. R. Dalton, "Polymeric

- waveguide prism-based electro-optic beam deflector," *Opt. Eng.*, vol. 40, no. 7, pp. 1217-1222, Jul. 2001.
- [76] W. Yuan, S. Kim, H. R. Fetterman, W. H. Steier, D. L. Jin, and R. Dinu, "Hybrid integrated cascaded 2-bit electrooptic digital optical switches (DOSs)," *IEEE Photon. Tech. Lett.*, vol. 19, no. 5-8, pp. 519-521, Mar.-Apr. 2007.
- [77] C. T. Zheng, C. S. Ma, X. Yan, X. Y. Wang, and D. M. Zhang, "Analysis of response characteristics for polymer directional coupler electro-optic switches," *Opt. Commun.*, vol. 281, no. 24, pp. 5998-6005, Dec. 2008.
- [78] C. T. Zheng, C. S. Ma, X. Yan, X. Y. Wang, and D. M. Zhang, "Simulation and optimization of a polymer directional coupler electro-optic switch with push-pull electrodes," *Opt. Commun.*, vol. 281, no. 14, pp. 3695-3702, Jul. 2008.
- [79] M. Renaud, M. Bachmann, and M. Erman, "Semiconductor optical space switches," *IEEE J Sel. Top. Quant.*, vol. 2, no. 2, pp. 277-288, Jun. 1996.
- [80] A. L. Glebov, M. G. Lee, L. Huang, S. Aoki, K. Yokouchi, M. Ishii, and M. Kato, "Electrooptic planar deflector switches with thin-film PLZT active elements," *IEEE J Sel. Top. Quant.*, vol. 11, no. 2, pp. 422-430, Mar.-Apr. 2005.
- [81] K. Nashimoto, N. Tanaka, M. LaBuda, D. Ritums, J. Dawley, M. Raj, D. Kudzuma, and T. Vo, "High-speed PLZT optical switches for burst and packet switching," in *2nd International Conference on Broadband Networks*, Boston, MA, USA, 2005, Vol. 2 pp. 1118-1123.
- [82] A. Sugama, T. Akahoshi, K. Sato, S. Aoki, Y. Kai, Y. Takita, M. Kato, and H. Onaka, "Integrated 8x8 Electro-optic High-Speed Switch for Optical Burst Transport Networks," presented at *Optical Fiber Communication Conference*, Anaheim, CA, USA, 2007.
- [83] G. H. Haertlin and C. E. Land, "Hot-pressed (Pb,La)(Zr,Ti)O₃ ferroelectric ceramics for electrooptic applications," *J Am Ceram Soc*, vol. 54, no. 1, pp. 1-11, Jan. 1971.
- [84] K. Nashimoto, *PLZT Thin Film Optical Waveguides and Devices*, Nozomi Photonics Co., 2003.
- [85] N. Dagli, *High-speed photonic devices*. New York: Taylor & Francis, 2007.
- [86] J. G. Mendoza-Alvarez, L. A. Coldren, A. Alping, R. H. Yan, T. Hausken, K. Lee, and K. Pedrotti, "Analysis of depletion edge translation lightwave modulators," *J Lightwave Technol.*, vol. 6, no. 6, pp. 793-808, Jun. 1988.
- [87] M. Fukuda, *Optical semiconductor devices*. New York: Wiley, 1999.
- [88] M. Lesecq, M. Beaugeois, S. Maricot, and J. P. Vilcot, "Crosstalk measurement of DOS-like switch using InP narrow deep-etched waveguides," *Opt. Express*, vol. 16, no. 8, pp. 5181-5185, Apr. 2008.
- [89] W. H. Nelson, A. N. M. M. Choudhury, M. Abdalla, R. Bryant, E. Meland, and W. Niland, "Wavelength-Independent and Polarization-Independent Large-angle InP/InGaAsP digital optical switches with extinction ratios exceeding 20-dB," *IEEE Photon. Tech. Lett.*, vol. 6, no. 11, pp. 1332-1334, Nov. 1994.
- [90] S. Ng, S. Janz, W. R. McKinnon, P. Barrios, A. Delage, and B. A. Syrett, "Performance optimization of a reconfigurable waveguide digital optical switch on InGaAsP/InP: design, material, and carrier dynamics," *IEEE J Quant. Elect.*, vol. 43, no.12, pp. 1147-1158, Dec. 2007.
- [91] T. Tanemura, M. Takenaka, A. Abdullah, K. Takeda, T. Shioda, M. Sugiyama, and Y. Nakano, "Design and Fabrication of Integrated 1x5 Optical Phased Array Switch on InP," in *The 20th Annual Meeting of the IEEE Lasers and Electro-Optics Society*, Lake Buena Vista, FL, USA, 2007, pp. 780-781.
- [92] Y. Ueda, S. Nakamura, K. Utaka, T. Shiota, and T. Kitatani, "Very-low-current and high-speed switching operation of InAlGaAs/InAlAs/InP Mach-Zehnder interferometer-type photonic switch," *Appl. Phys. Express*, vol. 1, no. 9, Sep. 2008.
- [93] G. Wenger, M. Schienle, J. Bellermaun, M. Heinbach, S. Eichinger, J. Muller, B. Acklin, L. Stoll, and G. Muller, "A completely packaged strictly nonblocking 8x8 optical matrix

- switch on InP/InGaAsP," *J Lightwave Technol.*, vol. 14, no. 10, pp. 2332-2337, Oct. 1996.
- [94] D. Thomson, F. Y. Gardes, G. Z. Mashanovich, A. P. Knights, and G. T. Reed, "Using SiO₂ carrier confinement in total internal reflection optical switches to restrict carrier diffusion in the guiding layer," *J Lightwave Technol.*, vol. 26, no. 9-12, pp. 1288-1294, May-Jun. 2008.
- [95] J. Van Campenhout, W. Green, and Y. Vlasov, "Broadband digital optical switches based on a SOI Mach-Zehnder lattice," in *The 21st Annual Meeting of the IEEE Lasers and Electro-Optics Society*, Newport Beach, CA, USA, 2008, pp. 386-387.
- [96] M. Kohtoku, K. Kawano, S. Sekine, H. Takeuchi, N. Yoshimoto, M. Wada, T. Ito, M. Yanagibashi, S. Kondo, Y. Noguchi, and M. Naganuma, "High-speed InGaAlAs-InAlAs MQW directional coupler waveguide switch modules integrated with a spotsize converter having a lateral taper, thin-film core, and ridge" *J Lightwave Technol.*, vol. 18, no. 3, pp. 360-369, Mar. 2000.
- [97] N. Yoshimoto, Y. Shibata, S. Oku, S. Kondo, Y. Noguchi, K. Wakita, and M. Naganuma, "Fully polarisation independent Mach-Zehnder optical switch using a lattice-matched InGaAlAs/InAlAs MQW and high-mesa waveguide structure," *Electron. Lett.*, vol. 32, no. 15, pp. 1368-1369, Jul. 1996.
- [98] Y. Chiu, J. Zou, D. D. Stancil, and T. E. Schlesinger, "Shape-optimized electrooptic beam scanners: Analysis, design, and simulation," *J Lightwave Technol.*, vol. 17, no. 1, pp. 108-114, Jan 1999.
- [99] T. Fujimura, T. Tanemura, and Y. Nakano, "Numerical and experimental study on beam-deflecting planar optical switch on InP," in *The 21st Annual Meeting of the IEEE Lasers and Electro-Optics Society*, Newport Beach, CA, USA, 2008, pp. 461-462.
- [100] M. Jarrahi, R. Fabian, W. Pease, D. A. B. Miller, and T. H. Lee, "Optical switching based on high-speed phased array optical beam steering," *Appl. Phys. Lett.*, vol. 92, no. 1, Jan 2008.
- [101] R. A. Meyer, "Optical beam steering using a multichannel lithium tantalate crystal," *Appl. Optics*, vol. 11, no. 3, pp. 613-616, Mar. 1972.
- [102] M. Mony, E. Bisailon, E. Shoukry, C. Ostafew, E. Grondin, V. Aimez, and D. V. Plant, "Reprogrammable optical phase array," *Appl. Optics*, vol. 46, no. 18, pp. 3724-3729, Jun. 2007.
- [103] F. Vasey, F. K. Reinhart, R. Houdre, and J. M. Stauffer, "Spatial Optical Beam Steering with an Algaas Integrated Phased-Array," *App. Optics*, vol. 32, no. 18, pp. 3220-3232, Jun. 1993.
- [104] Q. B. Chen, Y. Chiu, D. N. Lambeth, T. E. Schlesinger, and D. D. Stancil, "Guided-wave electrooptic beam deflector using domain reversal in LiTaO₃," *J Lightwave Technol.*, vol. 12, no. 8, pp. 1401-1404, Aug. 1994.
- [105] E. Shekel, D. Majer, G. Matmon, A. Krauss, S. Ruschin, T. McDermott, M. Birk, and M. Boroditsky, "Broadband testing of a 64x64 nanosecond optical switch," in *The 15th Annual Meeting of the IEEE Lasers and Electro-Optics Society*, 2002, Glasgow, Scotland vol.2 pp. 371-372.
- [106] A. K. Dutta, N. K. Dutta, and M. Fujiwara, *WDM technologies: passive optical components. Vol. II*. Amsterdam: Academic Press, 2003.
- [107] P. J. Duthie and M. J. Wale, "16x16 single chip optical switch array in lithium niobate," *Electron. Lett.*, vol. 27, no. 14, pp. 1265-1266, Jul. 1991.
- [108] K. Hamamoto, T. Anan, K. Komatsu, M. Sugimoto, and I. Mito, "1st 8x8 semiconductor optical matrix switches using GaAs/AlGaAs electrooptic guided-wave directional-couplers," *Electron. Lett.*, vol. 28, no. 5, pp. 441-443, Feb 1992.
- [109] K. Hamamoto, S. Sugou, K. Komatsu, and M. Kitamura, "Extremely low-loss 4x4 GaAs/AlGaAs optical matrix switch," *Electron. Lett.*, vol. 29, no. 17, pp. 1580-1582, Aug 1993.

- [110] K. Komatsu, K. Hamamoto, M. Sugimoto, A. Ajisawa, Y. Kohga, and A. Suzuki, "4x4 GaAs/AlGaAs optical matrix switches with uniform device characteristics using alternating delta beta electrooptic guided-wave directional-couplers," *J Lightwave Technol.*, vol. 9, no. 7, pp. 871-878, Jul. 1991.
- [111] S. Cao, J. Noad, L. Sun, R. James, D. Coulas, G. Lovell, and E. Higgins, "Small half-wave voltage for MZI-based GaAs/GaAlAs electro-optic modulators/switches with coplanar electrodes," in *The 21st Annual Meeting of the IEEE Lasers and Electro-Optics Society*, Newport Beach, CA, USA, 2008, pp. 188-189.
- [112] R. M. Jenkins, J. M. Heaton, D. R. Wight, J. T. Parker, J. C. H. Birbeck, G. W. Smith, and K. P. Hilton, "Novel 1xN and NxN integrated optical switches using self-imaging multimode GaAs/AlGaAs wave-guides," *Appl. Phys. Lett.*, vol. 64, no. 6, pp. 684-686, Feb. 1994.
- [113] R. Krahenbuhl, R. Kyburz, W. Vogt, M. Bachmann, T. Brenner, E. Gini, and H. Melchior, "Low-loss polarization-insensitive InP-InGaAsP optical space switches for fiber optical communication," *IEEE Photon. Tech. Lett.*, vol. 8, no. 5, pp. 632-634, May 1996.
- [114] S. S. Agashe, K. T. Shiu, and S. R. Forrest, "Compact polarization-insensitive InGaAsP-InP 2x2 optical switch," *IEEE Photon. Technol. Lett.*, vol. 17, no. 1, pp. 52-54, Jan 2005.
- [115] M. G. Young, U. Koren, B. I. Miller, M. Chien, M. A. Newkirk, and J. M. Verdiell, "A compact 2x2 amplifier switch with integrated DBR lasers operating at 1.55 μm ," *IEEE Photon. Technol. Lett.*, vol. 4, no. 9, pp. 1046-1048, Sept. 1992.
- [116] A. A. M. Staring, L. H. Spiekman, C. vanDam, E. J. Jansen, J. J. M. Binsma, M. K. Smit, and B. H. Verbeek, "Space-switching 2.5Gbit/s signals using wavelength conversion and phased array routing," *Electron. Lett.*, vol. 32, no. 4, p. 377, Feb. 1996.
- [117] H. Buchta and E. Patzak, "Analysis of the physical impairments on maximum size and throughput of SOA-based optical burst switching nodes," *J Lightwave Technol.*, vol. 26, no. 13-16, pp. 2821-2830, Jul.-Aug. 2008.
- [118] F. Dorgeuille, L. Noirie, J. P. Faure, A. Ambrosy, S. Rabaron, F. Boubal, M. Schilling, and C. Artigue, "1.28 Tbit/s throughput 8x8 optical switch based on arrays of gain-clamped semiconductor optical amplifier gates," in *Optical Fiber Communication Conference*, Baltimore, MD, USA, 2000, vol.4 pp. 221-223.
- [119] A. Albores-Mejia, K. A. Williams, T. de Vries, E. Smalbrugge, Y. S. Oei, M. K. Smit, S. Anantathanasarn, and R. Notzel, "Scalable quantum dot optical switch matrix in the 1.55 μm wavelength range," in *International Conference on Photonics in Switching*, Sapporo, Japan, 2008, pp. 1-2.
- [120] M. Gustavsson, B. Lagerstrom, L. Thylen, M. Janson, L. Lundgren, A. C. Morner, M. Rask, and B. Stoltz, "Monolithically integrated 4x4 InGaAsP/InP laser amplifier gate switch arrays," *Electron. Lett.*, vol. 28, no. 24, pp. 2223-2225, Nov. 1992.
- [121] J. W. Lim, H. J. Kim, S. H. Kim, and B. S. Rho, "Multi-chip integration on a PLC platform for 16 x16 port optical switch using passive alignment technique," in *Electronic Components and Technology Conference*, San Diego, CA, USA, 2006, p. 5.
- [122] W. van Berlo, M. Janson, L. Lundgren, A. C. Morner, J. Terlecki, M. Gustavsson, P. Granstrand, and P. Svensson, "Polarization-insensitive, monolithic 4x4 InGaAsP-InP laser amplifier gate switch matrix," *IEEE Photon. Tech. Lett.*, vol. 7, no. 11, pp. 1291-1293, Nov. 1995.
- [123] Y. Yamada, H. Terui, Y. Ohmori, M. Yamada, A. Himeno, and M. Kobayashi, "Hybrid-integrated 4x4 optical gate matrix switch using silica-based optical waveguides and LD array chips," *J Lightwave Technol.*, vol. 10, no. 3, pp. 383-390, Mar. 1992.
- [124] M. Crisp, E. T. Aw, A. Wonfor, R. V. Penty, and I. H. White, "Demonstration of an SOA efficient 32x32 optical switch for radio over fiber distribution systems," in *Optical Fiber communication/National Fiber Optic Engineers Conference*, San Diego, CA, USA, 2008, pp. 1-3.

- [125] G. Nakagawa, Y. Kai, S. Yoshida, Y. Aoki, K. Sone, and S. Kinoshita, "High-speed and High-reliability Optical Selector for 256Å—256 Large-scale, Nanosecond-order Optical Switching," in *Optical Fiber communication/National Fiber Optic Engineers Conference*, San Diego, CA, USA, 2008, pp. 1-3.
- [126] R. Varrazza, I. B. Djordjevic, and Y. Siyuan, "Active vertical-coupler-based optical crosspoint switch matrix for optical packet-switching applications," *J Lightwave Technol.*, vol. 22, no. 9, pp. 2034-2042, Sept. 2004.
- [127] G. A. Fish, B. Mason, L. A. Coldren, and S. P. DenBaars, "Compact, 4x4 InGaAsP-InP optical crossconnect with a scaleable architecture," *IEEE Photon. Tech. Lett.*, vol. 10, no.9, pp. 1256-1258, Sept. 1998.
- [128] H. S. Hinton, *An introduction to photonic switching fabrics*. New York: Plenum Press, 1993.
- [129] S. D. Smith, A. C. Walker, F. A. P. Tooley, and B. S. Wherrett, "The demonstration of restoring digital optical logic," *Nature*, vol. 325, pp. 27-31, Jan 1987.
- [130] R. Katouf, T. Komikado, M. Itoh, T. Yatagai, and S. Umegaki, "Ultra-fast optical switches using ID polymeric photonic crystals," *Photonics Nanostruct*, vol. 3, no. 2-3, pp. 116-119, Dec. 2005.
- [131] Y. M. Liu, X. Xiao, P. R. Prucnal, and J. C. Sturm, "All-Optical switching in an asymmetric silicon Fabry-Perot etalon based on the free-carrier plasma effect," *Appl. Optics*, vol. 33, no. 18, pp. 3871-3874, Jun. 1994.
- [132] Y. Tang, A. Siahmakoun, G. Sergio, M. Guina, and M. Pessa, "Optical switching in a resonant Fabry-Perot saturable absorber," *J Opt a-Pure Appl Op*, vol. 8, no. 11, pp. 991-995, Nov. 2006.
- [133] C. S. L. Chun, "High speed low loss optical switch for optical communication systems," U.S. Patent 5 037 169, Aug.6 1991.
- [134] L. R. McAdams, R. N. McRuer, and J. W. Goodman, "Oblique-incidence liquid-crystal-tunable etalon," *Opt. Lett.*, vol. 16, no. 11, pp. 864-866, Jun. 1991.
- [135] F. Wang and G. H. Haertling, "Thin film ferroelectric light modulators," U.S. Patent 6 211 993, Apr. 3, 2001.
- [136] G. S. Buller, C. R. Paton, S. D. Smith, and A. C. Walker, "All-optical routing networks based on bistable interferometers," *Appl. Phys. Lett.*, vol. 53, no. 25, pp. 2465-2467, Dec 1988.
- [137] R. W. Adair, G. A. Clarke, B. P. Hichwa, C. Iaconis, D. G. Jensen, S. C. Olson, J. W. Seeser, and B. L. Swaby, "Fabry-Perot optical switch" U.S. Patent 6 490 381, Dec. 3, 2002.
- [138] M. V. Kotlyar, L. O'Faolain, A. B. Krysa, and T. F. Krauss, "Electrooptic tuning of InP-based microphotonic Fabry-Perot filters," *J. Lightwave Technol.*, vol. 23, no. 6, pp. 2169-2174, Jun. 2005.
- [139] F. Riboli, N. Daldosso, G. Pucker, A. Lui, and L. Pavesi, "Design of an integrated optical switch based on liquid crystal infiltration," *IEEE J Quant. Elect.*, , vol. 41, no. 9, pp. 1197-1202, Sept. 2005.
- [140] N. L. Taranenko, S. C. Tenbrink, K. Hsu, C. M. Miller, and B. Yufei, "Use of a fiber Fabry-Perot tunable filter for high-speed optical packet switching: towards an experimental prototype," in *Proc. SPIE - Int. Soc. Opt. Eng. USA*, 1998, vol. 3283, pp. 883-93.
- [141] S. Gulde, A. Jebali, and N. Moll, "Optimization of ultrafast all-optical resonator switching," *Opt. Express*, vol. 13, no. 23, pp. 9502-9515, Nov 2005.
- [142] B. G. Lee, A. Biberman, P. Dong, M. Lipson, and K. Bergman, "All-optical comb switch for multiwavelength message routing in silicon photonic networks," *IEEE Photon. Technol. Lett.*, vol. 20, no. 9-12, pp. 767-769, May-Jun. 2008.
- [143] S. Y. Cho and R. Soref, "Interferometric microring-resonant 2x2 optical switches," *Opt. Express*, vol. 16, no. 17, pp. 13304-13314, Aug 2008.

- [144] P. Dong, S. F. Preble, and M. Lipson, "All-optical compact silicon comb switch," *Opt. Express*, vol. 15, no. 15, pp. 9600-9605, Jul 2007.
- [145] F. Gan, T. Barwicz, M. A. Popovic, M. S. Dahlem, C. W. Holzwarth, P. T. Rakich, H. I. Smith, E. P. Ippen, and F. X. Kartner, "Maximizing the thermo-optic tuning range of silicon photonic structures," in *Photonics in Switching*, San Francisco, CA, USA, 2007, pp. 67-68.
- [146] N. Sherwood-Droz, H. Wang, L. Chen, B. G. Lee, A. Biberman, K. Bergman, and M. Lipson, "Optical 4x4 hitless silicon router for optical Networks-on-Chip (NoC)," *Opt. Express*, vol. 16, no. 20, pp. 15915-15922, Sep. 2008.
- [147] M. Song, L. Zhang, L. Zou, J.-Y. Yang, R. G. Beausoleil, and A. E. Willner, "A three-ring-resonator electro-optical switch with reduced jitter and enhanced speed and extinction ratio," in *The 21st Annual Meeting of the IEEE Lasers and Electro-Optics Society*, Newport Beach, CA, USA, 2008, pp. 459-460.
- [148] Y. Vlasov, W. M. J. Green, and X. Fengnian, "High-Throughput Silicon Nanophotonic Deflection Switch for On-Chip Optical Networks," in *Optical Fiber communication/National Fiber Optic Engineers Conference*, San Diego, CA, USA, 2008, pp. 1-3.
- [149] Y. Kokubun, "Microring resonator device and its application to hitless wavelength selective switch circuit," in *International Nano-Optoelectronics Workshop*, Lake Saiko, Japan, 2008, pp. 38-39.
- [150] G. N. Nielson, D. Seneviratne, F. Lopez-Royo, P. T. Rakich, Y. Avrahami, M. R. Watts, H. A. Haus, H. L. Tuller, and G. Barbastathis, "Integrated wavelength-selective optical MEMS switching using ring resonator filters," *IEEE Photon. Tech. Lett.*, vol. 17, no. 6, pp. 1190-1192, Jun. 2005.
- [151] R. A. Soref and B. E. Little, "Proposed N-wavelength M-fiber WDM crossconnect switch using active microring resonators," *IEEE Photon. Technol. Lett.*, vol. 10, no. 8, pp. 1121-1123, Aug. 1998.
- [152] M. C. M. Lee and M. C. Wu, "Variable bandwidth of dynamic add-drop filters based on coupling-controlled microdisk resonators," *Opt. Lett.*, vol. 31, no. 16, pp. 2444-2446, Aug 2006.
- [153] B. E. Little, S. T. Chu, P. P. Absil, J. V. Hryniewicz, F. G. Johnson, E. Seiferth, D. Gill, V. Van, O. King, and M. Trakalo, "Very high-order microring resonator filters for WDM applications," *IEEE Photon. Technol. Lett.*, vol. 16, no. 10, pp. 2263-2265, Oct 2004.

Design Challenges in Integrated Fabry-Perot Optical Space Switches

3.1 Introduction

The design of a novel device always brings with it a series of challenges and trade-offs that must be evaluated and solved. To complement the brief introduction to integrated Fabry-Perot optical space switches given in chapter 1, the overview presented in this chapter highlights the issues faced during their development and the procedure followed in their design. The solutions to the challenges described here are discussed in more detail in the following chapters.

In the next section, the switch working principles are reviewed and they are followed by a discussion on the design challenges. Fig. 3.1 shows a schematic of the prototype implemented to demonstrate the novel switching device that identifies its different components and in which chapter their conception is explained.

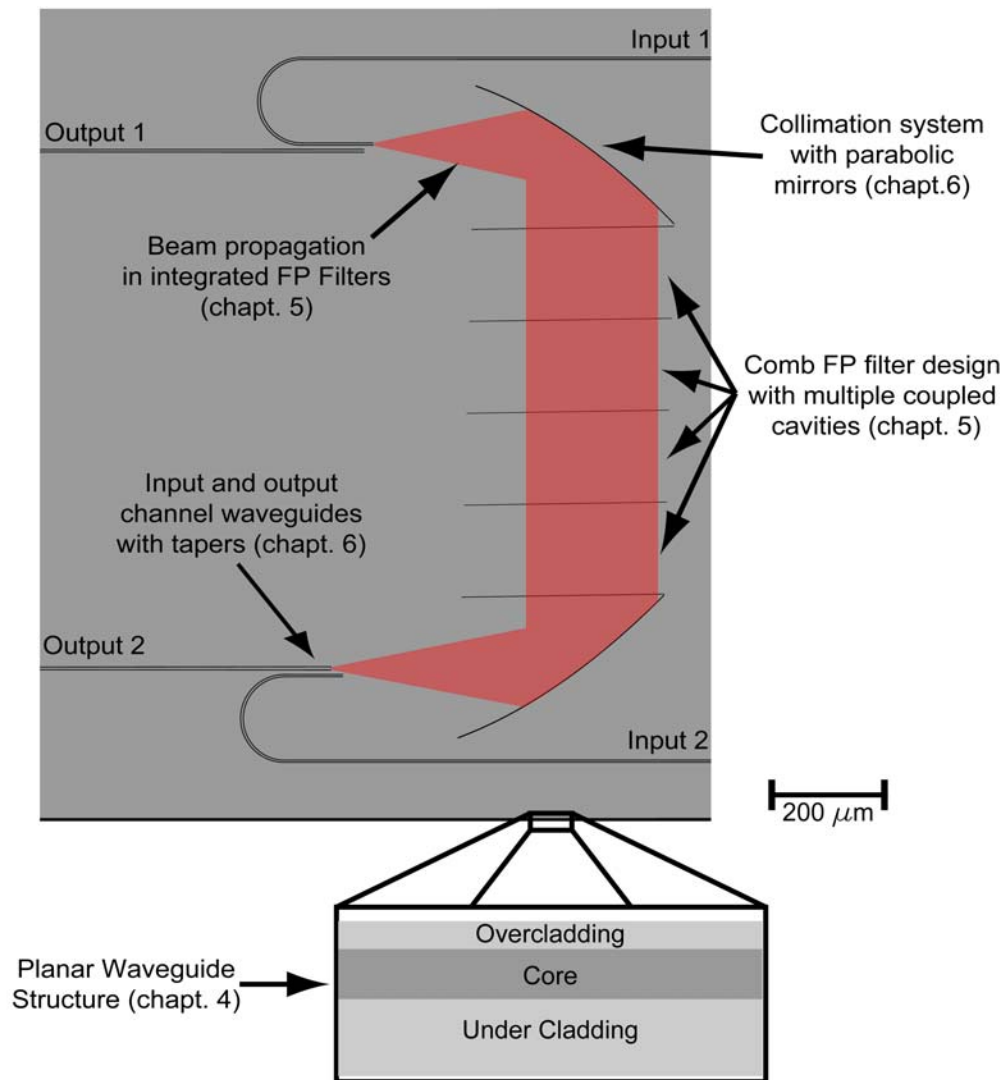


Fig. 3.1: Schematic of the integrated Fabry-Perot optical space switch demonstrator (to scale) showing the different challenges faced during its design.

3.2 Working Principles

In its simplest form, an integrated Fabry-Perot (FP) optical space switch can send an incoming beam to one of two output ports depending on the state of a tuneable Fabry-Perot filter (i.e. reflective or transmissive) with respect to the incident light wavelength. The filter is implemented in a planar waveguide, and since light is propagating at oblique incidence on the filter, no circulator is required to separate

the input and reflected beams, as is the case with the previous integrated FP filter implementations described in chapter 2. Furthermore, a single filter can form a 2x2 switch, as shown in Fig. 3.1, since inputs can be located on both side of the filter. Larger fabrics are obtained by using multiple filters laid out in ways similar to 2-D MEMS switches.

As explained in chapter 1, the next generation of optical networks will require fast optical switches to perform burst or packet switching. Therefore, the integrated Fabry-Perot optical space switch concept was developed to be compatible with electro-optic (EO) actuation. As a result, it is possible to change the switch state with the small refractive index modulation achievable with EO effects.

3.3 Design Challenges

Once the configuration of the switching element is found (a FP filter) and that the actuation mechanism is selected (EO effects), the first challenge in the investigation of integrated Fabry-Perot optical space switches is to choose a suitable material platform for their implementation. GaAs is preferred over LiNbO₃ and EO polymers because it can provide high index contrasts and planar waveguides are readily available. High index contrasts are obtained by etching through the planar waveguide. However, light propagating in the etched regions forming the filter mirrors experiences diffraction, which causes radiation losses. Therefore, the planar waveguide structure needs to be optimized to minimize these losses. A thorough study considering all the waveguide parameters and the dimensions of the etch regions is presented in chapter 4. The waveguide structure has to be determined before completion of the filter design because the effective refractive index of the waveguide is required to calculate the filter dimensions.

To build an efficient space switch, the FP filter must be able to work with multiple wavelength channels and its transmission passband should be broad and flat to avoid signal distortion. Unfortunately, EO effects can only shift a FP filter

transmission peak by approximately 1 nm, which is not sufficient to accommodate multiple channels. This problem is solved by reducing the free-spectral range of the FP filter to form a 200 GHz comb response. As a result, the filter transmits/reflects one out of every two wavelength channels on the ITU 100 GHz grid. Therefore, it is possible to change the switch state for all channels included in the comb filter response with the small shift in wavelength response provided by EO effects. Multiple channels can be switched as band of “even” or “odd” channels by a single device or they can be routed individually (each by a different filter) if they are demultiplexed before reaching the switch fabric. Switching bands of wavelengths could be useful in a router with multiple switching stages. For instance, one band of wavelengths could be forward directly to the next node while another is sent to a second switch fabric for further processing. Moreover, a 50 GHz passband is obtained by coupling several FP cavities. The filter design is explained in chapter 5 along with the impact of fabrication limits on its performance.

However, the filter is designed with the transfer matrix method, which assumes plane wave illumination. Thus, it is necessary to verify the filter response to the small beams used in integrated optics. This is a difficult task because light propagation in integrated Fabry-Perot switches is a 3-D problem. In the horizontal direction (i.e. parallel to the planar waveguide), the effect of oblique incidence on the filter must be considered while in the vertical direction the impact of radiation losses in the etched regions has to be accounted for. Unfortunately, no single simulation algorithm can model all of these aspects. The switches are too large to be simulated with the finite-difference time-domain method in 3-D and beam propagation algorithms cannot model interference occurring in the filter. Therefore, the switch design performance is evaluated by splitting the simulation problem in two. The effects of propagation through the filter on Gaussian beams are calculated by combining plane wave decomposition and the transfer matrix method whereas radiation losses are obtained with the

Eigenmode expansion method. The Eigenmode expansion method cannot simulate oblique incidence on the etched regions but since the angles used in integrated Fabry-Perot switches are small, the normal incidence results should closely represent what is taking place in the device. The analysis of Gaussian beam propagation in integrated filters leads to the development of an equation providing a lower limit on the Gaussian beam waist required to preserve the plane wave response of the filter and to avoid beam distortion. This investigation is included at the end of chapter 5. Furthermore, the minimum beam size needed to conserve the filter performance is sufficient to avoid issues of beam divergence inside the filter. Thus, horizontal confinement is not necessary in the filter.

The material presented in chapters 4 and 5 provides the basis necessary to implement an integrated Fabry-Perot optical space switch, which is the subject of chapter 6. Once the filter design and material are defined, the next challenge is to design a switch layout that is both practical and feasible. This requires the development of custom propagation and optimization software capable of both Gaussian beam propagation and interferometric simulations. The prototype fabrication will be done as much as possible within McGill facilities and thus the switch design has to be compatible with the equipment available. This imposes a number of limitations. First, every feature in the prototype has to have dimensions realizable with hard contact near UV photolithography. This fixes the minimum feature size to one micrometer. Only standard reactive ion etching is available and thus the etch depth is not as large as those possible with inductive coupled plasma etching. In the prototypes, integrated parabolic mirrors are used as collimation systems to obtain the large beams required to avoid distortion by the filter. Tapered channel waveguides are designed with beam propagation software to maximize coupling in and out of the chip. The prototypes are described in chapter 6 and it also presents experimental results, including wavelength response measurements and bit error tests.

Finally, the knowledge developed during the prototype design is used to evaluate the scalability of integrated Fabry-Perot optical space switches. Two architectures are considered, crossbar and shuffle Beneš. The challenge in developing large port count fabrics with integrated Fabry-Perot optical space switches is to find the optimal combination of incident angle and input beam waist that minimize the fabric area. More details are provided in chapter 7.

3.4 Conclusion

The development of the integrated Fabry-Perot optical space switch concept requires the investigation of planar waveguide structures, Fabry-Perot filter designs, and integrated optic layout and fabrication techniques. Issues of radiation losses, filter optimization, simulation approach, and fabrication limitations must to be solved to evaluate and demonstrate the novel device. This work requires the fabrication of switch prototypes, for which the optical response must be characterised. The scalability of integrated Fabry-Perot switch fabrics must also be evaluated.

Planar Waveguide Optimization

4.1 Introduction

Broadband mirrors are required in integrated Fabry-Perot optical space switches to maximize the number of wavelength channels with which they can operate. The mirrors are formed by etching completely through the planar waveguide, which provide the largest refractive index contrast possible (see Fig. 4.1). Unfortunately, beam expansion occurs in the regions where the waveguide is removed, leading to radiation losses. This problem has been extensively studied in the context of photonic crystals [1-6] and of high reflectance Bragg mirrors [7-14]. It was shown that both the waveguide index contrast [1-3, 6] and its layer structure [5, 6] need to be optimized to minimize losses. The trench geometry also plays an important role [4, 8, 11, 14, 15]. However, the previous reports only covered one or two of these features, and to the author's knowledge, this is the first study to consider them all simultaneously during waveguide optimization. Only the effects of conical or slanted wall trenches were not included.

This chapter is divided in two sections. First, the simulation technique used to study the impact of the different waveguide parameters is explained. Then, the simulation results are presented and analysed. It is demonstrated that the planar

waveguide structure and its refractive index contrast must be optimized concurrently to minimize radiation losses.

4.2 Simulation Technique

Fig. 4.1 illustrates the planar waveguide structure and defines the variables considered in the design optimization. Use of a GaAs/AlGaAs structure, in addition to being readily available, offers many degrees of freedom for planar waveguide optimization since the thickness and refractive index of every layer of the waveguide can be adjusted. The study presented below was carried out with the 2-D Eigenmode expansion algorithm described in [16] at a wavelength of 1550.12 nm (193.4 GHz). In the Eigenmode expansion method, the simulated structure is enclosed with artificial absorbing boundaries. The Eigenmodes of each longitudinally invariant section of the structure are solved for (up to a number fixed by the user), and at junctions between two different sections, the scattering properties are calculated by imposing the continuity of the tangential components to the complete set of Eigenmodes. With some algebraic manipulations, one gets a set of linear equations involving each possible modal pair made up of one mode from each structure. These equations are solved by computing an overlap integral over the modal pair and then solving for the transmission and reflection coefficients.

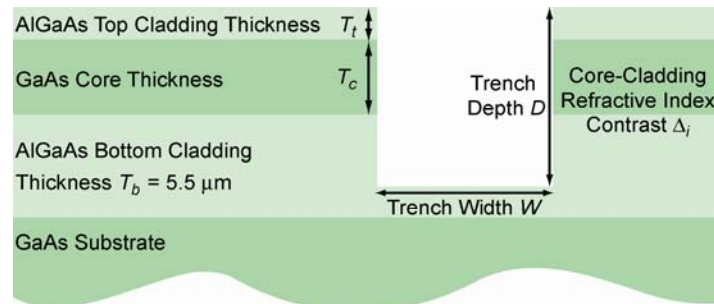


Fig. 4.1: Variables used in the planar waveguide optimization

Although the 2-D Eigenmode algorithm cannot model oblique incidence on Fabry-Perot (FP) filters, it is able to rapidly simulate a device with multiple coupled cavities at normal incidence. However, during the planar waveguide optimization a single trench was simulated to avoid variation in radiation losses resulting from a change in the frequency response of the device. As waveguide parameters are scanned, the propagation constant of the guided mode changes and thus the device response can switch between reflection and transmission. Because deep-etched trenches themselves act as FP cavities, transmitted wavelengths resonate within them, and the lack of confinement leads to radiation losses. On the other hand, light that is reflected from a trench quickly couples back into the waveguide and hence suffers less loss. In order to ensure that the simulations were always done with a trench maximizing transmission, and hence provided a worst case evaluation of radiation losses, the trench width was always equal to an integer number of half wavelengths. In their investigation on the effect of a waveguide index contrast on radiation losses, Bogaerts *et. al.* reported that there are two regimes in which low losses are achievable [3]. One is in low index contrast waveguides for which light is slowly diverging in etched areas, and the other is only attainable in semi-infinite periodic structures with high index contrast in which it is possible to couple to lossless Bloch modes. Since Bloch modes do not exist in FP filters, it is sufficient to consider a single trench and low index contrast to accurately optimize the waveguide structure.

An alternative to using a single trench would be to express the lengths of the device components in terms of wavelength and to adjust their physical dimensions according to the guided mode propagation constant at the beginning of each iteration. However, doing so with modal expansion methods requires careful adjustment of the simulation parameters since in the regions without waveguides most of the propagating light couples to high order modes that interact strongly with the simulation boundaries. As a result, the effective refractive index in the etched regions can be affected by the boundary conditions

and the difference in refractive index that this creates can change the state of the simulated device, especially if it has a narrow and sharp wavelength response.

4.3 Results and Analysis

The graphs in Fig. 4.2 show the radiation loss as a function of refractive index contrast and core thickness for a trench that is half a wavelength wide (at 1550.12 nm) and etched either 3 μm or 4 μm deep. For each index contrast and core thickness case, the top cladding thickness was varied between 0.5 μm and 3.0 μm and only the result from the most efficient configuration is reported in Fig. 4.2. The optimum waveguide designs vs. etch depth are given in Table 4.1. As the etch depth increases, the waveguide configuration that minimizes radiation losses requires a lower index contrast and a thicker core and top cladding. The optimum top cladding thickness as a function of index contrast and core thickness is shown in Fig. 4.3 for a 4 μm etch depth. As with the other etch depths, the top cladding thickness values for the best waveguides with 4 μm deep trenches are all well within the range of scanned values, which ensures that the optimization routine found the best solutions. Furthermore, single mode operation was verified for all waveguide configurations considered.

Table 4.1: Optimum GaAs/AlGaAs waveguide configurations vs. trench depth

Etch Depth (μm)	Single Trench Loss (%)	Refractive Index Contrast (%)	Cladding Aluminum Concentration (%)	Top Cladding Thickness (μm)	Core Thickness (μm)
2	16.6	2.31	14.6	0.0	1.55
3	6.5	1.04	7.2	0.0	2.35
4	3.3	0.68	5.0	0.5	2.55
5	1.9	0.49	3.8	0.8	2.95

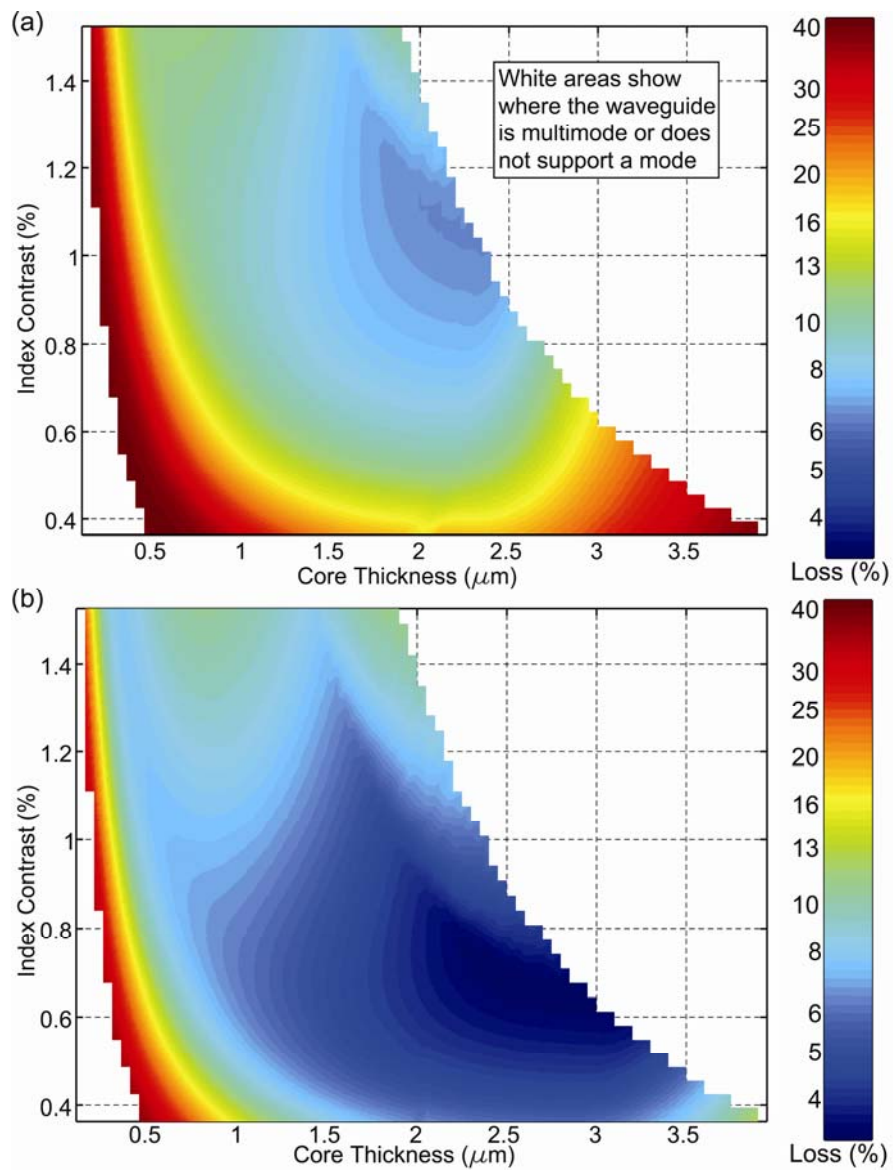


Fig. 4.2: Radiation loss vs. refractive index contrast and waveguide core thickness for (a) a 3 μm , and (b) 4 μm etch depth. The optimum top cladding thickness was found for each waveguide configuration.

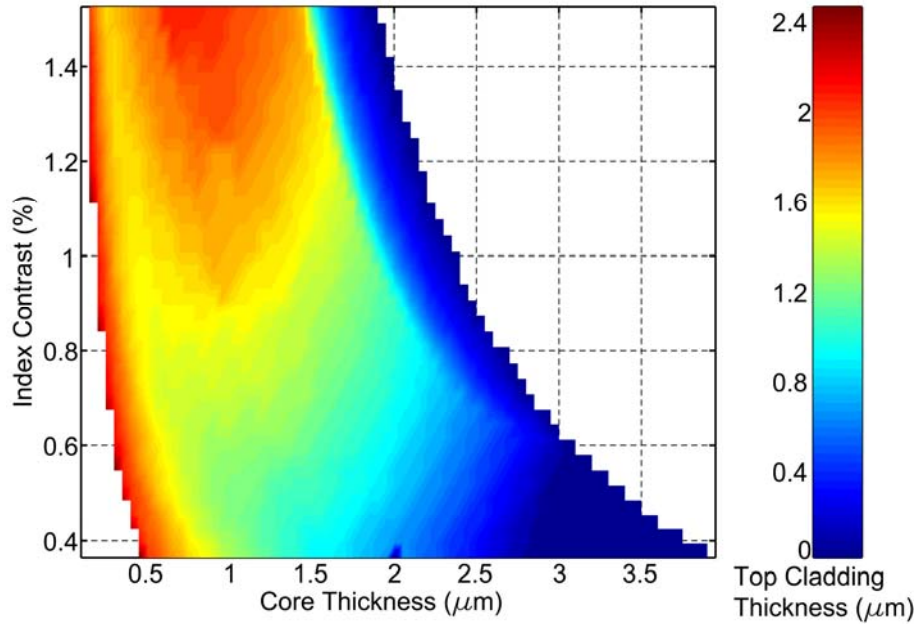


Fig. 4.3: Optimum top cladding thickness vs. refractive index contrast and waveguide core thickness for 4 μm deep and half a wavelength long trench.

The results shown in Fig. 4.2 illustrate the complex interactions that must be considered to minimize radiation losses when designing a waveguide. The divergence of the beam exiting the waveguide should be minimized to avoid light from radiating out of the trench. This is achieved by having a wide and smooth mode profile. On the other hand, the beam needs to be isolated from the trench floor where substrate leakage can occur, and this requires a compact mode profile. Thus, the optimum waveguide structure is the one that offers the least diverging mode profile that does not couple with the substrate. Furthermore, the fact that there is a unique optimum configuration of refractive index and waveguide layer thicknesses for each trench depth proves that both the width and shape of the waveguide mode are important. For instance, Fig. 4.4(a) shows two modes of equal width (measured at the $1/e^2$ intensity points) from different waveguides. The first waveguide has the optimum profile for a 4 μm deep trench (see Table 4.1) whereas the second one has a 0.81% index contrast with a 0.35 μm top cladding and 0.75 μm core. The optimum waveguide has radiation losses of 3.3 % whereas the other one suffers losses of 14.1 % after propagating through a half

wavelength trench that is $4\ \mu\text{m}$ deep. This difference can be explained in terms of the angular spectrums of the modes. The spectrum of the mode with the higher losses is wider (see Fig. 4.4(b)) and hence it has energy propagating at larger angles than the other mode. Also, since the optimum index contrast varies with the layer structure, both must be considered simultaneously to find the best waveguide configuration.

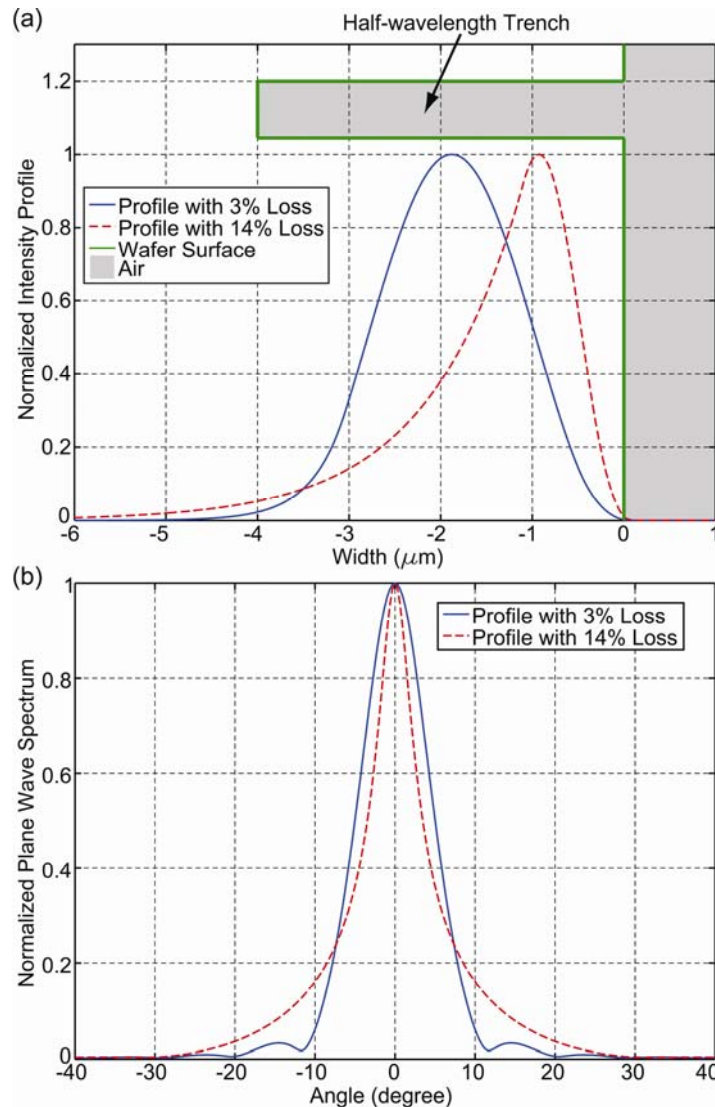


Fig. 4.4: (a) Two intensity profiles with the same $1/e^2$ width and (b) their angular spectrum. The blue line shows the profile for the optimum waveguide configuration for a $4\ \mu\text{m}$ trench described in Table 4.1. The red line is corresponds to a waveguide with an index contrast of 0.8%, a top cladding of $0.35\ \mu\text{m}$, and a core of $0.75\ \mu\text{m}$. Its radiation loss for a half-wavelength trench is 14%. The green line in (a) indicates the wafer surface and trench position with respect to the intensity profiles.

The reduction in radiation losses gained by etching deeper is shown in Fig. 4.5 and the effect of the cavity order is presented in Fig. 4.6. Radiation losses decrease exponentially with etch depth and they start to level off around 5 μm . As expected, losses increase with cavity order and they do so much more rapidly for shallow etch depths.

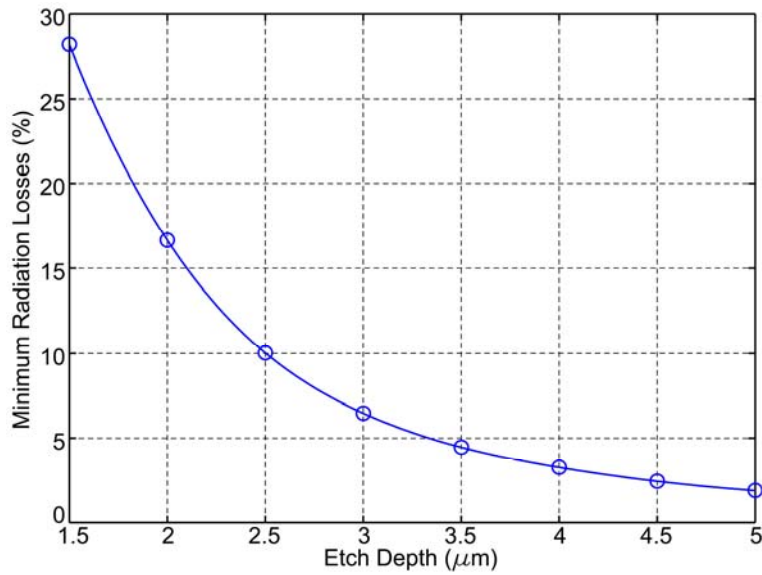


Fig. 4.5: Minimum radiation losses vs. etch depth for a first order trench.

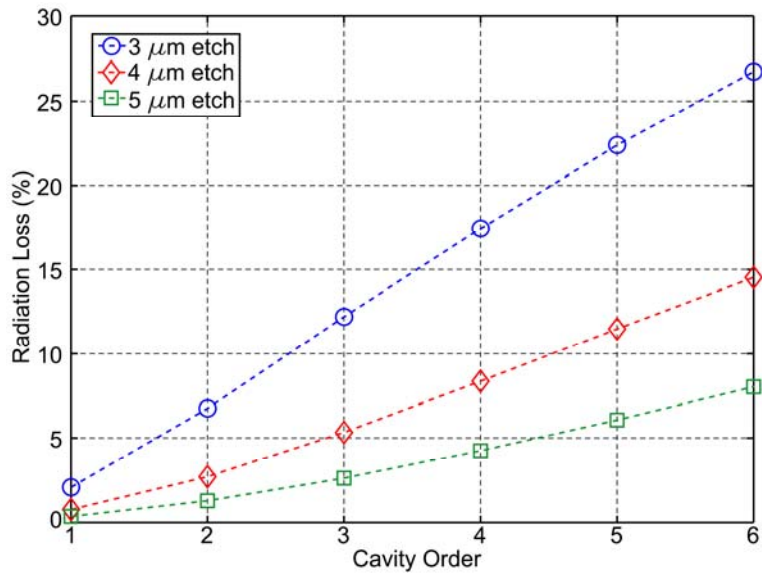


Fig. 4.6: Minimum radiation losses vs. trench width for different etch depth.

In addition to minimizing radiation losses, the planar waveguide must also be tolerant to variations in the fabrication process. As can be seen in Fig. 4.2, the optimum configuration for a 3 μm etch is at the limit at which the waveguide becomes multimode. Thus, it might be desirable to sacrifice some efficiency to improve fabrication tolerances. Moreover, Fig. 4.2 shows that tolerances increase for larger etch depths. If the maximum etch depth achievable is not exactly known before the growth of the waveguide, it is preferable to choose a waveguide design that is optimum for an etch depth shallower than expected. In Fig. 4.7 the radiation losses vs. etch depth are shown for the waveguide configurations given in Table 4.1. If a waveguide designed for a 5 μm etch depth is used but only 4 μm deep trenches are obtained, radiation losses will be 6.1% higher than with a waveguide optimized for 4 μm trenches. Conversely, if an etch depth of 5 μm is achieved with a waveguide structure designed for 4 μm trenches, radiation losses will only be 1.1% higher than with the optimum waveguide for that depth. Furthermore, these losses are compounded when multiple trenches are used, such as in the case of coupled-cavity FP filters, and thus it is important to find the best realizable waveguide configuration.

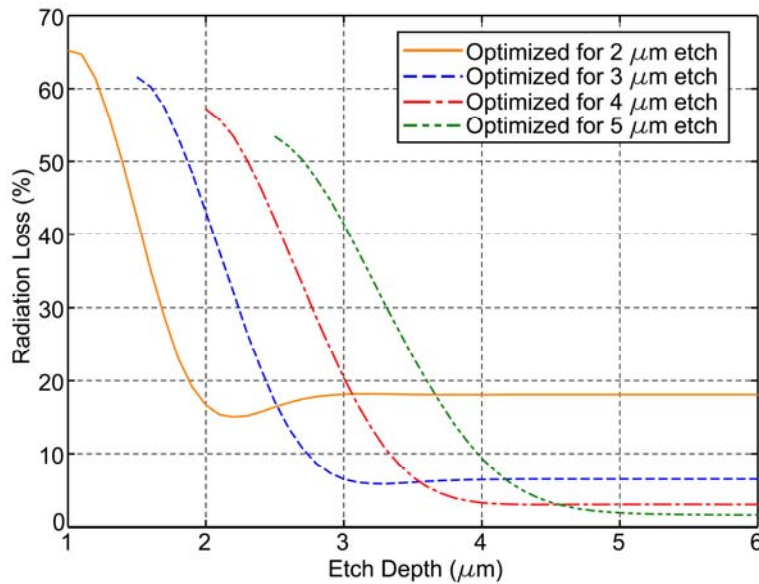


Fig. 4.7: Radiation losses vs. etch depth for the optimum waveguide configurations described in Table 4.1.

Radiation losses can be decreased at the expense of a reduction in reflectivity by filling the trenches with a low index material. For instance, the loss of a 4 μm deep and 1.55 μm wide trench can be reduced from 6.9 % to 2.2% by filling it with silicon dioxide even though that transforms a second order trench (when filled with air) into a third order one (with SiO_2 filling). Radiation losses can even be completely eliminated if a waveguide made of low index materials is formed inside the trenches, provided that the modes supported by both the high and low index waveguide match [2].

4.4 Conclusion

This study demonstrated that the index contrast and layer thickness of a planar waveguide must be considered simultaneously to minimize radiation losses. Furthermore, the depth of the etched features is also an important factor in the waveguide optimization. If at the time of growth of the epitaxial layers the maximum depth achievable is unknown, it is best to choose a waveguide configuration for a conservative estimation of the etch depth because the gain in efficiency provided by having the optimum waveguide for a deep etch are less than the loss suffered when the required depth is not obtained.

References

- [1] H. Benisty, D. Labilloy, C. Weisbuch, C. J. M. Smith, T. F. Krauss, D. Cassagne, A. Beraud, and C. Jouanin, "Radiation losses of waveguide-based two-dimensional photonic crystals: Positive role of the substrate," *Appl. Phys. Lett.*, vol. 76, no. 5, pp. 532-534, Jan. 2000.
- [2] S. Blair and J. Goeckeritz, "Effect of vertical mode matching on defect resonances in one-dimensional photonic crystal slabs," *J. Lightwave Technol.*, vol. 24, no. 3, pp. 1456-1461, Mar. 2006.
- [3] W. Bogaerts, P. Bienstman, D. Taillaert, R. Baets, and D. De Zutter, "Out-of-plane scattering in photonic crystal slabs," *IEEE Photon. Tech. Lett.*, vol. 13, no. 6, pp. 565-567, Jun. 2001.
- [4] G. W. Burr, S. Dizaiin, and M. P. Bernal, "The impact of finite-depth cylindrical and conical holes in lithium niobate photonic crystals," *Opt. Express*, vol. 16, no. 9, pp. 6302-6316, Apr. 2008.
- [5] R. Ferrini, A. Berrier, L. A. Dunbar, R. Houdre, M. Mulot, S. Anand, S. de Rossi, and A. Talneau, "Minimization of out-of-plane losses in planar photonic crystals by optimizing the vertical waveguide," *Appl. Phys. Lett.*, vol. 85, no. 18, pp. 3998-4000, Nov. 2004.
- [6] G. R. Hadley, "Out-of-plane losses of line-defect photonic crystal waveguides," *IEEE Photon. Technol. Lett.*, vol. 14, no. 5, pp. 642-644, May 2002.
- [7] K. J. Kasunic, "Design equations for the reflectivity of deep-etch distributed Bragg reflector gratings," *J. Lightwave Technol.*, vol. 18, no. 3, pp. 425-429, Mar. 2000.
- [8] T. C. Kleckner, D. Modotto, A. Locatelli, J. P. Mondia, S. Linden, R. Morandotti, C. De Angelis, C. R. Stanley, H. M. van Driel, and J. S. Aitchison, "Design, fabrication, and characterization of deep-etched waveguide gratings," *J. Lightwave Technol.*, vol. 23, no.11, pp. 3832-3842, Nov. 2005.
- [9] T. Kotani, Y. Hatada, M. Funato, Y. Narukawa, T. Mukai, Y. Kawakami, and S. Fujita, "Fabrication and characterization of GaN-based distributed Bragg reflector mirrors for low lasing threshold and integrated photonics," *Phys. Status Solidi C*, vol. 2, no. 7, pp. 2895-2898, May 2005.
- [10] M. V. Kotlyar, L. O'Faolain, A. B. Krysa, and T. F. Krauss, "Electrooptic tuning of InP-based microphotonic Fabry-Perot filters," *J. Lightwave Technol.*, vol. 23, no. 6, pp. 2169-2174, Jun. 2005.
- [11] C. Marinelli, M. Bordovsky, L. J. Sargent, M. Gioannini, J. M. Rorison, R. V. Penty, I. H. White, P. J. Heard, M. Benyoucef, M. Kuball, G. Hasnain, T. Takeuchi, and R. P. Schneider, "Design and performance analysis of deep-etch air/nitride distributed Bragg reflector gratings for AlInGaN laser diodes," *Appl. Phys. Lett.*, vol. 79, no. 25, pp. 4076-4078, Dec. 2001.
- [12] P. Modh, N. Eriksson, M. Q. Teixeira, A. Larsson, and T. Suhara, "Deep-etched distributed Bragg reflector lasers with curved mirrors-experiments and modeling," *IEEE J. Quantum Elect.*, vol. 37, no. 6, pp. 752-761, Jun. 2001.
- [13] S. Rennon, F. Klopff, J. P. Reithmaier, and A. Forchel, "12 μm long edge-emitting quantum-dot laser," *Electron. Lett.*, vol. 37, no. 11, pp. 690-691, May 2001.
- [14] H. K. Tsang, M. W. K. Mak, L. Y. Chan, J. B. D. Soole, C. Youtsey, and I. Adesida, "Etched cavity InGaAsP/InP waveguide Fabry-Perot filter tunable by current injection," *J. Lightwave Technol.*, vol. 17, no. 10, pp. 1890-1895, Oct. 1999.
- [15] G. R. Zhou, X. Li, and N. N. Feng, "Design of deeply etched antireflective waveguide terminators," *IEEE J. Quantum Elect.*, vol. 39, no. 2, pp. 384-391, Feb. 2003.
- [16] P. Bienstman and R. Baets, "Optical modelling of photonic crystals and VCSELs using eigenmode expansion and perfectly matched layers," *Opt. Quantum Electron.*, vol. 33, no. 4-5, pp. 327-341, Apr. 2001.

Integrated Off-Axis Fabry-Perot Filter Design

5.1 Introduction

Fabry-Perot (FP) interferometers have found application in many areas of science and engineering since their introduction in 1897 [1]. In optical telecommunications, they are commonly used as wavelength selective filters to isolate channels. In integrated Fabry-Perot optical space switches, FP filters operate as switchable reflectors that reflect or transmit light beams depending on the refractive index of their cavity. By using tuneable FP filters at oblique incidence, one can create optical space switches with layouts similar to 2-D MEMS switches but in which the switching mechanism can be thermo-optic, electro-optic, or all-optical (see Fig. 3.1). This way, it is possible to avoid speed limitations inherent to moving parts while having a simple and scalable architecture. However, FP filters must be carefully engineered to provide a wavelength response that is broad and sharp in order to offer transparency to bit rates.

The optimization presented in chapter 4 found the waveguide structures that minimized radiation losses as a function of etch depth. In this chapter, the effective refractive index of the optimum waveguide for the 4 μm etch depth (i.e. 3.367 at 1550 nm) is used in the transfer matrix method to design an FP filter suitable for a broadband switch. To take into account waveguide and material

dispersion in the filter design, the effective refractive index was obtained for wavelengths between 1527 nm and 1639 nm on a 0.1 nm interval. This chapter begins with a description of the filter configuration and of the performance requirements. Then the refinement of the filter structure is explained followed by the evaluation of the impact of the fabrication constraints. The chapter ends with an analysis of Gaussian beam propagation at oblique incidence in integrated FP filters, and a formula for the minimum Gaussian beam waist required as a function of incident angle is presented.

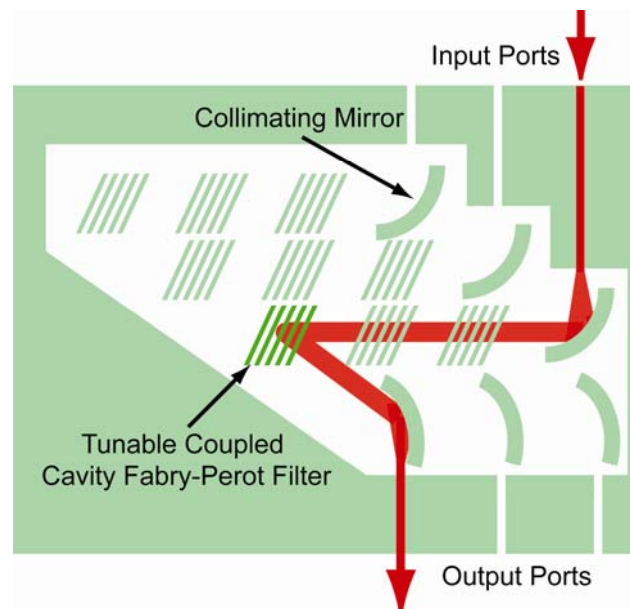


Fig. 5.1: Schematic of a 3x3 switch with tuneable coupled cavity Fabry-Perot filters in a crossbar configuration.

5.2 Filter Requirements

To create efficient space switches, the filter response must have a flat and wide passband with sharp transitions between its regions of high transmission and reflection. This is achieved by coupling multiple FP cavities [2-4]. Furthermore, to make the switch practical, it must work over a broad wavelength range. Unfortunately, the refractive index modulation provided by fast phenomena, such as electro-optic or non-linear optical effects, is too small to shift a FP filter

transmission peak over several channels. To extend the bandwidth over which the switch can operate, the filter free-spectral range (FSR) was designed to produce a comb response that transmits/reflects one out of every two channels on the desired frequency grid. One drawback of this technique is that FP filters lose their ability to work as demultiplexers. To demonstrate the integrated FP filter switch concept, a filter was designed to meet the following objectives:

- The clear transmission bandwidth (i.e. -0.5 dB) should be flat (i.e. ripples < 0.5 dB) have a linear phase, and be greater than 50 GHz;
- The comb response should have a 200 GHz pitch so that the switch is compatible with the 100 GHz ITU grid;
- The on/off ratio should be greater than 20 dB;
- The switch should work over the entire C-band;
- The switch has to work with only one polarization.

5.3 Filter Design

The relationships between the mirror reflectivity and the cavity length defined in [4] were used to obtain a preliminary design and to constrain the number of variables during optimization. Initially, the outer mirrors were made of a single trench whereas the inner ones had two since, according to [4], the inner mirrors must have a higher reflectivity than the outer ones. This design was refined using a commercial software based on the transfer matrix method (TMM) in which the planar waveguide was modeled by its effective refractive index. The principle behind the TMM is to solve the differential formulation of Maxwell equations by assuming plane wave illumination on a stack made of layers with different refractive index. The TMM uses the continuity of the tangential fields as boundary conditions. The resulting equations are then cast in matrix formalism. A complete derivation is available in [3, 5]. By using tensors for the permittivity and permeability, a general algorithm capable of handling anisotropic media can be obtained [6, 7].

It became apparent that a single trench would be sufficient to implement the inner mirrors since the widths of the two trenches used in the first design iterations were not close to a multiple of quarter wavelengths. Using only one trench to define the inner mirrors increased bandwidth by improving cavity coupling and reducing radiation losses. Bandwidth here is defined as the wavelength range over which the switch achieves an extinction ratio larger 20 dB. The design with mirrors made of two trenches has a maximum bandwidth of 36 nm and transmission losses of 0.9 dB whereas with mirrors having a single trench, the switch can cover the entire C-band (40 nm) and has a maximum loss of 0.2 dB, assuming a 5 μm etch depth. Furthermore, the tolerance to variations in trench width is higher for mirrors defined by a single trench, as shown in Fig. 5.2. To model accurately what takes place during fabrication, the width that was added/removed to a trench was removed/added to the neighbouring cavities. Variations larger than ± 20 nm destroyed the response of the switch implemented with mirrors having two trenches. Reducing the number of trenches in the inner mirrors doubled the tolerance to variations in width, as shown in Fig. 5.2(b). Also, errors in trench width that are consistent across the entire filter will shift its wavelength response up (for larger trenches) or down (for smaller trenches).

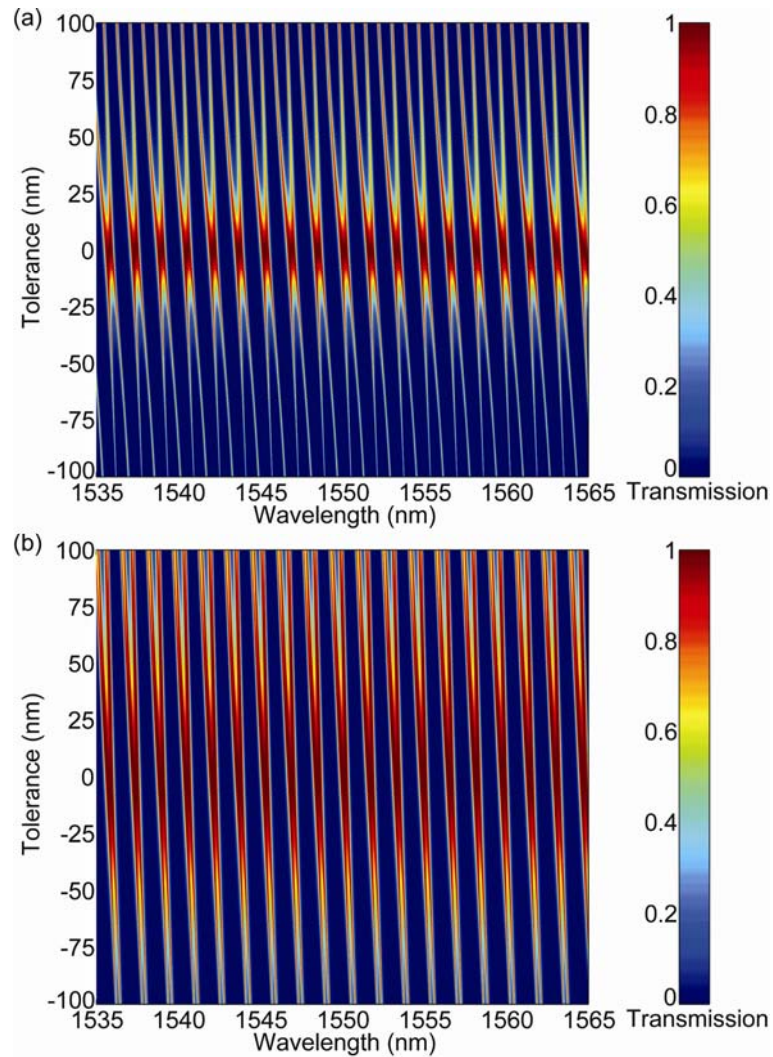


Fig. 5.2: Normalized transmission response of the filter as a function of the error in trench width for (a) a design with double trench mirrors and (b) a design with single trench mirrors.

Four cavities are needed to obtain a clear bandwidth greater than 50 GHz. This is more than 10 times the clear bandwidth of a single cavity comb filter with a similar rejection ration of the adjacent channels. Because of the small FSR required to get the desired comb response, the cavities needed to be long, which leads to large filters. Furthermore, as demonstrated in [2], the passband width decreases with increasing cavity order. Thus, more cavities are required in comb filters to obtain a 50 GHz passband than in single channel filters. However, small FSRs provide sharper responses for the same mirror reflectivity [8]. The increase

in passband gained by having multiple cavities provides many advantages that outweigh the increase in size. First, it allows the switch to handle signals with higher modulation rates. It is more tolerant to wavelength drift in input signals and to temperature variations [9]. Also, it relaxes the control needed on the switching mechanism. Although chromatic dispersion cannot be avoided in autoregressive filters [10], with careful design its peaks can be moved towards the passband edges and a region with low and linear dispersion can be achieved in the centre of the passband. Thus, a wide passband is useful to mitigate dispersion. Moreover, when designing FP filters, a trade-off must be made between the rejection ratio and dispersion. This is done by adjusting the mirror reflectivity. Fig. 5.3(a) shows the transmission spectrum of two filters with four coupled cavities but with different mirror reflectivity. The filter with the high reflectivity mirrors has a sharper response and a higher rejection of the adjacent channels but, as shown in Fig. 5.3(b), it suffers from stronger chromatic dispersion. Lastly, as explained below, a large passband allows small beams or beams with a greater angle of incidence to travel through the filter undistorted.

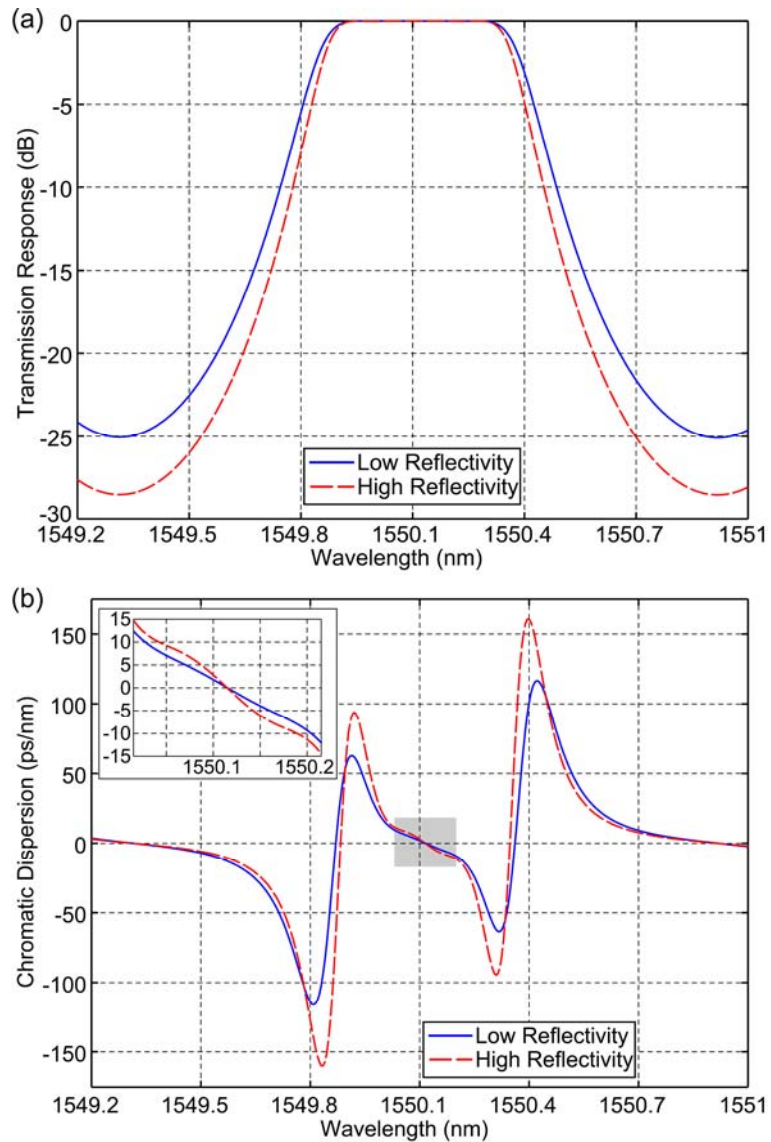


Fig. 5.3: (a) Transmission response and (b) chromatic dispersion for filters with different mirror reflectivity calculated with the TMM. The inset in (b) shows a zoom of the grey area. The filter with the low reflectivity is the 1st order design described in Table 5.1 below. At 1550.12 nm the mirror reflectivity is 10%, 51% and 66% for the 1st, 2nd and 3rd mirror, respectively. The 4th and 5th mirrors are identical to the 1st and 2nd. The high reflectivity filter has the same number of layers but the reflectivity of its 1st, 2nd and 3rd mirrors is 14%, 57% and 70% respectively.

5.4 Impact of Fabrication Constraints

In addition to meeting the performance requirements cited above, the filter design must also be compatible with the fabrication process. Table 5.1 shows the ideal dimensions for the four cavity design at normal incidence. Some trenches are very small and might not be realizable with a given fabrication process. One possible way to circumvent this issue is to increase the trench width by integer multiple of half wavelengths. However, this increases radiation losses, which in turn reduces the extinction ratio below 20 dB. It also increases the cavity coupling sensitivity to wavelength, which causes ripples in the passband that increase as the incident wavelength gets farther from the design value (see Fig. 5.4). Enlarging the trenches defining the filter mirrors from first to second order increases radiation losses by 0.87 dB in transmission and 0.49 dB in reflection when the filter is implemented with 4 μm deep trenches. For 5 μm trenches, the loss increase is 0.54 dB in transmission and 0.31 dB in reflection. The impact on the bandwidth is much worse since the range over which of the on/off ratio exceeds 20 dB decreased from the whole C-band (40 nm) to only 12 channels (8.8 nm) for both etch depth. If 3 μm trenches are used, the first order filter also works over the entire C-band, with losses of 0.65 dB and 0.12 dB in transmission and reflection, respectively. However, it is impossible to obtain 20 dB of extinction for any channels with the second order design at that etch depth. The maximum extinction ratio is 16.1 dB for transmitted channels. With the first order design, the bandwidth over which the extinction ratio is 20 dB starts to decrease for etch depths of less than 2 μm and disappears completely below 1.5 μm . Note that the losses and passband width reported in Table 5.1 are average values calculated by considering only the channels within the switch bandwidth.

Table 5.1: Characteristics of four cavity filters at normal incidence

Structure	Filter Region Type	Index	1st order mirrors Thickness (nm)	2nd order mirrors Thickness (nm)
1st mirror	Trench	1.000	55	1 605
1st cavity	Waveguide	3.367	210 873	210 413
2nd mirror	Trench	1.000	597	1 371
2nd cavity	Waveguide	3.367	210 821	210 839
3rd mirror	Trench	1.000	493	1 061
3rd cavity	Waveguide	3.367	210 821	210 839
4th mirror	Trench	1.000	597	1 371
4th cavity	Waveguide	3.367	210 873	210 413
5th mirror	Trench	1.000	55	1 605
Average Loss (dB) (transmission/reflection)	3 μm etch		0.65 / 0.12	NA
	4 μm etch		0.34 / 0.07	1.21 / 0.56
	5 μm etch		0.21 / 0.06	0.75 / 0.37
Passband Clear Bandwidth (GHz)	3 μm etch		52.6	NA
	4 μm etch		54.2	50.8
	5 μm etch		55.7	52.6
Switch Bandwidth (nm)	3 μm etch		> 40	0.0
	4 μm etch		> 40	8.8
	5 μm etch		> 40	8.8

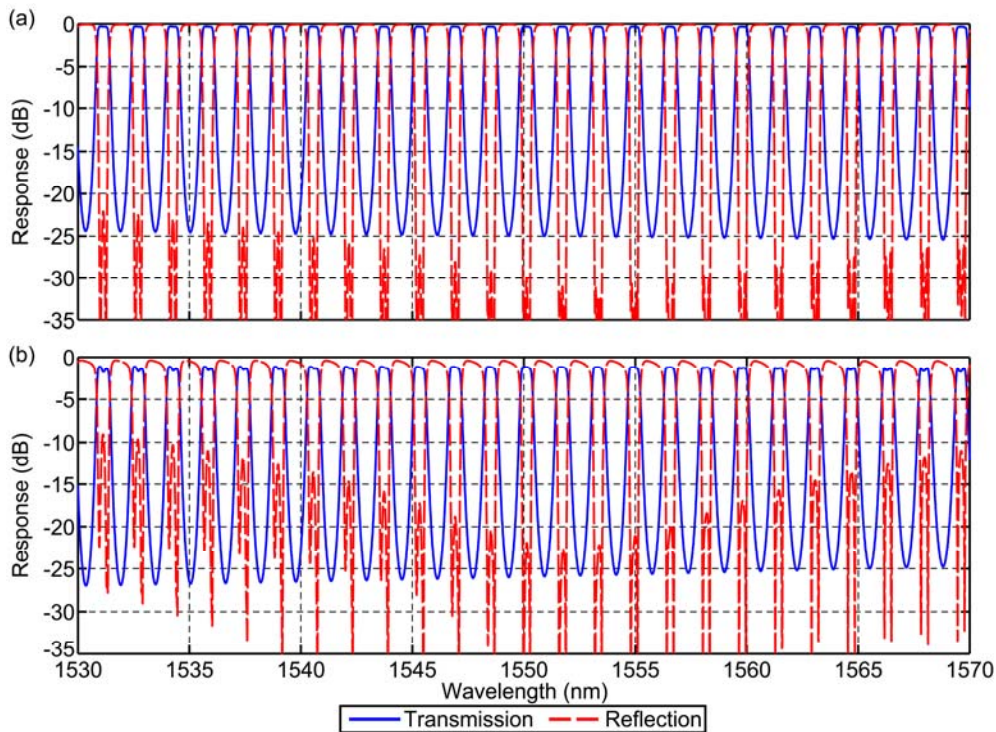


Fig. 5.4: Wavelength response in transmission and reflection for filters with (a) first and (b) second order mirrors.

Radiation losses not only reduce efficiency but also affect the wavelength response. The response of the filter described in Table 5.1 was calculated at normal incidence with the Eigenmode method for mirrors implemented with first and second order trenches (see Fig. 5.4). The radiation losses are slightly higher for the longer wavelengths of the passband, and this creates a slope in the passband.

5.5 Beam Propagation in Integrated Off-axis Filters

The filter wavelength response was designed assuming plane wave illumination at normal incidence, which is very different from the small beams used in integrated optics (see Fig. 5.5). To evaluate the impact of finite size beam on the filter response, Gaussian beams were propagated through the filter with the TMM by decomposing them into their angular components. Fig. 5.6 shows the filter wavelength response around 1550.12 nm for beams with different fractions of their angular spectrum power included within the clear bandwidth of the filter angular response. Even with 99.99% of the angular spectrum of the incident beam located within the clear bandwidth of the filter angular spectrum, the plane wave response is not completely recovered but it is enough to obtain a passband greater than 50 GHz. Once this relationship between the filter and the angular spectrum of the incident beam is established, it is possible to relate the angular bandwidth of the filter with the minimum beam waist required to avoid degradation of the filter response and beam distortion:

$$\omega_o = \frac{2 \cdot 1.945 \cdot \lambda_o}{\pi \theta n_{eff}} \quad (5.1)$$

where ω_o is the 1/e Gaussian beam waist, θ is the clear angular bandwidth of the filter in radians, and n_{eff} is the effective refractive index of the planar waveguide. The constant 1.945 is the beam waist multiplication factor within which 99.99% of the plane wave spectrum power in is contained for a one-dimensional Gaussian beam. The derivation of this equation is provided in appendix A. Although the

choice of 99.99% is probably a good rule of thumb for the ratio between a filter angular bandwidth and the angular spectrum of an incident Gaussian beam, the exact number required to recover the plane wave response of a filter is dependent on its response shape. The motivation to find a relationship between the filter and the beam angular spectrum is that the former changes with the angle of incidence. Hence, equation 5.1 provides a way to find the appropriate beam size as a function of incident angle.

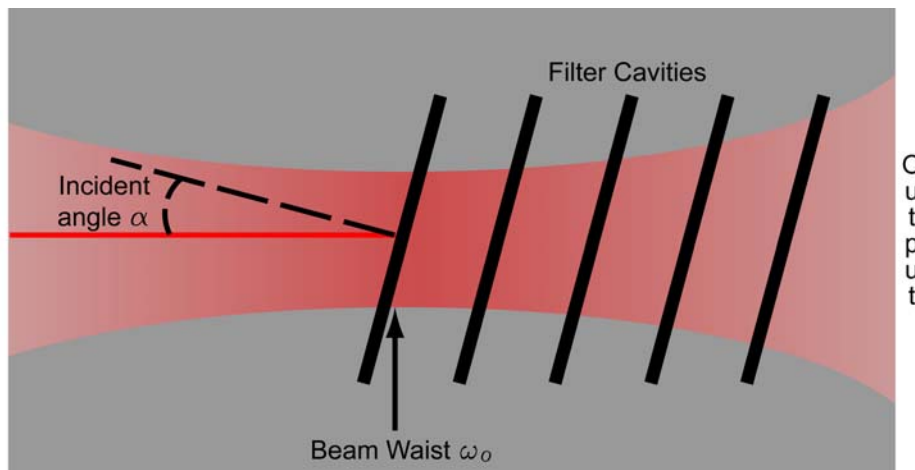


Fig. 5.5: Schematic showing Gaussian beam propagation in an integrated Fabry-Perot filter

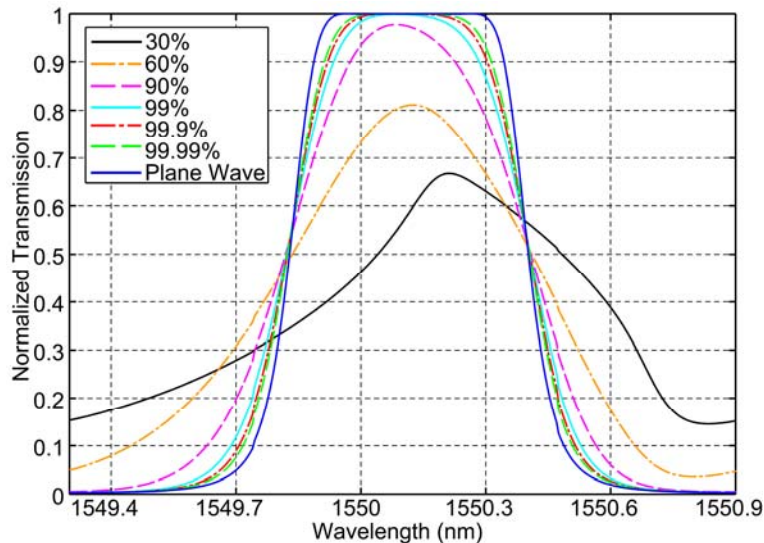


Fig. 5.6: Transmission efficiency vs. wavelength for input beams with different fractions of their angular spectrum within the clear bandwidth of the filter angular spectrum.

Although a filter wavelength response can be conserved as the angle of incidence is changed by scaling its normal incidence dimensions by one over the cosine of the new angle, the width of its angular response decreases rapidly as the incident angle increases. This is because the optical path difference caused by a given angular difference increases with the angle of incidence. The minimum beam waist required for undistorted propagation as a function of incident angle for the first order filter described in Table 5.1 is shown in Fig. 5.7. Because the increase in beam width is very rapid, the incident angle of the filter must be small to keep the beam size compatible with integrated optics. Adjusting the dimensions of the filter maintains the optical path difference between the interfering beams but it does not compensate for the changes in reflectivity at the interfaces, and thus this limits the angular range over which a given design can be used. That is why the curve in Fig. 5.7 approaches an asymptote for angles larger than 10 degrees. In that range the filter response widens because the filter phase is altered by the variations in reflectivity. Also, the maximum incident angle is limited by total internal reflection (TIR) between guided and etched regions. For GaAs-air interfaces, TIR occurs for incident angle larger than 17.2° . Nevertheless, the filter angular bandwidth continues to decrease as the incident angle increases even if it is implemented with a lower index contrast, and thus, the constraint on the incident angle still exists for low index contrast filters.

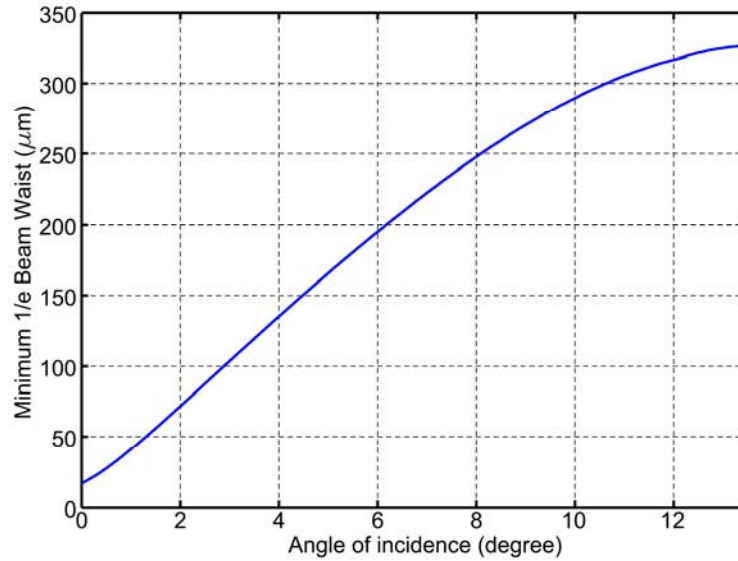


Fig. 5.7: Minimum 1/e Gaussian beam width for undistorted propagation through the four cavity filter described in Table 5.1 as a function of incident angle.

In previous studies of Gaussian beam propagation in thin-film filters, four impairments were identified [11-14]: lateral beam shift, waist magnification, angular shift, and focal shift. Lateral beam shift, which is the difference in the beam centroid position between that predicted by simple ray propagation and that created by interference, increases with the incident angle and must be taken into account when positioning the input and output ports of a device including off-axis FP filters. However, the waist magnification, angular shift, and focal shift caused by the FP filters described here are well below one percent of their original values. According to [13], nonspecular phenomena in multilayer dielectric stacks are significant in the regime in which their responses vary rapidly. Therefore, the wide and flat passband provided by the coupled cavities attenuates these undesired effects. At oblique incidence, the filter response may vary with polarization. This is the case with the FP filter presented here and it was optimized to work only with the TE polarization of the planar waveguide. Furthermore, working off-axis can lead to polarization conversion. To evaluate whether this occurred in these integrated filters, their wavelength response was simulated with the TMM formulation developed by Hodgkinson and Wu [6], and it predicted that no polarization conversion would take place.

5.6 Comparison with Experimental Results

In order to verify the design and optimization approach developed here, simulated results are compared with experimental ones obtained from the prototypes described in chapter 6 and fabricated using the process explained in appendix B. The dimensions of the fabricated device were measured from scanning electron micrographs, and they were used with the Eigenmode method to simulate the prototype wavelength response (see Fig. 5.8). No other fitting parameters were used. As shown in Table 5.2, over-etching increased the width of the trenches and it shifted the prototype response to the L-band and reduced cavity coupling. Furthermore, second order trenches were used to implement the filter mirrors in the prototype to satisfy the minimum feature size requirement of the photolithographic process. The shape of the simulated wavelength responses is similar to the experimental one, which indicates that the simulation approach is valid. Unfortunately, misalignments of the input and output waveguides caused significant insertion loss, and thus the radiation losses cannot be compared directly. The results in Fig. 5.8 were adjusted by subtracting the collimation system loss measured without the presence of a filter. Nevertheless, the average loss difference between the transmitted and reflected signals predicted by the Eigenmode method (0.9 dB) and measured experimentally (1.2 dB) agree. More details on the prototype wavelength response are presented in chapter 6.

Table 5.2: Designed and measured trench width.

Trench	Expected Width (nm)	Measured Width (nm)	Difference	
			(nm)	%
1	1 610	1 647	37	2.3
2	1 373	1 459	86	6.3
3	1 267	1 294	25	2.1
4	1 373	1 459	86	6.3
5	1 610	1 635	25	1.6

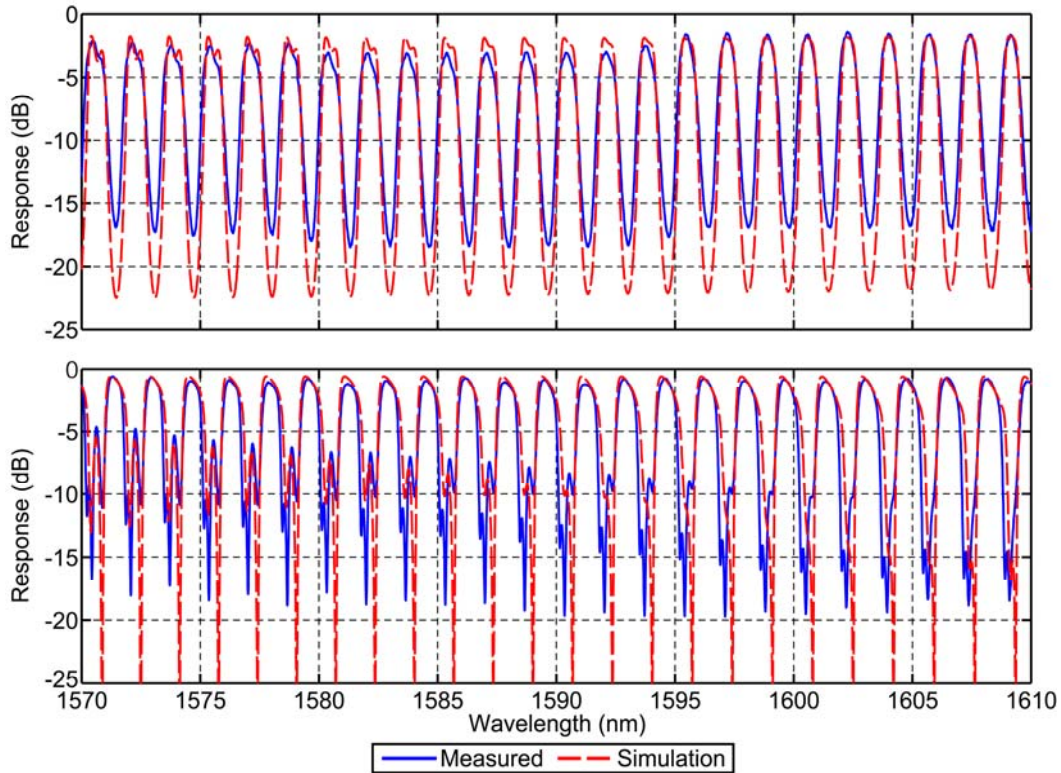


Fig. 5.8: Prototype wavelength response measured experimentally and simulated with the Eigenmode expansion method in (a) transmission and (b) reflection.

5.7 Conclusion

This chapter presented the approach used to develop a FP filter designed as a tuneable reflector for broadband integrated optical space switches. An initial design was conceived from previous work on multi-mirror FP interferometers and was later refined with a commercial thin film design software. This led to a device containing four coupled cavity filters with a 200 GHz comb response, a transmission passband larger than 50 GHz, and a theoretical on/off ratio greater than 20 dB over the entire C-band. The clear bandwidth obtained with multiple cavities is over an order of magnitude larger than for a filter with a single cavity. Having a wide passband allows the filter to handle higher bit rates and makes it more tolerant to wavelength drift in the input signal. Although mirrors implemented with first order trenches provide better cavity coupling and a larger

bandwidth, a design with larger second order trenches was conceived to be compatible with fabrication tools available at the McGill microfabrication laboratory. However, having larger trenches reduced the bandwidth by 82% and increased the transmission and reflection losses by 0.6 dB and 0.3 dB, respectively, for 5 μm deep trenches.

Working off-axis requires that careful attention be paid to the incident beam size because the angular spectrum of FP filters decreases quickly with increasing incident angle. To avoid distortion, including waist magnification, focal shift, and angular shift, 99.99% of the beam angular spectrum must be included in the clear bandwidth of the filter angular spectrum. However, lateral beam shift is always present and it must be considered in the switch layout.

Using the TMM for filter optimization and combining it with Eigenmode expansion to evaluate radiation losses is a valid approach to design integrated off-axis filters, as it was demonstrated by comparing simulation results with experimental data. Thanks to its comb response, the filter presented here can work with multiple wavelength channels and requires only a refractive index modulation of 0.053% to switch between reflection and transmission.

References

- [1] C. Fabry and A. Perot, "Sur les franges des lames minces argentées et leur application à la mesure de petites épaisseurs d'air," *Ann. Chim. Phys.*, vol. 12, pp. 459-501, 1897.
- [2] C. Ciminelli, F. Peluso, and M. N. Armenise, "2D guided-wave photonic band gap single and multiple cavity filters," in *Proceedings of 2005 IEEE/LEOS Workshop on Fibers and Optical Passive Components*, Taipei, Taiwan, pp. 404-409.
- [3] H. A. Macleod, *Thin-film optical filters*, 3rd ed. Philadelphia, PA: Institute of Physics, 2001.
- [4] H. Vandestadt and J. M. Muller, "Multimirror Fabry-Perot Interferometers," *J Opt Soc Am A*, vol. 2, no. 8, pp. 1363-1370, Aug. 1985
- [5] M. Born and E. Wolf, *Principles of optics: electromagnetic theory of propagation, interference and diffraction of light*, 7th expanded ed. New York: Cambridge University Press, 1999.
- [6] I. J. Hodgkinson and Q. h. Wu, *Birefringent thin films and polarizing elements*. River Edge, NJ: World Scientific, 1997.
- [7] P. Yeh, "Electromagnetic propagation in birefringent layered media," *J. Opt. Soc. Am.*, vol. 69, no. 5, pp. 742-756, May 1979.
- [8] E. Hecht, *Optics*, 4th ed. Reading, MA: Addison-Wesley, 2002.
- [9] Y. Vlasov, W. M. J. Green, and F. Xia, "High-throughput silicon nanophotonic wavelength-insensitive switch for on-chip optical networks," *Nature Photonics*, vol. 2, no. 2, pp. 242-246, Apr. 2008.
- [10] C. K. Madsen and J. H. Zhao, *Optical filter design and analysis: a signal processing approach*. New York: Wiley, 1999.
- [11] K. D. Hendrix and C. K. Carniglia, "Path of a beam of light through an optical coating," *Appl. Optics*, vol. 45, no. 11, pp. 2410-2421, Apr. 2006.
- [12] R. E. Klinger, C. A. Hulse, C. K. Carniglia, and R. B. Sargent, "Beam displacement and distortion effects in narrowband optical thin-film filters," *Appl. Optics*, vol. 45, no. 14, pp. 3237-3242, May 2006.
- [13] T. Tamir, "Nonspecular Phenomena in Beam Fields Reflected by Multilayered Media," *J Opt Soc Am A*, vol. 3, no. 4. pp. 558-565, Apr. 1986.
- [14] T. Tamir and H. L. Bertoni, "Lateral Displacement of Optical Beams at Multilayered and Periodic Structures," *J Opt Soc Am*, vol. 61, no. 10, pp. 1397-1413, Oct 1971.

Optical Prototype Layout and Characterisation

6.1 Introduction

Two 2x2 prototypes of integrated Fabry-Perot optical space switches were built in GaAs/AlGaAs planar waveguides to validate and demonstrate the design and simulations presented in chapters 4 and 5. In order to simplify the fabrication process, only the optical system of the switch, which includes input and output channel waveguides, collimating mirrors and the filter, was implemented. To obtain fully functional electro-optic switches, the doping profile of the planar waveguide should be adjusted to form a P-I-N structure and ohmic contacts would have to be deposited on the switches. Nevertheless, the prototypes were characterised in both reflection and transmission for 50 wavelength channels on the 100 GHz ITU grid by using the thermo-optic effect as the switching mechanism. Bit error tests on signals reflected and transmitted by a prototype were also performed at 10 Gb/s.

This chapter begins with a description of the layout and of the components of the prototypes. Section 6.3 presents the results of the wavelength response measurements along with the characterisation of the ITU channels, which includes insertion loss, crosstalk, and extinction ratio. The bit error rate tests are reported in section 6.4. Further details on the fabrication process, including explanations on the mask design and etch recipe, are provided in appendix B.

6.2 Prototype Layout

The light path in the devices is as follows (see Fig. 6.1(a)). The light from a lensed fibre is coupled into a channel waveguide on the left side of the die. An 180° curve was introduced to position the inputs and outputs on opposite sides of the chip to simplify testing. The input waveguide terminates at the focal point of a total internal reflection (TIR) parabolic mirror used to collimate the beam that propagates in the planar waveguide. The collimated light is reflected at 90° and sent to the integrated Fabry-Perot switch, whose normal is tilted by 1.2° with respect to the direction of propagation of the beam. If the light is reflected by the filter, it is focused into an output channel waveguide placed just below the input by the same mirror that collimated it. Otherwise, when the input signal is transmitted by the filter, it is coupled into another output channel waveguide by a second parabolic mirror located on the other side of the filter. To obtain a 2x2 switch, a second input waveguide is added below that output. The trade-offs involved in the design of each component are explained below.

6.2.1 Planar Waveguide

The waveguide structure shown in Fig. 6.1(c) was grown by metal-organic chemical vapor deposition on n^+ GaAs substrates. It consists of a $0.6\ \mu\text{m}$ $\text{Al}_{0.06}\text{Ga}_{0.94}\text{As}$ over cladding, a $2.1\ \mu\text{m}$ GaAs core, and a $5.5\ \mu\text{m}$ $\text{Al}_{0.06}\text{Ga}_{0.94}\text{As}$ under cladding. The epitaxial layers were not doped since the prototypes were implemented to evaluate the optical design only. The refractive indices of the core and claddings are 3.374 and 3.345, respectively. The effective refractive index of the planar waveguide is 3.365 for the TE polarization, which is the only one considered during the filter design. A 125 nm aluminum layer was deposited on the filters to simulate the presence of electrodes for future electrically controlled implementations of the switch. This aluminum layer accounted for any loss an electrode could induce. The refractive index and thickness of the epitaxial

layers were optimized to minimize radiation losses in the etched areas, as explained in chapter 4. In building the prototypes, a waveguide design with greater tolerance to variations in index contrast and over cladding thickness was selected in preference to the design with minimum radiation loss described in chapter 4, and a conservative $4\ \mu\text{m}$ estimate was assumed for the etch depth. This modification of the waveguide did not significantly increase radiation losses.

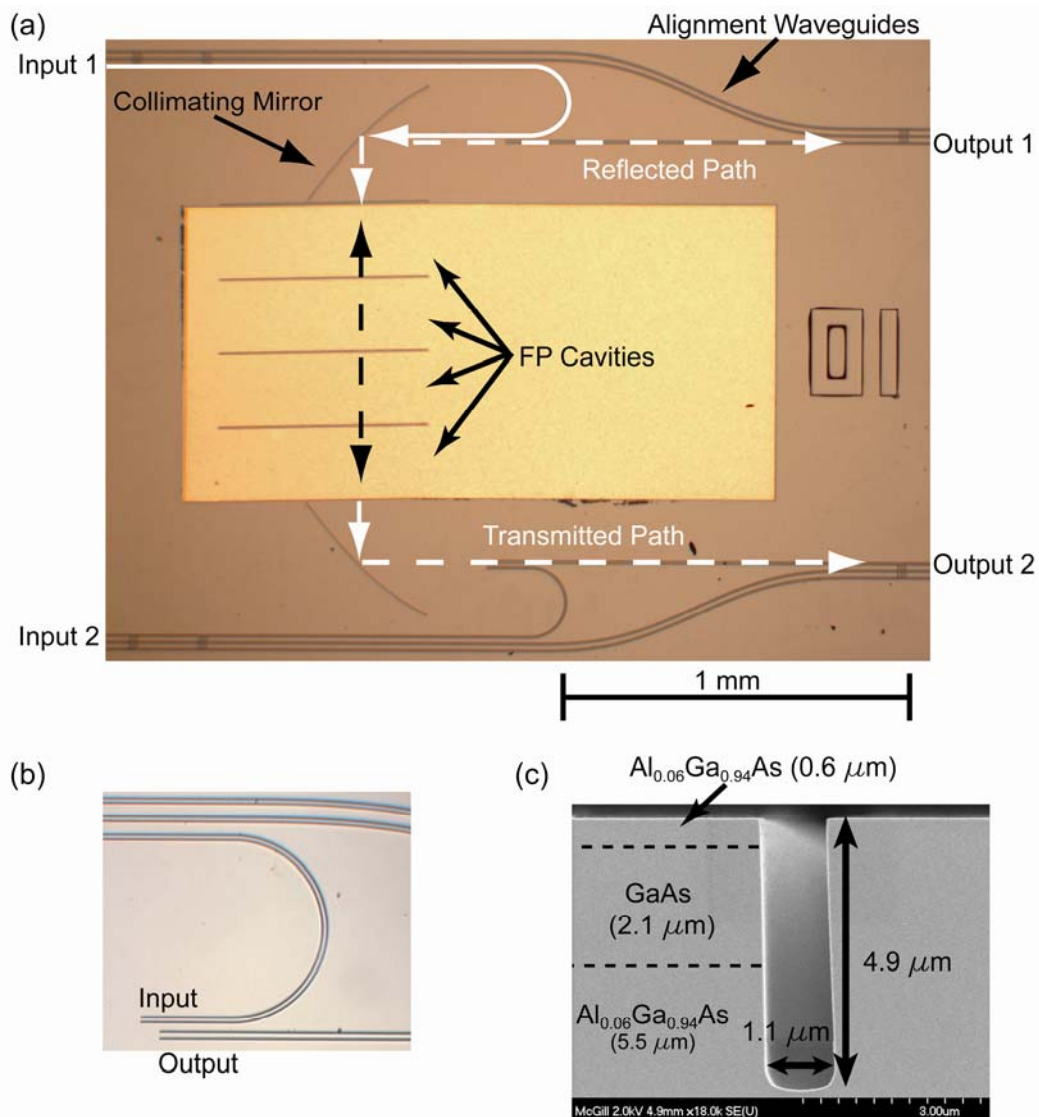


Fig. 6.1: Pictures of a switch prototype: (a) complete device, including alignment waveguides, (b) enlargement of the top input and output waveguides, and (c) SEM micrograph of the cross-section of a mirror defining the cavities showing the planar waveguide epitaxial layers.

6.2.2 Input and Output Channel Waveguides

Channel waveguides that are $3.0\ \mu\text{m}$ wide and defined by $2.0\ \mu\text{m}$ wide and $2.5\ \mu\text{m}$ deep trenches on each side are used to route the input and output signals to and from the collimating mirrors. A shallower etch depth was required to implement the channel waveguides because the deep etch used to form the filter and collimating mirrors would have created multimode waveguides even if their width was reduced to the minimum feature size of the photolithographic process (i.e. $1.0\ \mu\text{m}$). Thus, the channel waveguides and the filter had to be fabricated in separated etch, which introduced a critical alignment step. The channel waveguide was designed to optimize the overlap between the fundamental TE mode and a Gaussian beam. The optimum overlap is 97% with a Gaussian beam having a $1.1\ \mu\text{m}$ beam waist ($1/e$ radius). In addition to providing a high level of coupling with the lensed fibre, this ensures that the beam has a profile close to the Gaussian beam approximation assumed during the filter and collimating mirror design. A $0.7\ \text{dB/cm}$ propagation loss was measured experimentally with the cut back method for straight channel waveguides (see Fig. 6.2).

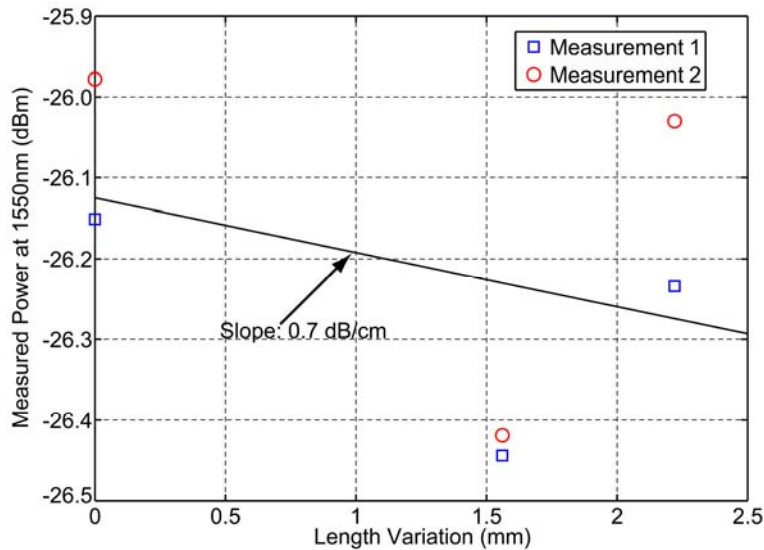


Fig. 6.2: Experimental results from the loss measurements with the cut-back method.

When the prototype is operated as a 2x2 switch, there is a slight difference in the location of the output beam waist at a given output waveguide depending on whether the filter is in transmission or reflection. This is because the interference taking place in the filter affects the beam differently depending on whether transmission or reflection occurs. Therefore, the output waveguides were tapered to accommodate these small variations in position. Beam propagation simulations indicated that the most efficient taper width was 3.5 μm . The tapering down to 3.0 μm was done linearly over 1.0 mm. This ensured that at least 92 % of the two possible output signals would couple into the channel waveguide. Similar tapers were used at the die edge to increase the alignment tolerance of the lensed fibres.

6.2.3 Collimating Mirrors

As explained in chapter 5, 99.99% of the plane wave power spectrum of the incident beam must be contained within the clear bandwidth of the filter angular response in order to preserve the filter wavelength response. Since the filter used here has an angular clear bandwidth of 0.7° , the incident beam must have a $1/e$ beam radius of at least 47.0 μm . In the prototypes, the beam radius was slightly larger (51.7 μm). Because of the large beam size required, TIR parabolic mirrors were chosen as the collimation system. The system should be as compact as possible, and this is achieved by locating the input beam at the mirror focal point. This can be derived from the magnification formula for a Gaussian beam [1]:

$$M = \frac{\omega_f}{\omega_i} = \frac{f}{\sqrt{x_i^2 + \left(\frac{\pi \omega_i^2}{\lambda}\right)^2}} \quad (6.1)$$

where M is the magnification; ω_i and ω_f are the initial and final $1/e$ beam waist radius; f is the focal length; x_i is the distance between the initial waist ω_i and the focal point; and λ is the wavelength in the waveguide. The distance between the input waist and the mirror is equal to x_i+f , and from equation (6.1) it is minimized

when x_i is zero for a given magnification. Under that condition, equation (6.1) can be simplified to find a straightforward relationship between the parabolic mirror focal length and the required input and output waist:

$$f = \frac{\pi \omega_f \omega_i}{\lambda}. \quad (6.2)$$

Using the parabola equation in polar coordinates:

$$r = \frac{2a}{1 + \cos(\theta)} \quad (6.3)$$

where a is the distance between the focus and the parabola apex (see Fig. 6.3) and θ is measured from the parabola axis of symmetry, it is possible to establish a relationship between the angle θ and the mirror focal length f_m since $a=2f_m$. Combining equations (6.2) and (6.3) gives the focal length required for the collimation system as a function of angle:

$$f_m(\omega_i, \omega_f, \theta) = \frac{\pi \omega_f \omega_i}{2\lambda} (1 + \cos(\theta)) \quad (6.4)$$

To simplify layout and to ensure total internal reflection at the waveguide-trench interface, the angle θ in equation (6.4) was set to 90° , which translated to a 45° angle of incidence (α) with respect to the parabola normal at that point. Thus, to enlarge the $1.1 \mu\text{m}$ beam from a channel waveguide to $51.7 \mu\text{m}$, a mirror with a focal length of $193.9 \mu\text{m}$ is needed. The operation of the parabolic mirrors was validated experimentally by observing the trenches for scattered light with an infrared camera but none was detected, as can be seen on Fig. 6.4.

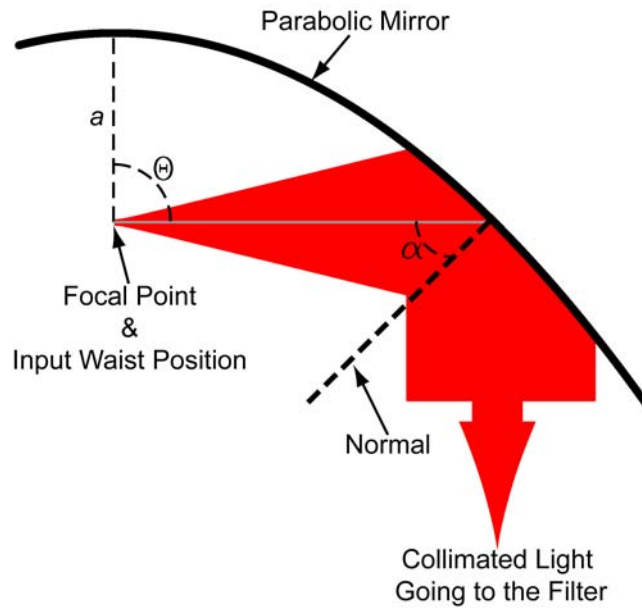


Fig. 6.3: Schematic illustrating the parabolic mirror layout

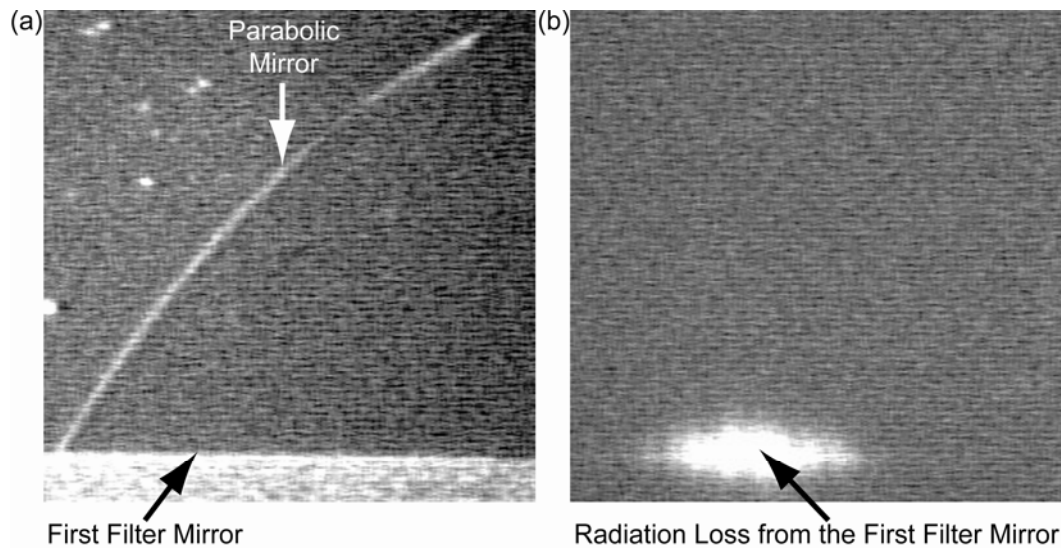


Fig. 6.4: Picture of a TIR parabolic mirror taken with (a) visible light illumination and (b) without external illumination. The bright spot visible in (b) is the infrared light that radiates out of the trench forming the first mirror of the filter. No infrared light is leaking from the parabolic mirror, which indicates that TIR is keeping light inside the planar waveguide.

6.2.4 Filter

The filter consists of four coupled high order cavities delimited by five mirrors, each made of a single second order deep-etched trench. The design dimensions are listed in Table 5.1. Second order trenches were used to implement the mirrors to satisfy the 1.0 μm minimum feature size of the photolithographic process. This increases radiation loss from 0.2 dB to 1.0 dB in transmission and from 0.1 dB to 0.4 dB in reflection, according to Eigenmode expansion simulations. However, the most significant consequence of using second order trenches is on the number of channels for which the theoretical extinction ratio is greater than 20 dB since it decreases from 50 (i.e. the entire C-band) to only 12, as explained in chapter 5. The small discrepancies between the switch performance reported here and those given in chapter 5 are caused by the difference in the number of channels considered for each analysis. In chapter 5, the performance was evaluated by considering only the channels with an extinction ratio greater than 20 dB, which is the criterion used to define the switch bandwidth. In this chapter, all 50 channels are taken into account to match the experimental data.

To obtain a compact device, the smallest incident angle at which the outputs are separated from the inputs must be found because the minimum beam waist required to maintain the plane wave response of the filter increases rapidly with the angle of incidence. Thus, having a small incident angle keeps the filter as narrow as possible. Furthermore, minimizing the beam width reduces the size and focal length of the parabolic mirrors. To compute the output position as a function of incident angle on the filter, the beams emitted from the input waveguides were propagated to the parabolic mirrors using Gaussian beam equations and ray tracing. However, to account for interference effects occurring inside the filter, such as lateral beam shift, waist magnification, and angular beam shift, the beams at the filter inputs were decomposed into their plane wave spectrum and propagated with the transfer matrix method described in [2]. This propagation algorithm was the basis of an optimization software that searched for

the most compact layout for the 2x2 switch as a function of input beam waist and filter angle. In addition to the output waist positions, it calculated the dimensions of the parabolic mirrors, as well as the filter width.

In the prototypes, the distance between the mirrors and the focal point is $388.4 \mu\text{m}$ (i.e. twice the focal length calculated in the previous section). The mirror and filter width must be at least $254 \mu\text{m}$ to capture 99.9% of the beams intensity but, as can be seen on Fig. 6.1(a), they have been extended to facilitate the measurement of their etch profile. An incident angle of 1.2° was sufficient to provide at least $10 \mu\text{m}$ of separation between the edge of the input and output beams (measured at the radius containing 99.9% of the beam power).

6.3 Prototype Characterization

Two identical dies, each having seven 2x2 switches with slightly different filter dimensions, were fabricated (see appendix B for fabrication details). All switches were tested and the performance of the best device on each die is reported. The optical response of the two selected prototypes was measured in transmission and reflection for channels on a 100 GHz grid in the L-band by modulating the filter refractive index with the thermo-optic effect. A schematic of the test set-up is shown in Fig. 6.5. To control the temperature of the devices, they were mounted on a custom holder with a thermo-electric cooler, and a thermistor was fitted on top of them. A temperature variation of 5.8°C was necessary to change the filter state for a given channel. The holder (shown in Fig. 6.6) was put on a manual alignment stage located between two piezoelectric stages on which polarization-maintaining (PM) tapered-lensed fibres were mounted. The polarization axes of the fibres were oriented along the TE polarization plane of the planar waveguide.

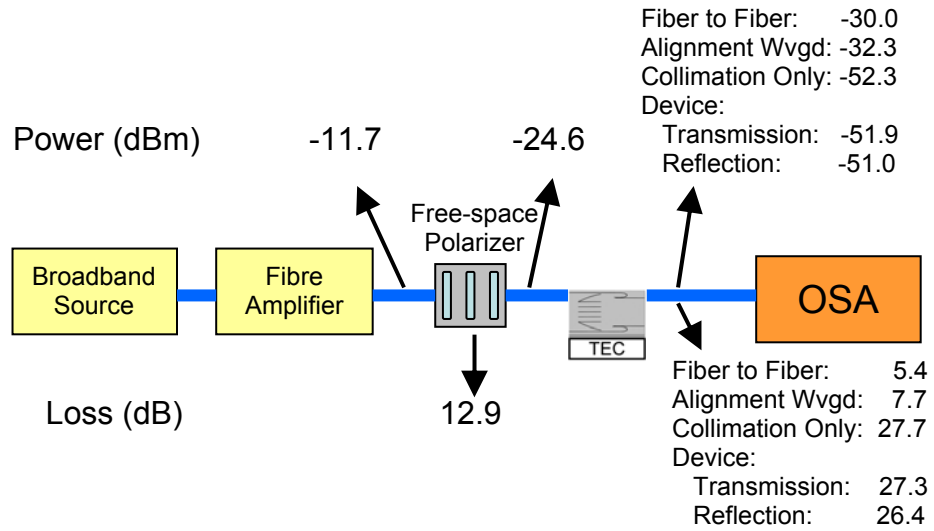


Fig. 6.5: Schematic of the experimental set-up used for the wavelength response measurements showing power levels and insertion losses.

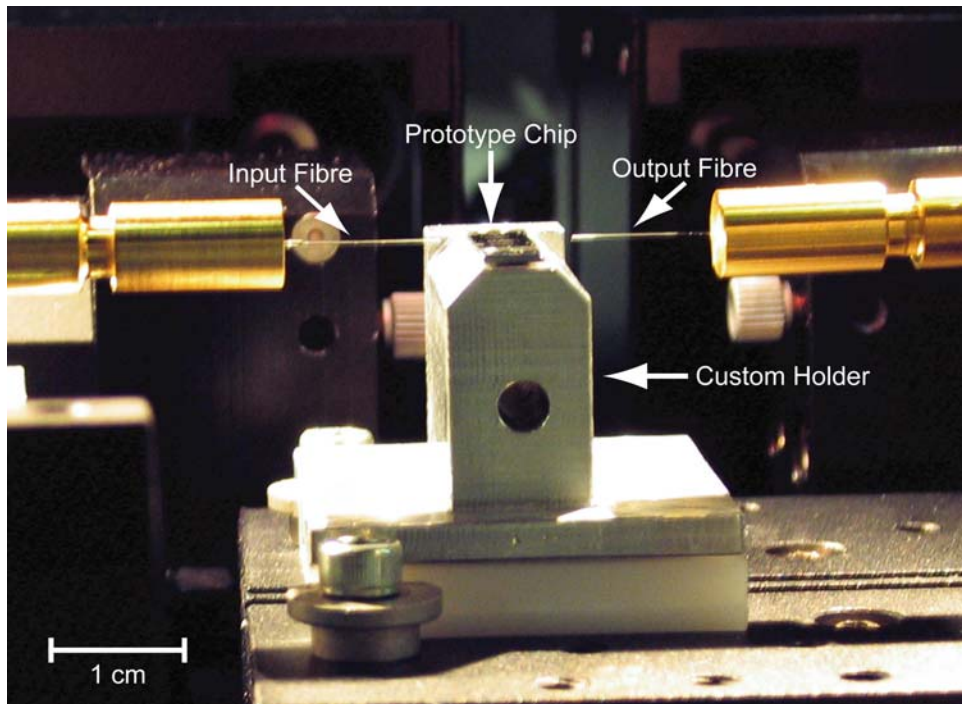


Fig. 6.6: Picture showing a switch prototype mounted on a custom holder. The thermo-electric cooler and thermistor are not in this picture because they would have hidden the chip.

6.3.1 Wavelength Response

The wavelength response of the prototypes was measured with a broadband source and an optical spectrum analyser. A free-space polarization module was inserted between the broadband source and the input PM fibre to ensure that only the desired polarization state coupled into the input waveguide. The measured spectra are shown in Fig. 6.7 and Fig. 6.8 for both the transmitted and reflected outputs. The response of only one input is included in Fig. 6.7 because the first prototype broke before it could be completely characterised. The expected wavelength response calculated with the Eigenmode expansion method from the filter design values is shown in Fig. 6.9 for comparison. Over-etching of the trenches forming the filter mirrors to between 25 nm and 86 nm occurred during fabrication, which shifted the filter response into the L-band. The reflection and transmission spectra are normalized to a 0 dBm input (excluding coupling losses). A device without a filter (i.e. with collimating mirrors alone) was fabricated on the same die as a prototype and its response is also shown in Fig. 6.7 and Fig. 6.8. Since the device without a filter also exhibited a high level of losses, it confirmed that the losses are due to the collimation system and channel waveguides. The most likely cause is a misalignment between the waveguides and mirror masks. Simulations indicated that a lateral misalignment of $\pm 1.1 \mu\text{m}$ induced at least 20 dB of losses. Moreover, the difference in wavelength response between the two inputs of the second prototype support this explanation since errors in alignment can lead to different incident angles for each input. A fraction of the loss (approximately 4 dB) is due to bending losses in the input waveguide. Although the horizontal refractive index contrast of the channel waveguides is high, light in the bend can leak into the substrate since the vertical contrast is weak.

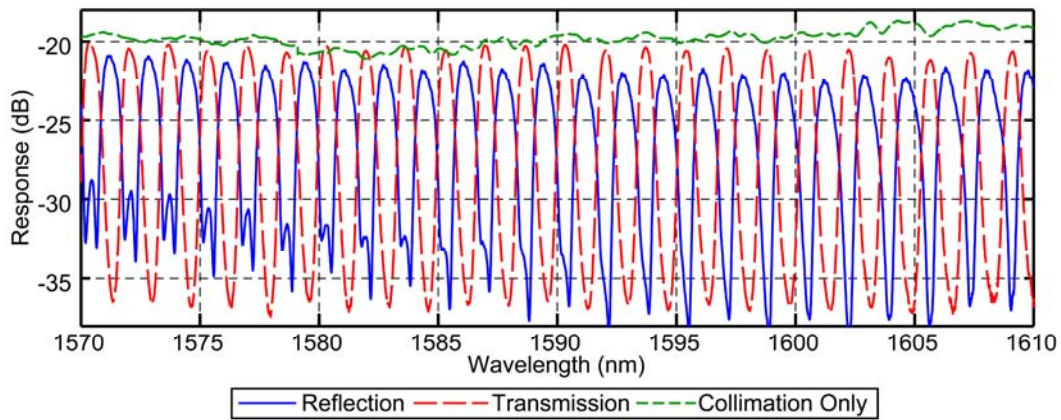


Fig. 6.7: Measured wavelength response of the first prototype. Only the response for input 1 is shown because the device broke before it could be completely characterised. The reflection spectrum is shown in blue, and the transmission spectrum in red. The green line shows the throughput of the collimation system without a filter.

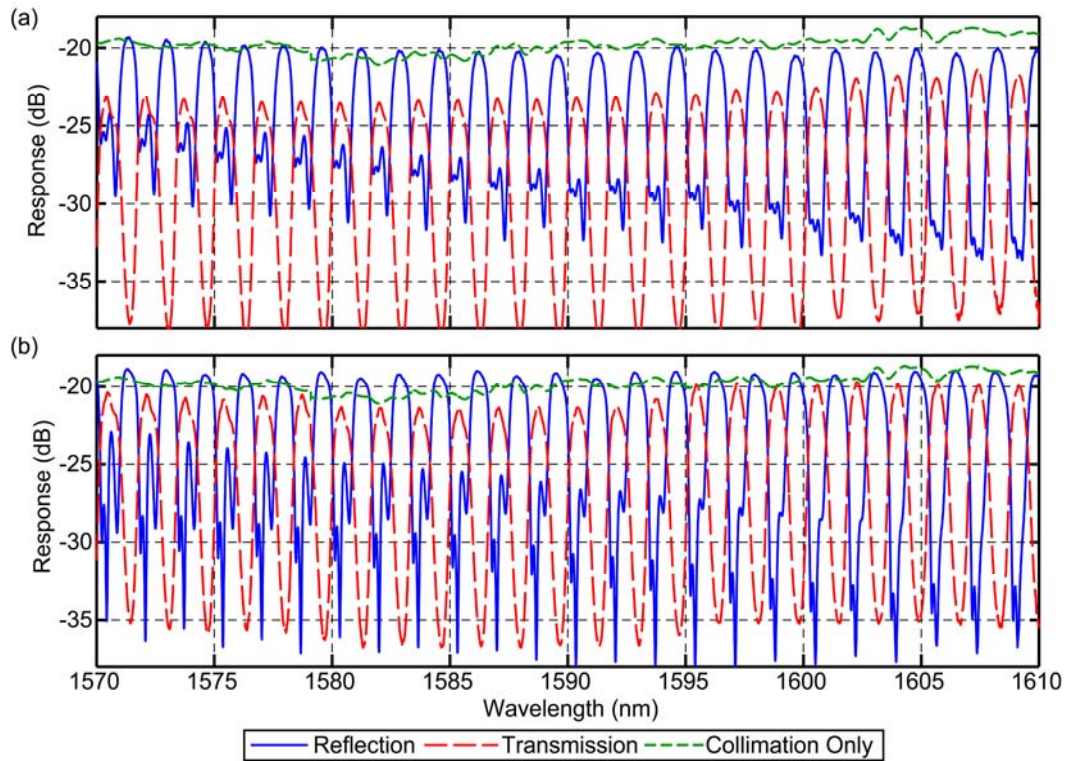


Fig. 6.8: Measured wavelength response of the second prototype: (a) shows the response of input 1 and (b) that of input 2. The reflection spectrum is shown in blue, and the transmission spectrum in red. The green line shows the throughput of the collimation system without a filter.

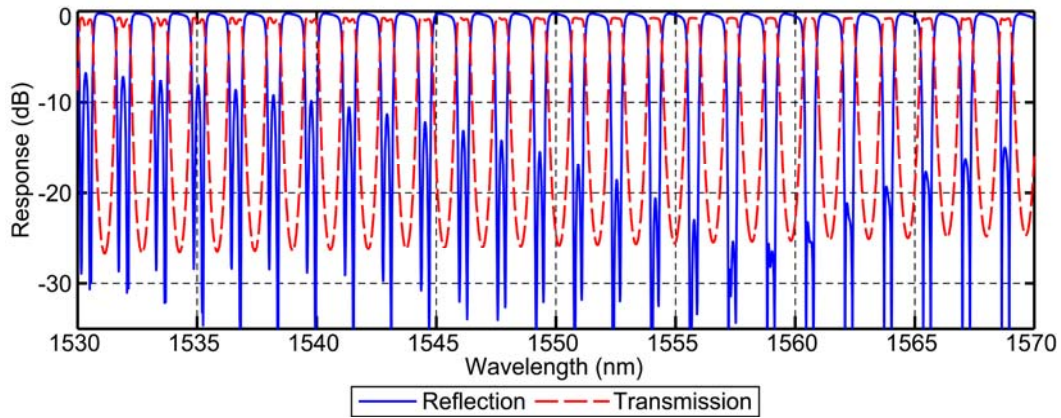


Fig. 6.9: Expected wavelength response for the switch prototype based on Eigenmode expansion simulations with the filter design values. The reflection spectrum is shown in blue and the transmission spectrum in red.

Fabrication errors reduced the free spectral range (FSR) below 200 GHz. The characteristics of the wavelength response of the fabricated filters are listed in Table 6.1, including their FSR and their transmission passband width. Nevertheless, it was possible to simultaneously fit 25 ITU channels in the reflection or transmission clear bandwidth of the filters. Since the filters can work with either the “odd” or “even” channels of the 100 GHz grid, they can handle any of the 50 channels in the L-band. The minimum clear bandwidth is 23.1 GHz while the average is close to 30 GHz for the three inputs. This is significantly less than the 55.5 GHz predicted by Eigenmode expansion simulations for the filter design values. This discrepancy is due to the reduction in cavity coupling caused by fabrication errors. The effects of the decrease in coupling can also be seen in the large ripples of the reflected signal at the wavelengths at which transmission is maximized in Fig. 6.8. Nonetheless, the minimum 3 dB bandwidth is 72.8 GHz, which is almost to seven times greater than the 10.6 GHz 3 dB bandwidth reported for a single micro-ring comb filter switch [3]. The first prototype has the sharpest response, since it has the widest clear passband but the narrowest 3 dB one.

Table 6.1: Characteristics of the frequency response of the fabricated filters

Device	Input	FSR (GHz)	Clear Passband (GHz)			3 dB Passband (GHz)		
			min	avg.	max	min	avg.	max
1	1	199.6	27.2	31.7	36.2	59.6	68.3	78.4
2	1	199.6	23.1	29.9	36.1	72.8	83.3	95.1
	2	199.3	24.7	29.2	35.1	73.4	83.5	94.8
Expected Values		200.0	49.9	55.5	62.7	64.6	70.4	75.5

The average channel insertion loss for the best 1x2 switch, which is obtained with input 2 of the second prototype, was 19.3 dB in reflection and 20.5 dB in transmission. The difference in loss between the reflected and transmitted signals, which originates in the higher radiation loss that transmitted signals experience because they interact with more trenches, was 1.2 dB on average. This is consistent with simulation results based on the dimensions of the fabricated filters which predicted a difference of 0.9 dB. Furthermore, as shown in Fig. 6.10, it was possible observe the difference in radiation losses with an infrared camera.

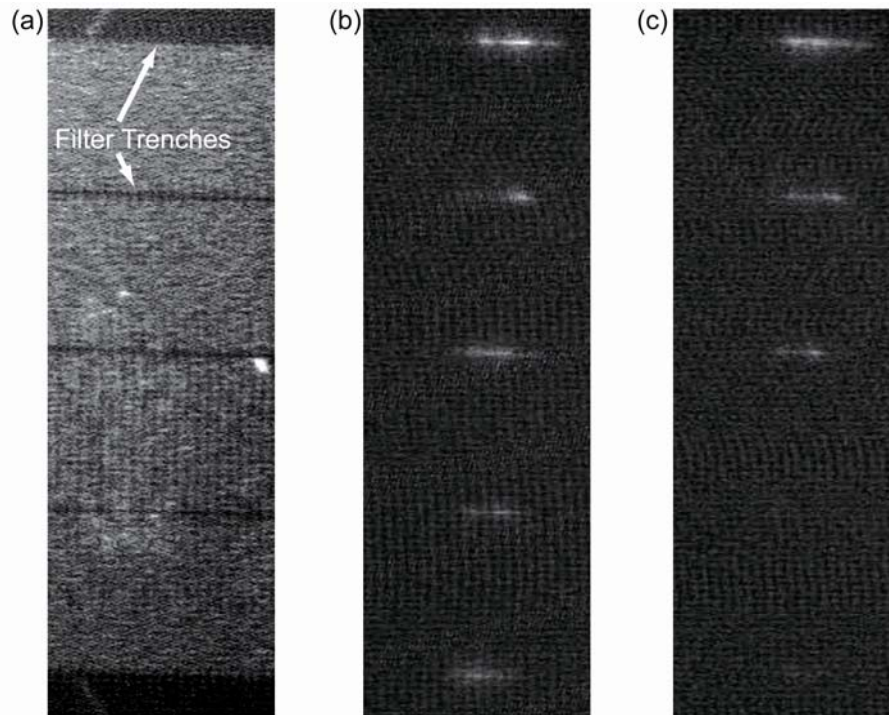


Fig. 6.10: Pictures of a filter taken (a) with visible light illumination and with infrared light (b) transmitted or (c) reflected by the filter.

The loss, crosstalk, and extinction ratio for the 50 channels in the L-band are shown in Fig. 6.11 for the first prototype and in Fig. 6.12 for the second. The expected performance calculated from simulations based on the filter design values are presented in Fig. 6.13, and the average values for all devices and simulations are reported in Table 6.2. The reason why insertion losses are higher in reflection rather in transmission for the first prototype is that the output waveguide facet of the reflected signal was damaged during the alignment of the tapered fibre. Unfortunately, the 20 dB extinction ratio that the filter was designed for was not obtained for any wavelength channel because of the decrease in coupling caused by fabrication errors. The difference between the performance of the odd and even channels comes from the asymmetry in the wavelength response which is also caused by the reduction in cavity coupling. Tolerance simulations on the trench width have shown that changes larger than ± 10 nm significantly degrade the filter response if they are not consistent across the filter. The large discrepancy between the expected reflected and transmitted signal average crosstalk and extinction ratio is caused by an increase in the strength of the reflected signal as the coupling between the Fabry-Perot cavities decreases. This occurs because when they are not perfectly coupled each cavity behaves as a single cavity Fabry-Perot filter with a slightly different peak transmission wavelength. Therefore, having multiple filters with unmatched transmission response in series creates the equivalent of a broadband mirror, which increases crosstalk for the transmitted signals and decreases extinction ratio for the reflected ones.

The filter response observed for the TM polarization over the L-band showed that most of the input light is reflected (it was designed to work only in TE). This can also be explained by decoupling of the filter cavities. Because of the effective refractive index discrepancy between the TE and TM polarizations, the filter cavities are coupled at different frequencies for the each polarization state. When the filter is working for one polarization, its cavities are decoupled

for the other, and thus most of the light having the unwanted polarization will appear at the reflected output because decoupled cavities behave as a broadband mirror.

Table 6.2: Average loss, crosstalk and extinction ratios of the prototypes. The values in parenthesis are the standard deviations.

Device	Input	Loss (dB)		Crosstalk (dB)		Extinction Ratio (dB)	
		Reflection	Transmission	Reflection	Transmission	Reflection	Transmission
1	1	22.0 (0.6)	20.5 (0.3)	12.6 (0.9)	13.8 (2.6)	12.4 (2.3)	14.1 (1.2)
2	1	20.2 (0.2)	23.0 (0.6)	17.1 (0.8)	6.1 (2.8)	8.9 (2.3)	14.4 (1.2)
	2	19.3 (0.2)	20.5 (0.5)	15.1 (1.5)	12.9 (1.7)	14.1 (1.7)	13.9 (1.7)
Expected Values		0.4 (0.0)	1.0 (0.3)	25.4 (0.7)	14.6 (6.6)	15.3 (6.3)	24.7 (0.5)

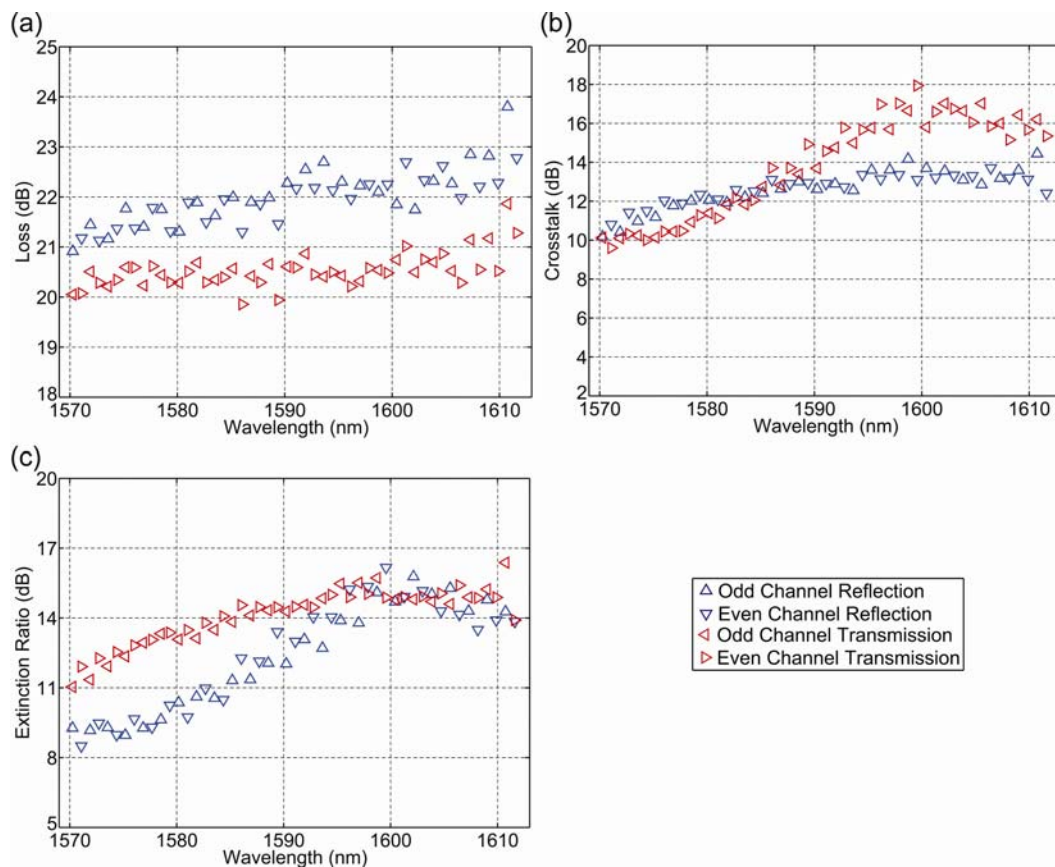


Fig. 6.11: First prototype wavelength channel performance over the L-band: (a) insertion loss, (b) crosstalk, and (c) extinction ratio.

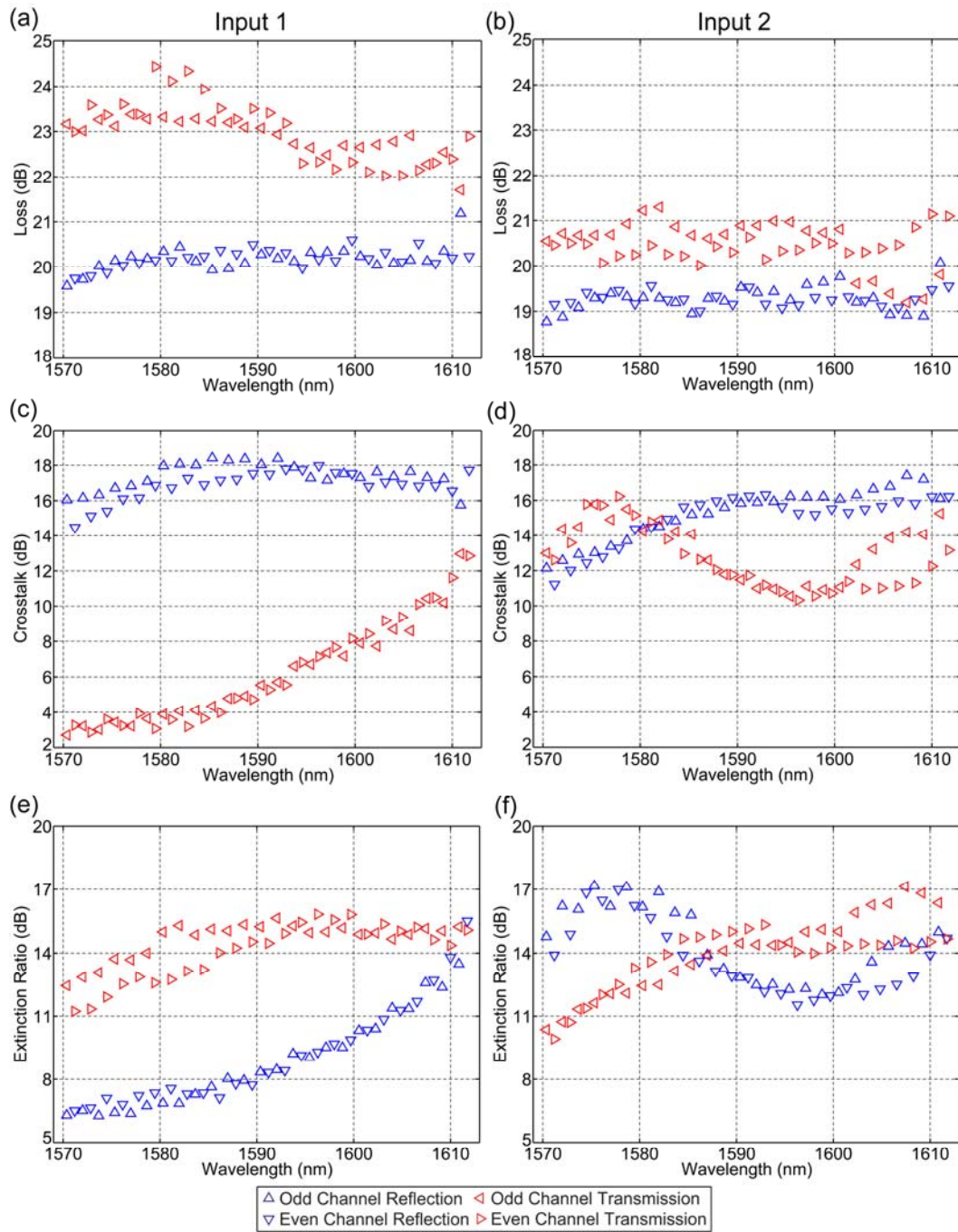


Fig. 6.12: Second prototype performance over the L-band: (a) and (b) show the channel insertion loss for input 1 and 2, respectively; (c) and (d) the crosstalk; and (e) and (f) the extinction ratio.

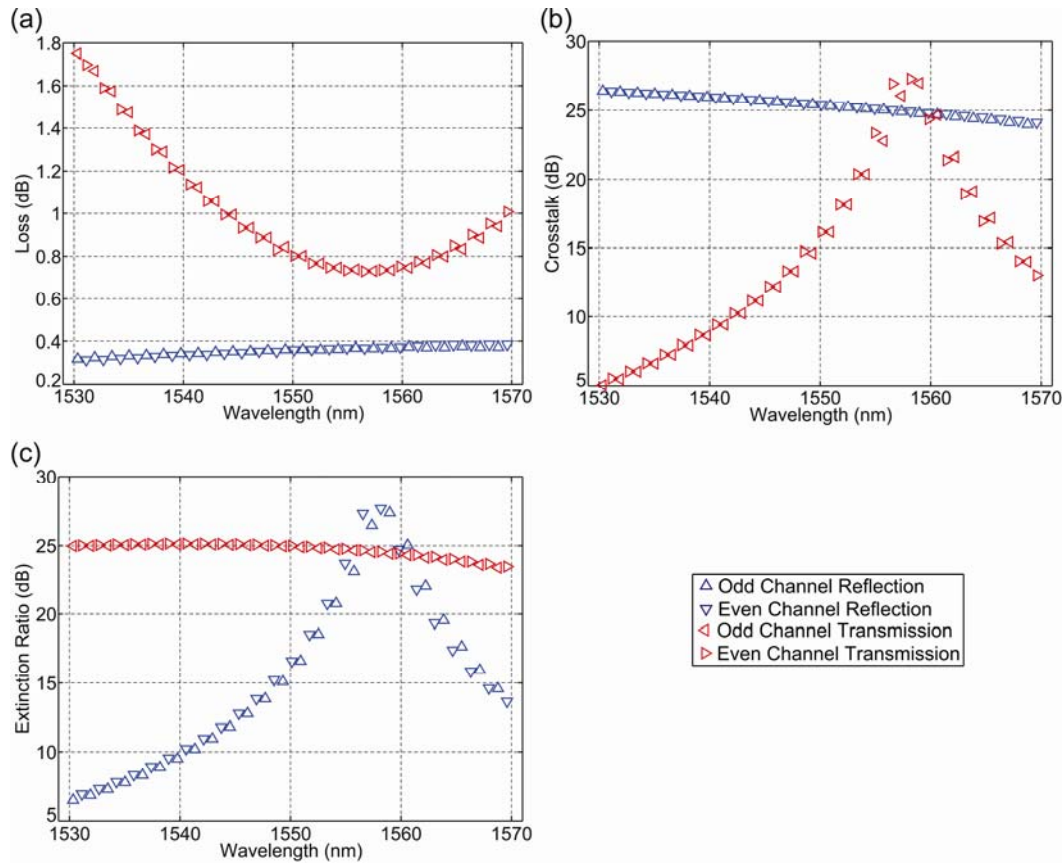


Fig. 6.13: Expected wavelength channel performance over the C-band calculated from simulations based on the filter design dimensions: (a) insertion loss, (b) crosstalk, and (c) extinction ratio.

6.3.2 Transmission Experiments

To verify whether the filters caused significant signal distortion, the bit error rate (BER) of a 10 Gb/s non-return to zero signal was measured as a function of received power. A schematic of the test setup is shown in Fig. 6.14. A tuneable laser was adjusted to 1595.49 nm (187.9 THz) and externally modulated with a $2^{31}-1$ pseudorandom bit sequence. This wavelength was used because it was the operating point at which the filter performance was optimum within the range covered by the optical sources and amplifiers that were available during this experiment. An L-band fibre amplifier boosted the signal before it was coupled to input 2 of the second prototype. This particular device and input was used because it is the one having the best filter characteristics. The output light was amplified with a semiconductor optical amplifier (SOA) and then sent through a

tuneable filter with a 0.55 nm 3 dB passband to remove amplification noise. The optical signal passed through a variable attenuator connected to a photodiode. The photodiode electrical signal was boosted with broadband amplifiers before being sent to a BER tester.

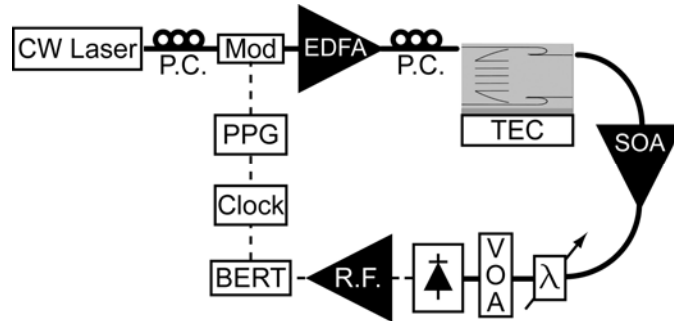


Fig. 6.14: BER measurement test setup. (Mod: 10 Gb/s LiNbO₃ modulator, EDFA: erbium-doped fibre amplifier, P.C.: polarization controller, TEC: thermo-electric cooler, SOA: semiconductor optical amplifier, R.F.: radio frequency amplifiers, BERT: bit error rate tester, PPG: pulse pattern generator)

The measured BER curves are shown in Fig. 6.15. For the measurement without the switch, the signal was sent through an alignment waveguide adjacent to the filter on the integrated circuit. The power penalty when the filter is in reflection is less than 0.5 dB. However, in transmission it was impossible to obtain a BER better than 10^{-7} . This is because the extra attenuation suffered in transmission brought the power at the switch output below -20 dBm, which was the SOA sensitivity floor, and thus greatly reduced the signal to noise ratio at the photodiode. The impact of this can be seen on the eye diagrams shown in Fig. 6.16. For the same level of received power, the eye of the transmitted signal has an opening of 60 mV while that of the reflected one is 70 mV. The difference in peak power at the output of the device and after the SOA is shown in Fig. 6.17 for both the reflected and transmitted signals. The 6.8 dB difference between the reflected and transmitted signal at the device output is much larger than the one obtained from the wavelength measurement response (i.e. 1.2 dB) and this was probably due to damage to the transmitted signal output waveguide that could have occurred during the alignment of the output fibre. Because the switch

operated in the L-band, no other optical amplifiers were available to further compensate the loss or boost the input signal. Since most of the attenuation is due to the collimation system and not the filter, the limitations encountered during this experiment are probably the results of restrictions in our fabrication process and are not intrinsic to the device.

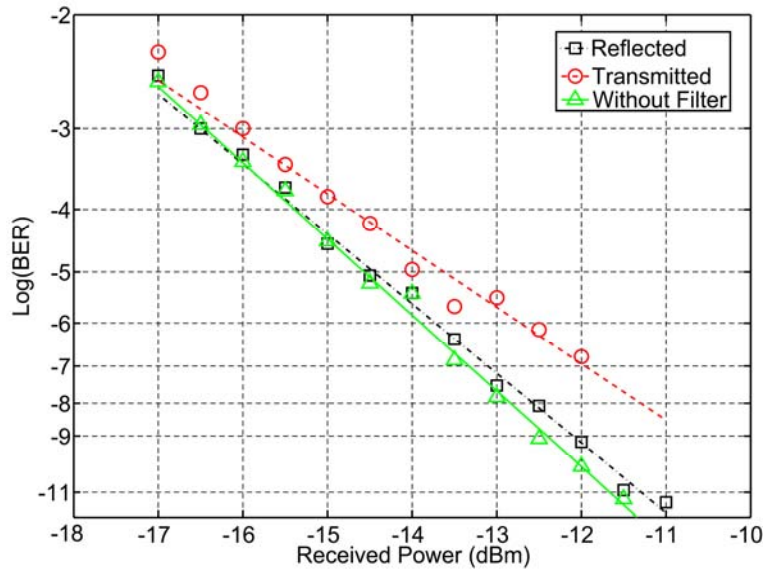


Fig. 6.15: Bit error rate curves for a 10 Gb/s signal reflected and transmitted by the switch prototype. The switch impact on the signal can be seen by comparing the BER for a signal send through an alignment waveguide.

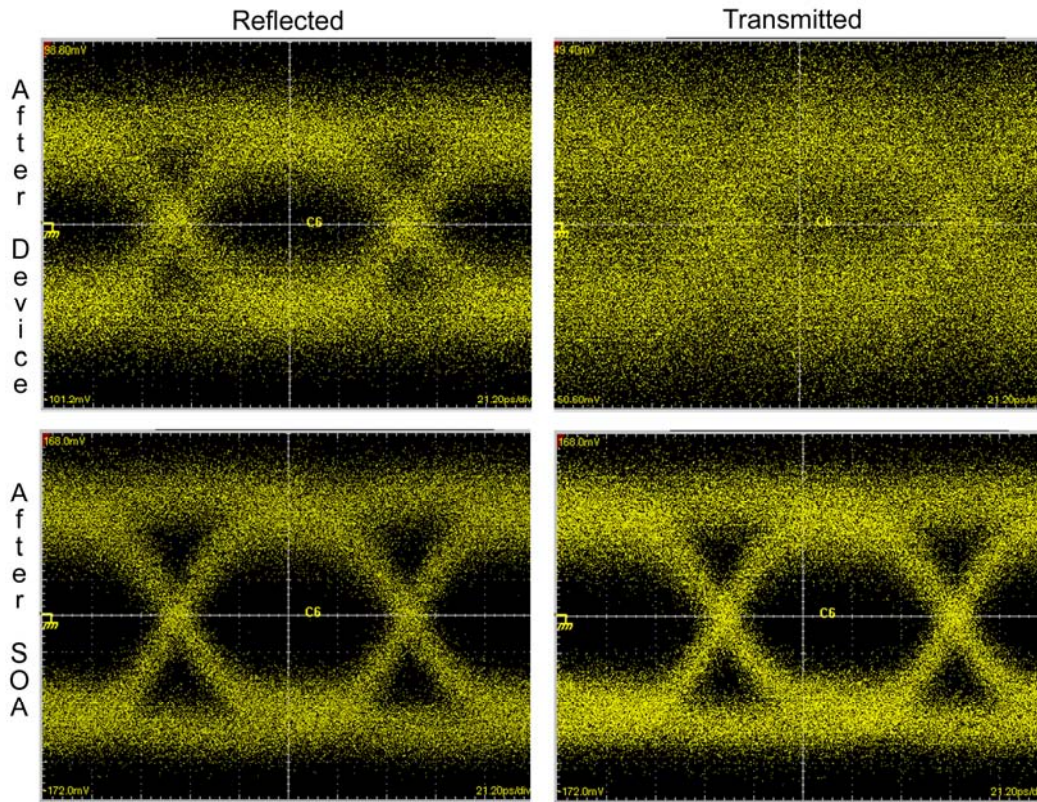


Fig. 6.16: Eye diagrams measured at the output of the device before amplification and at -12 dBm of received power for the transmitted and reflected signals.

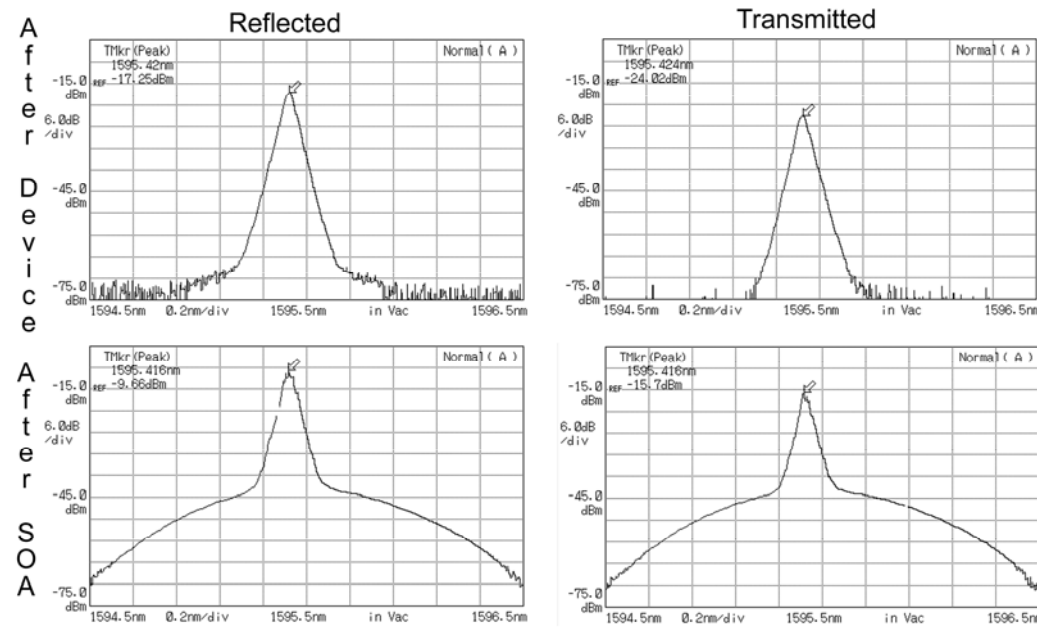


Fig. 6.17: Measured optical spectra after the optical switch and the SOA showing the difference in peak power of the reflected and transmitted signals.

6.4 Conclusion

The layout and characterisation of 2x2 optical switch prototypes based on the designs described in chapter 4 and 5 was presented. Because of the large beam waist needed to ensure that beams propagate undistorted and that the plane wave response of the filter is preserved, TIR parabolic mirrors were used to collimate the outputs of channel waveguides before they were sent to the filter. Two etch steps were required to build the switch because the input and outputs channel waveguides could not be made narrow enough to be single mode at the etch depth necessary to implement the filter and parabolic mirrors. This introduced a critical alignment step which caused high insertion losses. A self-aligned double etch process could be used to reduce losses due to alignment errors.

Characterisation of the prototypes showed that over-etching shifted the filter wavelength response towards the L-band. It also reduced coupling between the filter cavities, which decreased the clear bandwidth by approximately 40 % for the two devices tested and the maximum achievable extinction ratio by about 9 dB. It also caused ripples in the reflected signal. This demonstrates the sensitivity of the filter performance to coupling between the cavities. To obtain the designed filter response, the control on the trench width must be within 10 nm. This is clearly the most critical aspect in the fabrication of integrated Fabry-Perot optical space switches. Nevertheless, it was possible to contain 50 wavelength channels of the 100 GHz ITU grid within the response of the prototypes. Although the thermo-optic effect was used to characterise the prototypes, the filters could be tuned with faster mechanisms, such as electro-optic and/or plasma effects, after optimization of the waveguide doping profile. Data transmission tests at 10 Gb/s showed that error free transmission is achievable with little power penalty when the signal is reflected from the prototype device but the combination of radiation and collimation losses limited the BER to 10^{-7} in transmission. However, this limitation is caused by fabrication errors and it is probably not intrinsic to the device.

Gains in efficiency could be obtained by using first order mirrors to implement the filters. This would practically eliminate radiation losses and improve cavity coupling, which would extend the switch bandwidth over the entire C-band. Moreover, with the ability to build smaller features, the channel waveguides could be fabricated at the same time as the filter and collimating mirrors, which would reduce losses due to misalignment. Nevertheless, efficient first order designs require aspect ratios between 20:1 and 40:1, which pose a significant fabrication challenge.

References

- [1] B. E. A. Saleh and M. C. Teich, *Fundamentals of photonics*, 2nd ed. Hoboken, NJ: Wiley-Interscience, 2007.
- [2] I. J. Hodgkinson and Q. h. Wu, *Birefringent thin films and polarizing elements*. River Edge, N.J.: World Scientific, 1997.
- [3] B. G. Lee, A. Biberman, P. Dong, M. Lipson, and K. Bergman, "All-optical comb switch for multiwavelength message routing in silicon photonic networks," *IEEE Photon. Tech. Lett.*, vol. 20, no.10, pp. 767-769, May-Jun 2008.

Scalability Analysis

7.1 Introduction

In addition to fast switching speeds and good optical performance, a practical optical switching technology should also be scalable. Integrated Fabry-Perot space switches present interesting possibilities in that regard since their planar waveguide configuration allows the interconnection of switching elements (i.e. filters) without having to use channel waveguides. Therefore, it is possible to have light signals crossing each other without suffering losses, which is not the case in devices implemented with channel waveguides.

The two switch fabrics configurations used to evaluate the scalability of integrated Fabry-Perot optical space switches are described in section 7.2. The technique used to minimize the switch fabrics areas is presented next, along with the optimisation results for devices with 2 to 16 ports. Lastly, the trade-offs in the design of integrated Fabry-Perot switch fabrics are discussed.

7.2 Possible Switch Fabric Layouts

Integrated Fabry-Perot optical space switches provide a flexible building block to build various switch fabrics. They can be used to implement crossbar, shuffle Beneš or router-selector architectures. In crossbar configurations, they are suitable for use as wavelength selective switches within reconfigurable optical add/drop multiplexers (see Fig. 7.1). The shuffle Beneš configuration is adapted from work by Ma and Kuo, who developed this architecture for 2-D MEMS

mirrors [1]. The static mirrors required in the shuffle Beneš configuration can be implemented by Bragg gratings when integrated Fabry-Perot switches are used in place of MEMS, as shown in Fig. 7.1(b). It is also possible to create a colorless device with integrated Fabry-Perot switches by using interleavers to separate the incoming signals into groups of “odd” and “even” channels and then processing each group with different switches. These interleavers can be implemented with the same filter design as the switches. After being processed by the switches, the outputs are recombined with another set of interleavers. This concept is illustrated in Fig. 7.1(c).

7.3 Optimisation Technique and Results

The optimization software described in chapter 6 was extended to handle multiple ports. It was used to find the layouts requiring the least surface area for both crossbar and shuffle Beneš configurations by searching for the optimum input beam waist and filter angle. To speed up the program, only the longest propagation path was considered for the crossbar layouts. This technique could not be applied to shuffle Beneš switches because in this architecture all optical paths are of equal lengths. Nonetheless, this does not mean that all paths have the same impact on input beams since filter distortion changes whether the beams are transmitted or reflected. Although waist magnification, focal shift, and angular shift are negligible for a single filter, their cumulative effects must be considered when designing large switch fabrics, especially for transmitted beams which suffer more from these impairments. They also have larger lateral beam shift. Therefore, during the shuffle Beneš optimization, the path requiring the most filters in transmission mode was used. The optimization results are reported in Table 7.1 for both configurations. Note that the collimation systems and the input and output waveguides were not considered in these calculations. All device parameters, including the filter and planar waveguide configurations, were the same as those described for the prototypes presented in chapter 6.

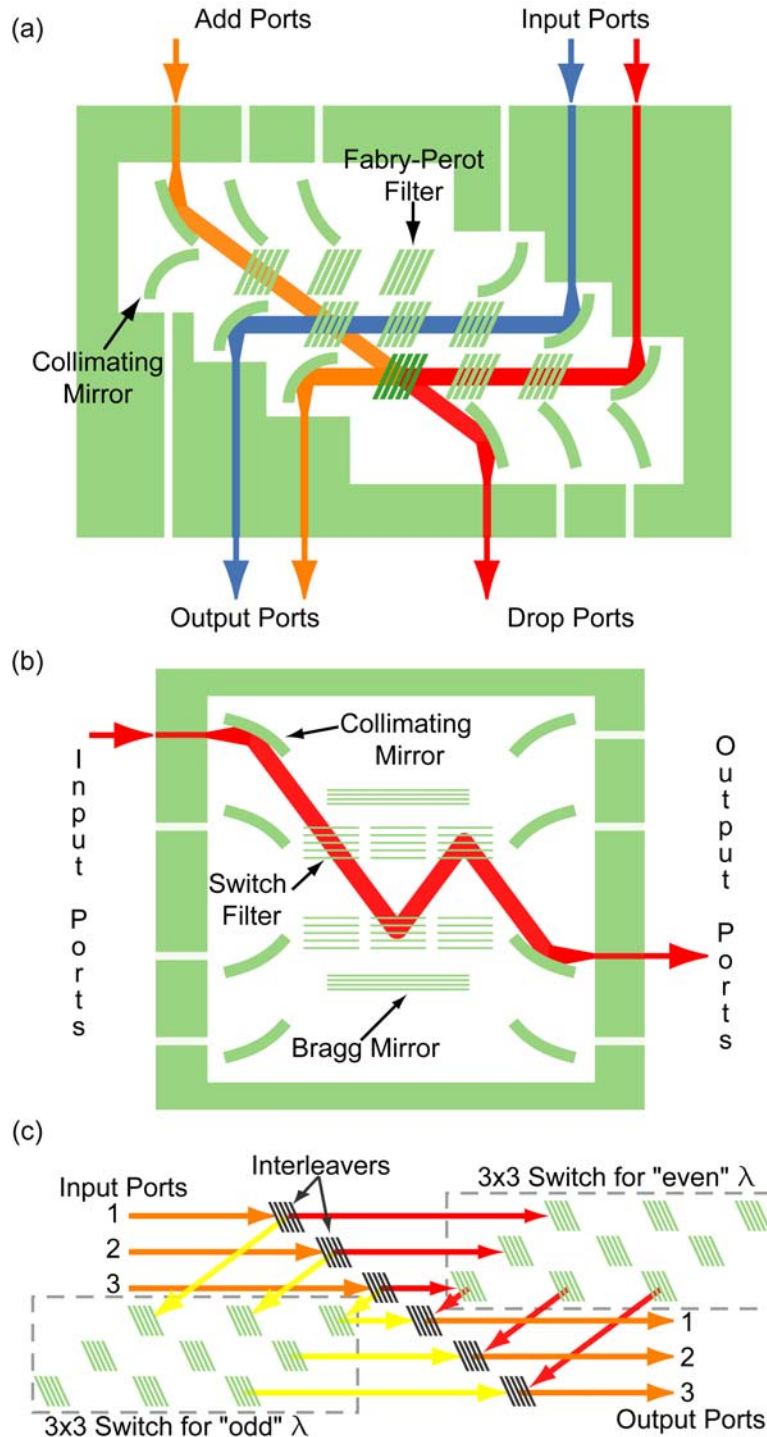


Fig. 7.1: Schematics of integrated Fabry-Perot switch fabrics: (a) crossbar layout configured as a 3x3 wavelength selective switch within a ROADM; (b) 4x4 shuffle Beneš switch; and (c) 3x3 colorless switch fabric made of two 3x3 crossbar switches and 6 interleavers. In the ROADM wavelength selective switch, the added signal can be at a different wavelength than the dropped one but both must be from the same group (i.e. "odd or" "even").

Table 7.1: Switch fabrics with minimum area

Number of Ports	Crossbar				Shuffle Beneš			
	Filter angle (°)	Width (mm)	Length (mm)	Area (mm ²)	Filter angle (°)	Width (mm)	Length (mm)	Area (mm ²)
2	1.6	0.9	7.0	6.2	1.2	0.3	0.9	0.2
4	2.4	2.6	22.1	57.3	2.4	2.7	27.6	74.6
8	5.0	10.1	52.2	527.0	3.8	9.1	81.2	737.1
16	10.8	40.5	111.1	4 494.5	6.2	30.8	193.8	5 965.3

7.4 Design Trade-offs

In the layout of integrated Fabry-Perot switch fabrics, selecting the filter angle is a trade-off between the ability of the filter to separate the input and reflected beams, and the minimum beam waist that is needed to preserve the filter wavelength response. Having a large incident angle reduces the distance required to separate the incident and reflected beams and thus enables the filters constituting a switch fabric to be positioned closer to each other. However, as explained in chapter 5, the beam waist required to maintain the filter wavelength response increases rapidly with the angle of incidence. As a result, the distance needed between filters can increase as the incident angle gets larger because the input beams become bigger. This is a significant difference with 2-D MEMS switches in which the input beam size is determined by diffraction inside the device, which is only a function of the propagation distance. Therefore, the optimization routine goal is to find the incident angle that provides the best compromise between the ability of the filter to separate signals and the width of the input beams. As can be seen on Table 7.1, the optimum incident angles are small for all the listed configurations but they slowly increase with the number of ports. This shows that the dominating factor in the switch fabric layout is the input beam waist required by the filters. As the number of ports increases, the distance between the filters begins to have a more significant impact on the switch fabric area, and as a consequence, it drives the incident angle to larger values. Also, the small incident angles in the optimized layout lead to thin and long devices, which can limit the

number of dies per wafers. Therefore, the configuration that minimizes area is not necessarily the one that maximizes yield.

Since angular and frequency passband bandwidths are proportional, filters with large frequency bandwidth are able to work with small input beams. Therefore, smaller switch fabrics can be achieved with filters having a wide passband. Fig. 7.2 shows the minimum area as a function of clear bandwidth for a 4x4 crossbar switch. However, the maximum passband width is limited by the refractive index modulation achievable with a given tuning mechanism and the frequency grid on which the switch must operate since it must be possible to tune the filter response by at least the separation between two adjacent channels. On the other hand, the refractive index contrast used to implement the filters has no significant impact on a switch fabric area. This is illustrated in Fig. 7.3 which shows the minimum area as a function of the refractive index contrast used to implement the filter in 4x4 crossbar and shuffle Beneš switch fabrics.

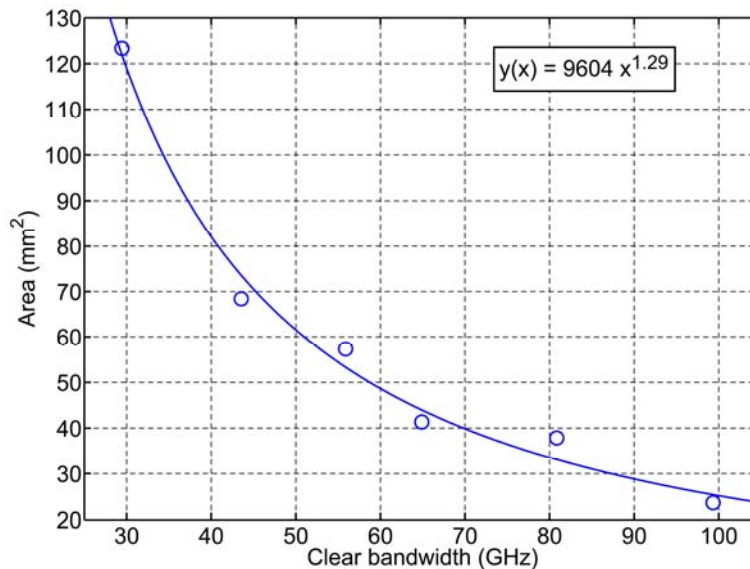


Fig. 7.2: Area as a function of filter clear bandwidth for a 4x4 crossbar switch fabric.

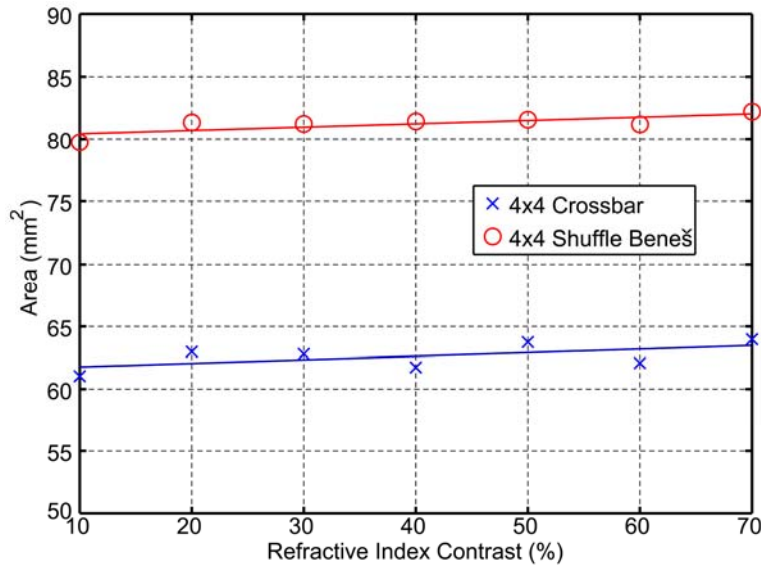


Fig. 7.3: Minimum switch area for 4x4 crossbar and shuffle Beneš fabrics vs. the refractive index used to implement the filters.

Due to the constraint imposed by the filters on the input beams, shuffle Beneš layouts require more area than their crossbar equivalent, except for 2x2 switches (only one filter is needed in 2x2 Beneš switches). This is not the case with MEMS switches for which crossbar fabrics are significantly larger than shuffle Beneš ones [1]. Moreover, shuffle Beneš switch fabrics are rearrangeably non-blocking whereas crossbar fabrics are strictly non-blocking. Nevertheless, the fewer number of filters in shuffle Beneš fabrics can drastically improve performance. In the worst case scenario, a signal has to propagate through 15 filters in an 8x8 crossbar switch: 14 working in transmission and one in reflection. Assuming the propagation losses computed with Eigenmode expansion for a filter with 5 μm deep second order mirrors (see chapter 5), this leads to an insertion loss of 11.6 dB. In an 8x8 shuffle Beneš switch, the signal goes through at most 5 filters and is reflected by 3 static mirrors. If the static mirrors have the same losses as filters in reflection, this gives a 5.2 dB loss.

7.5 Conclusion

Integrated Fabry-Perot switches can be used to build different kind of fabrics. Crossbar and shuffle Beneš configurations were optimized in order to evaluate their scalability. It is the minimum beam waist needed to maintain the filter response that is the dominating factor limiting a switch fabric minimum area. Furthermore, 8x8 fabrics (in crossbar configuration) could be fabricated on standard 3" wafers commonly used with III-V semiconductors. Although shuffle Beneš switch fabrics are larger than crossbar ones, their smaller number of filters makes them more efficient.

Reference

- [1] X. H. Ma and G. S. Kuo, "A novel integrated multistage optical MEMS-mirror switch architecture design with shuffle Benes inter-stage connecting principle," *Opt. Commun.*, vol. 242, no. 1-3, pp. 179-189, Nov. 2004.

Chapter 8

Conclusion

8.1 Summary

The increase in throughput of optical telecommunication networks, stimulated by the growing popularity of the Internet, was achieved by improvements in transmission bit rates and by the multiplication of wavelength channels. However, these enhancements to the transmission capacity put pressure on the electronic routing components of the network nodes. As a result, electronic routers have become expensive and power hungry machines that might soon be bottlenecks in optical networks. This issue, in conjunction with the advent of technologies enabling optical transmission over long distances, has motivated research towards the development of all-photonic networks in which data signals always remain in the optical domain between their ingress and egress points.

Doing so reduces the amount of electronic processing required for routing. Furthermore, all-photonic networks based on burst or packet switching are flexible and allow efficient use of the transmission capacity. Such networks require at their core fast, broadband, transparent, and scalable optical space switches. However, none of the currently available commercial technologies, such as MEMS or thermo-optic switches, can achieve speeds fast enough for burst or packet switching. Many other technologies that have been demonstrated in laboratory experiments, including electro-optic devices or semiconductor amplifier based switches, possess much faster switching times but they have low

optical performance or issues of scalability. This motivated the development of a novel switching concept based on tuneable off-axis Fabry-Perot filters implemented in planar waveguides, which is the subject of the investigation reported in this thesis.

The objectives of this work were to assess the practicality and scalability of this novel concept as an optical space switching technology for the next generation of optical networks. This was achieved through the development of a design methodology that resulted in the fabrication of optical prototypes. The design process began by identifying a suitable material platform. GaAs/AlGaAs planar waveguides were chosen over LiNbO₃ and EO polymers because they are readily available and they can provide the high refractive index contrast that is necessary to obtain broadband filter mirrors.

A comprehensive optimization of the waveguide structure, which for the first time simultaneously considered the layer structure of the waveguide, its refractive index contrast, and the etch depth, was conducted to minimize radiation losses in trenches created in a planar waveguide. The results of this study determined the effective refractive index of the planar waveguide, which modeled the waveguide in the transfer matrix method used for the filter design. A comb filter response was implemented to enable the switches to work with any channel in an entire wavelength band while requiring only a small refractive index modulation. Multiple FP cavities were coupled to create a flat and wide passband with sharp transition between regions of high transmission and high reflection. The mirror structure used in the filter was investigated to find out which configuration maximized bandwidth and minimized radiation losses. The filter design was adjusted to satisfy the fabrication limits imposed by the tools available in McGill's microfabrication laboratory and a study was performed to determine the minimum Gaussian beam size required to preserve the characteristics of the plane wave response of the filter.

After developing a layout that facilitated fabrication and testing, optical prototypes were implemented and characterised. Over-etching of the mirror trenches shifted the device wavelength response in the L-band and reduced cavity coupling. This affected the switches performances but nevertheless it was possible to measure the insertion loss, crosstalk, and extinction ratio for 50 wavelength channels. Switching between transmission and reflection was achieved with the thermo-optic effect since the waveguide doping was not designed to provide electro-optic effects. Bit error tests at 10 Gb/s showed that the filter impose a very small power penalty in reflection. However, in transmission the bit error rate was limited to 10^{-7} , probably because the excess loss suffered in transmission brought the switch output power below the sensitivity floor of the optical amplifier located before the photodiode.

Lastly, the scalability of integrated Fabry-Perot space switches was investigated through the optimization of crossbar and shuffle Beneš fabrics with 2 to 16 ports. The dominating factor limiting the minimization of a switch fabric area is the minimum beam waist needed to avoid distortion. Although crossbar fabrics are more compact than shuffle Beneš ones, the smaller number of filters required to implement shuffle Beneš fabrics can significantly improve the optical performance of devices with a given port count.

8.2 Comparison with Existing Technologies

The great strength of the design approach developed in this thesis is its flexibility. By relying on the transfer matrix method to design the switch frequency response, almost any passband shape can be achieved, as demonstrated with thin-film filters. Implementing the filters in planar waveguides provided a level of integrations never achieved in previous off-axis Fabry-Perot switches. It allows miniaturisation of the components and can reduce cost considerably. However, integration creates new challenges. Careful design of the planar waveguide is required to minimize radiation losses. It is also necessary to verify that the light

beams inside the devices are not distorted by the filters, especially when they are used at oblique incidence.

In terms of optical performance and scalability, no technologies come close to the results demonstrated with MEMS switches but they are too slow for burst or packet switching. Silicon-on-insulator (SOI) thermo-optic switches might be able to achieve speeds sufficient for burst switching but an efficient and practical fibre coupling technique needs to be developed. In theory, integrated Fabry-Perot switches could achieve performance comparable with other electro-optic devices. Mach-Zehnder interferometers (MZI) have less stringent fabrication requirements, and if they are implemented with high index contrast waveguides, they could be more compact than integrated Fabry-Perot switches. Directional couplers (DC) on the other hand have similar fabrication tolerances than integrated Fabry-Perot switches but these tolerances are easier to meet since deep etching is not required. Digital optical switches (DOS) can easily be made polarization independent because of their digital response but their minimum length is limited by the small angle needed to achieve low crosstalk. The characteristic that makes integrated Fabry-Perot switches stand out from the other electro-optic switch designs is their ability to work with different wavelength bands. MZI and DC can only handle a single wavelength at the time. Moreover, their control signals need to be calibrated for every new wavelength that they have to work with. DOS are able to switch multiple wavelengths simultaneously but they cannot separate them in different bands. Furthermore, integrated Fabry-Perot switches can have a flat and wide passband which makes them transparent to a variety of bit rates.

Devices similar to integrated Fabry-Perot switches have been demonstrated with micro-ring resonators but, as in the case of SOI thermo-optic switches, coupling with optical fibres is an issue for telecommunication applications. However, micro-ring switches have shown a lot of potential for on chip interconnects.

The possibility of obtaining gain and the very low crosstalk levels provided by semiconductor optical amplifier switches represent advantageous characteristics to implement a switch fabric. However, their power consumption is higher than electro-optic devices and they introduce nonlinearities and noise. Their scalability appears to be limited to similar port count as integrated Fabry-Perot switches.

Among the fast switching technologies reviewed in chapter 2, the largest switch fabric reported is a 64x64 phase array that combined multiple chips. The biggest single chip fabrics reported are 16x16 arrays, which is larger than the largest integrated Fabry-Perot switch fabrics that could be implemented on a 3” wafer (i.e. 8x8 crossbar).

Unfortunately, it is impossible to say that integrated Fabry-Perot optical space switches represent a clearly advantageous technology to implement switch fabrics for burst and packet switched networks. Nevertheless, with the improvements suggested in the next section and if a network architecture was developed to take advantage of their unique ability to work with different wavelength bands, integrated Fabry-Perot switches could represent an enabling technology for the next generation of optical networks.

8.3 Future Work

The work presented in this thesis laid the foundations for the development of integrated Fabry-Perot optical space switches but the prototypes demonstrated here could be improved in a number of ways. The first would be to reduce the insertion loss of the collimation system. Alignment between the photomasks defining the channel waveguides and the collimating mirrors could be improved with a self-aligned double etch process or better yet, the channel waveguides could be defined at the same time as the collimating mirrors. This would require a lithographic process with a minimum feature size much smaller than 1 μm , such as electron beam lithography or deep UV photolithography. Moreover, the

bending losses in channel waveguides with a strong horizontal confinement but with a weak vertical one should be investigated further. Experimental measurements of a series of bends with different radius showed that losses increase more rapidly than the theoretical predictions obtained with two-dimensional analytical methods. The most likely cause for this discrepancy is that significant substrate leakage probably occurs in the bends.

The ability to define smaller features would allow the implementation of first order filter mirrors, which would greatly improve the switch performance. It would reduce radiation losses in the filter trenches and increase cavity coupling. However, doing so would also require improvements in the etch process because of the high aspect ratios needed. Thus, inductive coupled plasma or chemically assisted ion beam etching would have to be used. Another way to reduce radiation losses in the deep etched features would be to use two dimensional photonic crystals to form the filter mirrors. In this case, the resonances taking place in the mirrors would occur mostly in the planar waveguide region between the holes defining the photonic crystal and thus the signal would suffer less radiation losses. A theoretical investigation of coupled cavity FP filters with photonic crystal mirrors has been reported in [1, 2].

The demonstration of the fast operation of integrated FP switches with electro-optic effects also needs to be done. This requires investigation of the doping profile of the planar waveguide to optimize the refractive index modulation as a function of applied voltage. There is also a trade-off to be reached between the achievable refractive index modulation and the extra insertion loss caused by the added doping. If the GaAs substrate is to be used as an electrode, then the waveguide should have a P-I-N doping profile (see Fig. 8.1(a)). A process to deposit ohmic contacts on GaAs would have to be developed since none is available in the microfabrication laboratory. It is possible to avoid doping the waveguide but that requires the deposition of Schottky metal contacts on both sides of the epitaxial layers, and thus they have to be transferred

onto a support substrate [3], as shown in Fig. 8.1(b). The waveguide layers can be removed from the substrate on which they were grown by adding a layer of AlAs under the waveguide and using the high etching selectivity between GaAs and AlAs of $\text{H}_2\text{O}:\text{NH}_4\text{OH}$ [4]. However, it would be a very delicate operation.

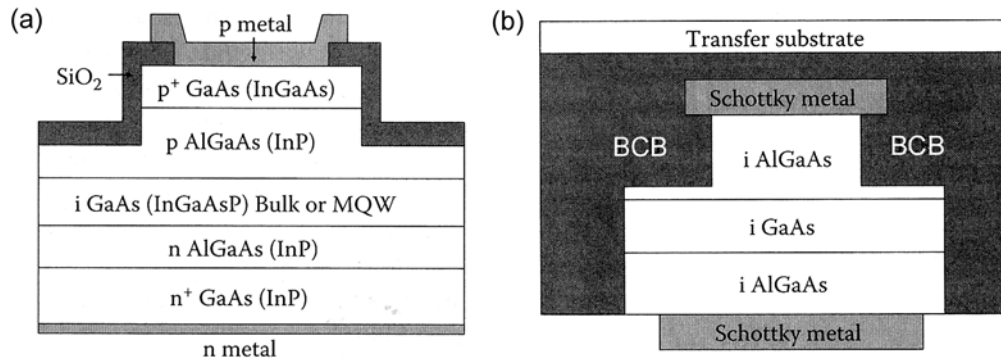


Fig. 8.1: Possible GaAs epitaxial configurations to obtain electro-optic effects: (a) P-I-N doping profile and (b) layers with intrinsic doping transferred onto a support substrate. (BCB: benzocyclobutane; MQW: multiple quantum wells). Figure adapted from [3].

Unlike the thermo-optic technique used in this thesis to test the prototypes, which required that the whole chip be heated, employing electro-optic effects provides a confined tuning mechanism. Thus, slightly different voltages could be applied to each filter cavity to compensate for fabrication errors. This would multiply by four the number of control signals required but in a more advanced implementation, a voltage divider could be fabricated on chip and then the resistances in the divider could be adjusted with laser trimming during the testing of the devices.

Electro-optic switches are electro-static devices that only consume significant amount of power when they are changing state. Nonetheless, because of the high switching rates required in optical networks, it is important to minimize their power consumption. Having individual control on the filter cavities could reduce the power consumption of integrated Fabry-Perot switches because switching could be achieved by decoupling only one or two cavities to change the filter response from transmission to reflection. As explained in chapter 6, decoupling the cavities turns the filter into a broadband mirror.

Lastly, a major drawback of the optical prototypes presented in this thesis is their polarization dependence. The filter could be made polarization independent by adjusting their cavity size such that different orders are simultaneously satisfied for the different polarizations. However, this would also determine the filter free-spectral range, and it might not correspond to a useful frequency grid. Subwavelength structures could be added to the planar waveguide to compensate for the effective refractive index difference between the polarizations. However, the switches would have to be actuated with a mechanism other than electro-optic effects since they are polarization dependent. One possible solution would be to use current injection but that would increase power consumption.

Before optical burst and packet switching can become a reality, more developments are needed in fast optical space switching technologies. The solution might not lie in a particular technology but in the combination of many, as recently demonstrated by a team from NTT and Fujitsu who used both MEMS and SOA switches to build a 10 Tb/s router that is potentially scalable to 100 Tb/s [5].

References

- [1] C. Ciminelli, F. Peluso, and M. N. Armenise, "2D guided-wave photonic band gap single and multiple cavity filters," in *Proceedings of 2005 IEEE/LEOS Workshop on Fibres and Optical Passive Components*, Taipei, Taiwan, pp. 404-409.
- [2] C. Ciminelli, F. Peluso, M. N. Armenise, and R. M. De la Rue, "Variable oblique incidence for tunability in a two-dimensional photonic-crystal guided-wave filter," *J Lightwave Technol.*, vol. 24, no. 1, pp. 470-476, Jan. 2006.
- [3] N. Dagli, *High-speed photonic devices*. New York: Taylor & Francis, 2007.
- [4] S.R. Sakamoto, C. Ozturk, B. Young Tae, J. Ko, and N. Dagli, "Low-loss substrate-removed (SURE) optical waveguides in GaAs-AlGaAs epitaxial layers embedded in organic polymers," *IEEE Photon. Tech. Lett.*, vol. 10, no. 7, pp. 985-987, Jul. 1998
- [5] K. Yonenaga, F. Inuzuka, S. Yongmei, Y. Aoki, K. Sone, A. Sano, K. Mori, T. Ono, Y. Kai, S. Yoshida, G. Nakagawa, Y. Sakai, A. Takada, and S. Kinoshita, "Demonstration of 10-Tbit/s multi-granularity optical cross-connect node toward 100-Tbit/s scalability," in *Conference on Optical Fiber Communication*, San Diego, CA, USA, 2009, pp. 1-3.

Appendix A

1-D Gaussian Beam Waist vs. Filter Angular Spectrum

A.1 Introduction

In chapter 5, an equation was introduced to compute the minimum $1/e$ Gaussian beam waist required to avoid distortion and to preserve the plane wave response of an integrated filter as a function of its clear angular bandwidth. This equation is:

$$\omega_o = \frac{2 \cdot 1.945 \cdot \lambda_o}{\pi \theta n_{eff}} \quad (\text{A.1})$$

where ω_o is the $1/e$ Gaussian beam waist, θ is the clear angular bandwidth of the filter in radians, and n_{eff} is the effective refractive index of the planar waveguide. This appendix presents the mathematical derivation that led to this equation.

A.2 Beam Waist and Angular Spectrum

The local angular (or plane wave) spectrum of any light beam cross-section is obtained by taking the Fourier transform of its spatial distribution at a point along its propagation path [1]:

$$A(k_x, k_y; z_o) = \int_{-\infty}^{\infty} \int_{-\infty}^{\infty} E(x, y; z_o) e^{-jk_x x - jk_y y} dx dy \quad (\text{A.2})$$

where $E(x,y;z_o)$ is the light spatial distribution at z_o , and k_x and k_y are angular frequencies along two different orthogonal axes. For the remaining calculations z_o is assumed to be the beam waist location for simplicity. However, in this mathematical derivation only the angular power distribution is considered. Thus, the light spatial distribution could be taken at any point on the beam path since the magnitude of the angular spectrum remains constant as the beam propagates; only the phase relationship between the different angular frequencies changes. The angular frequency components are related through:

$$k = \frac{2\pi}{\lambda_o} = \sqrt{k_x^2 + k_y^2 + k_z^2} \quad (\text{A.3})$$

where λ_o is the light wavelength in vacuum. Since light in integrated Fabry-Perot optical space switches is confined in the vertical direction by the planar waveguide, both the magnitude and phase of the vertical angular spectrum are preserved throughout the devices and the beam incident on the filter can be considered as one-dimensional. The light spatial distribution at the beam waist is given by:

$$E(x) = E_o e^{-\frac{x^2}{\omega_o^2}} \quad (\text{A.4})$$

and equation A.2 can be simplified to:

$$A(k_x) = E_o \int_{-\infty}^{\infty} e^{-\frac{x^2}{\omega_o^2}} e^{-jk_x x} dx. \quad (\text{A.5})$$

Using the following identity [2]:

$$\int_{-\infty}^{\infty} e^{-(ax^2+bx+c)} dx = \sqrt{\frac{\pi}{a}} e^{\frac{b^2-4ac}{4a}} \quad (\text{A.6})$$

equation A.5 can be integrated to obtain the angular spectrum amplitude:

$$A(k_x) = E_o \sqrt{\pi} \omega_o e^{-\frac{k_x^2 \omega_o^2}{4}}. \quad (\text{A.7})$$

Since the Fourier transform of a Gaussian function is also a Gaussian, it is possible to identify the $1/e$ point of the angular spectrum k_o as being equal to $2/\omega_o$.

Expressing k_o in radians and solving for ω_o provides an equation for the spatial beam waist required to get a given angular waist ϕ . The angular waist is the $1/e$ width of the Gaussian beam angular spectrum. Assuming the small angle approximation since the required angular spectra are narrow:

$$\frac{k_o}{2\pi} = \frac{\sin(\phi)}{\lambda_o / n_{eff}} \Rightarrow k_o = \frac{2\pi\phi}{\lambda_o} n_{eff} \quad (\text{A.8})$$

$$k_o = \frac{2\pi\phi n_{eff}}{\lambda_o} = \frac{2}{\omega_o} \Rightarrow \omega_o = \frac{\lambda_o}{\pi\phi n_{eff}} \quad (\text{A.9})$$

A.3 Fraction of Power in an Given Angular Range

Finding the amount of power in a given angular range is necessary to establish a limit on the lost that can be suffered before the beam is severally distorted. This is similar to the fraction of power that must be contained within an aperture to prevent modification to the waist size and location of a beam due to clipping. In the present case, the angular aperture is defined as the angular clear bandwidth of the filter (i.e. the angular range with over 90 % transmission). The procedure to find the power contained within a given angular range is similar to the derivation for the power enclosed in a circle described in [3] except than the beam here is one-dimensional. The first step is to express the angular distribution in terms of intensity:

$$I(k_x) = (A(k_x))^2 = E_o^2 \pi \omega_o^2 e^{-\frac{k_x^2 \omega_o^2}{2}} \quad (\text{A.10})$$

The total power P is:

$$P = \int_{-\infty}^{\infty} I(k_x) dk_x = \sqrt{2\pi^3} E_o^2 \pi \omega_o^2 \quad (\text{A.11})$$

and the fraction of power within an angular range $\pm k_a$ is:

$$\frac{1}{P} \int_{-k_a}^{k_a} I(k_x) dk_x = erf\left(\frac{\omega_o k_a}{\sqrt{2}}\right) \quad (\text{A.11})$$

where $erf()$ is the error function. To find the spatial beam waist for which 99.99% of the angular spectrum power is contained within the angular range $\pm k_a$, the expression $A k_o$ is substituted for k_a in the right hand side of equation A.11 and solved to determine the value of A . The result is $A = 1.945$. Using this value and recognising that the clear angular bandwidth of the filter $\theta = 2 (A k_o)$, equation A.9 becomes:

$$\omega_o = \frac{2 \cdot 1.945 \cdot \lambda_o}{\pi \theta n_{eff}} \quad (\text{A.12})$$

which is the equation reported in chapter 5.

References

- [1] M. Born and E. Wolf, *Principles of optics: electromagnetic theory of propagation, interference and diffraction of light*, 7th expanded ed. New York: Cambridge University Press, 1999.
- [2] M. R. Spiegel and J. Liu, *Mathematical handbook of formulas and tables*. New York: McGraw-Hill, 1999.
- [3] B. E. A. Saleh and M. C. Teich, *Fundamentals of photonics*, 2nd ed. Hoboken, NJ: Wiley-Interscience, 2007.

Appendix B

Fabrication Process

B.1 Introduction

The fabrication process was developed in the McGill microfabrication laboratory. Except for the growth of the epitaxial layers, which was done at the Canadian Photonics Fabrication Centre, all processing steps were performed at McGill. No processes specific to GaAs existed in the microfabrication laboratory at the beginning of this project. Cleaning procedures, photolithographic exposures, and metal sputtering recipes were adapted from work done with silicon wafers. However, the dry etch recipe was conceived from begin to end for the fabrication of integrated Fabry-Perot switches.

This appendix is divided in two sections. The first one presents the layout of the photomask used for the fabrication of the prototypes and discusses their salient features. The second one describes each steps of the fabrication process in details, starting with wafer cleaving all the way to aluminum patterning.

B.2 Photomasks

The fabrication of the prototypes requires four photomasks and each of them were obtained from a different vendor since they all had different tolerance requirements. A positive photoresist was used in the fabrication process, and thus the features to be etched into the samples appear as transparent areas (i.e. without chrome) on the masks. This means that the polygons shown in the following

figures represent areas without chrome. All masks were created with AutoCAD 2002 using a custom library of functions written in the ARX language. The AutoCAD files were converted to GDSII format before being sent to the mask manufacturers.

The first mask was used for edge bead removal. Because of their small size (18 mm x 18 mm), the samples had to be coated with photoresist on the manual coater. To remove most of the edge bead, they were exposed with a mask consisting of a 9 mm x 9 mm square filled with chrome and of small alignment brackets matching the samples corners. Since the precision of the dimensions of this mask features was not important, this mask was ordered from Fineline Imaging, which transfers patterns printed with a plotter onto chrome masks.

The next mask used in the fabrication process has the patterns defining the filter and collimating mirrors. It consists of 16 cells, each having a filter located between two collimating mirrors, except for one cell which has only collimating mirrors. The cells are arranged in a 4x4 layout and the two central rows are shown in Fig. B.1. Only two consecutive columns can be fabricated on a sample. Therefore, multiple copies of the alignment pattern used with the waveguide and electrode masks were put on the filter mask in order to accommodate all column combinations possible. Furthermore, since the filter mask is the first one used to create features on the samples, rough alignment patterns were drawn on it to allow the positioning of the mask with respect to the photoresist square defined during the edge bead removal. The collimating mirrors are identical in each cell but the filters have dimensions varying between ± 400 nm of the design values. Any width removed/added to a trench was added/removed to the neighbouring cavities. The variations in the dimensions of the filters are provided in Table B.1. Having multiple devices with slightly different dimensions helps to mitigate errors caused by the fabrication process since at the end of the fabrication run the implementation closest to the desired design can be selected. Because the filter mask contains the features with the most stringent tolerances, it was ordered from

a commercial manufacturer (Compugraphics) that guaranteed a critical dimension tolerance of ± 30 nm. Fig. B.2 shows the content of one cell with the patterns of the filter and channel waveguide masks. The pattern of the filter mask is shown in green whereas the one of the channel waveguide mask is in red.

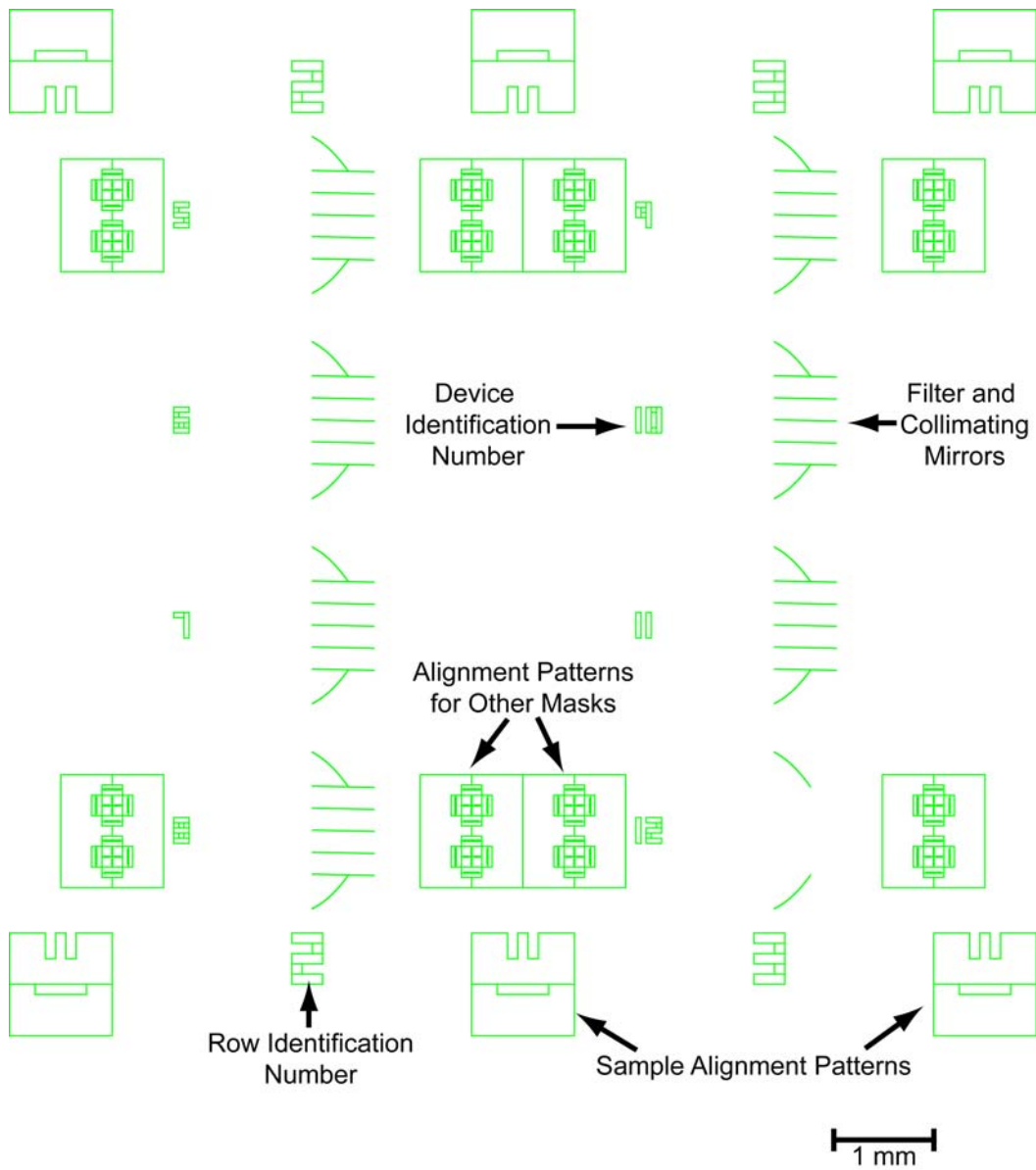


Fig. B.1: Schematic showing the two central rows of the filters photomask.

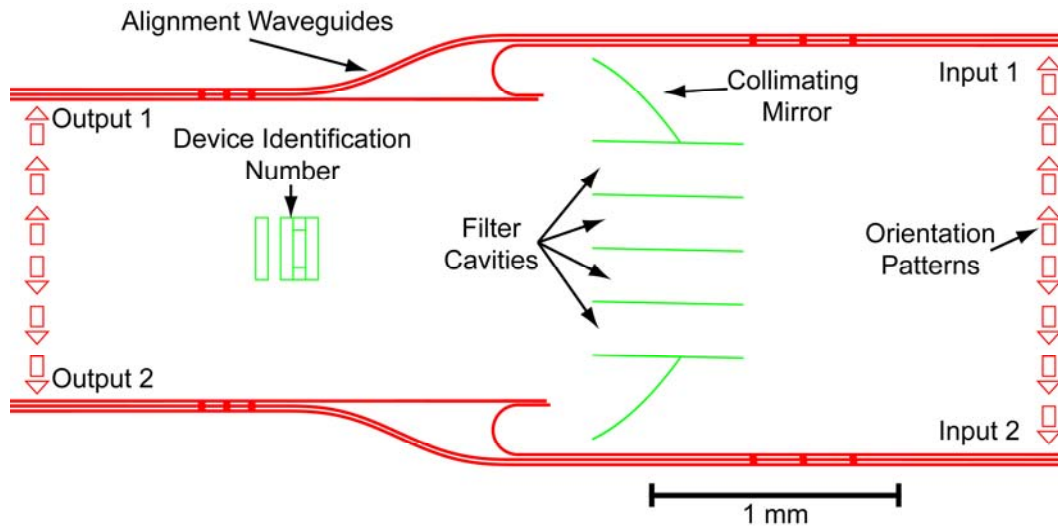


Fig. B.2: Schematic showing the filter (in green) and channel waveguide (in red) mask patterns for a single device.

Table B.1: Variations from the design values of the devices on the filter mask

Die #	Variation (nm)						
1	-400	5	-120	9	-40	13	400
2	-320	6	-80	10	0	14	320
3	-240	7	80	11	40	15	240
4	-160	8	120	12	N/A	16	160

The channel waveguides were defined by etching $2.0\ \mu\text{m}$ wide trenches on each side of a $3.0\ \mu\text{m}$ ridge and they were separated by $20\ \mu\text{m}$ (centre to centre) at the die edges. The 180° bend in the input waveguides has a radius of curvature of $100\ \mu\text{m}$. Six sets of three chevrons were etched between the channel waveguides to ensure that no light is guided in these regions. The waveguide mask also included a set eight of waveguides with different lengths to measure propagation loss below the switch waveguides. Another set of seven waveguides with 180° bends having radii varying between $20\ \mu\text{m}$ to $200\ \mu\text{m}$ was added to the mask to evaluate bending losses. The waveguide mask has 12 copies of the pattern shown in red in Fig. B.2 lay out in three columns of four rows each. All patterns are identical except for the one at the bottom of the third column. This pattern was

designed to work with the device that does not have a filter and thus the position of its output waveguides was adjusted to match the position of the output waists for this case. Depending on the filters that had been etched in the sample, either the first two columns with eight identical patterns was aligned with the sample or the last two columns were used if the sample had the device without a filter. The waveguide mask was written with an e-beam writer at INRS in Varennes on a best effort basis.

The last mask was used to pattern the aluminum layer modeling the electrodes on the optical prototypes. The electrode pattern is shown in blue in Fig. B.3. This pattern was repeated eight times and lay out in two columns of four rows. All patterns were identical. This mask was written with a laser plotter at the Université de Sherbrooke.

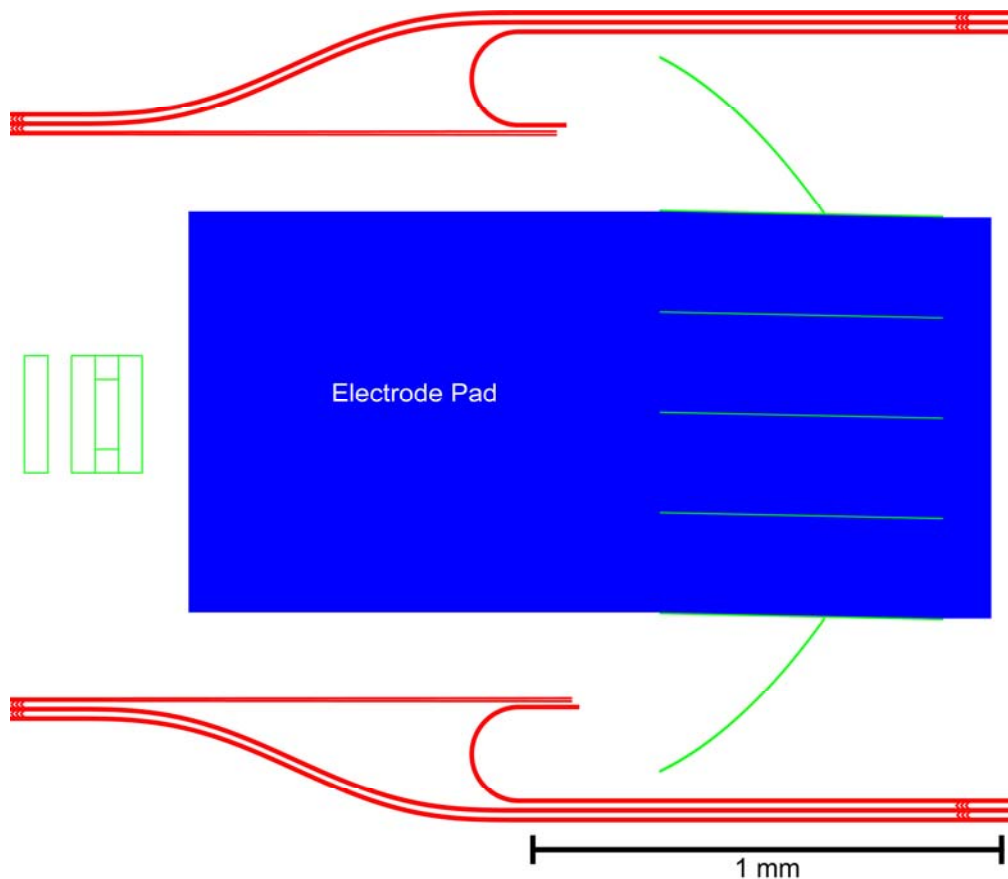


Fig. B.3: Schematic showing the electrode (in blue), channel waveguides (in red), and filter mask pattern for a single device.

The alignment marks shown in Fig. B.4 were used to overlay the photomasks described above. It consists of a double cross pattern for coarse alignment and of $0.5\ \mu\text{m}$ and $0.2\ \mu\text{m}$ Vernier scales for fine alignment. Unfortunately, the $0.2\ \mu\text{m}$ Vernier scales were hard to resolve with the 10X objectives mounted on the aligner and only the $0.5\ \mu\text{m}$ ones were used. Copies of the marks shown below were put on each corner of the samples to ensure proper angular alignment.

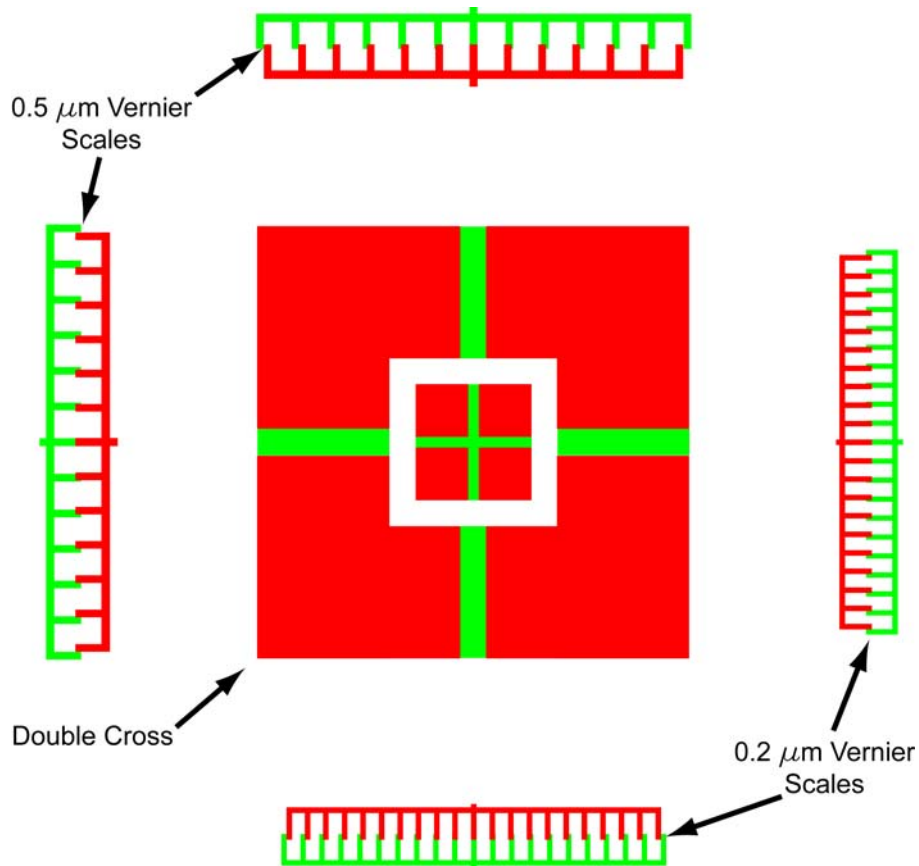


Fig. B.4: Schematic of the alignment marks used to overlay the photomasks. The features in green are on the filter mask while those in red were on the channel waveguides and electrodes masks.

B.3 Fabrication Process

The equipment available in the McGill microfabrication laboratory at the time of fabrication required that two major adjustments be made to state-of-the-art GaAs fabrication processes described in the literature [1-3]. First, SiO_2 is usually used as a hard mask, especially when deep etching is required. Since plasma-enhanced chemical vapour deposition (PECVD) was not available, hard bake photoresist was used instead. The other change concerned the reactive ion etching gas. The only gas available that could etch GaAs was Cl_2 . Although Cl_2 provides high etch rates, SiCl_4 is usually preferred because it can achieve smoother surfaces and that a polymerisation reaction occurring during etching improves the verticality of deep features. Nevertheless, through extensive experimentation smooth and vertical features were obtained with an etch rate greater than $2 \mu\text{m}/\text{minutes}$. Fig. B.5 shows cross-sections of features fabricated during the process development illustrating the depth, vertically, and quality achieved with the etch recipe.

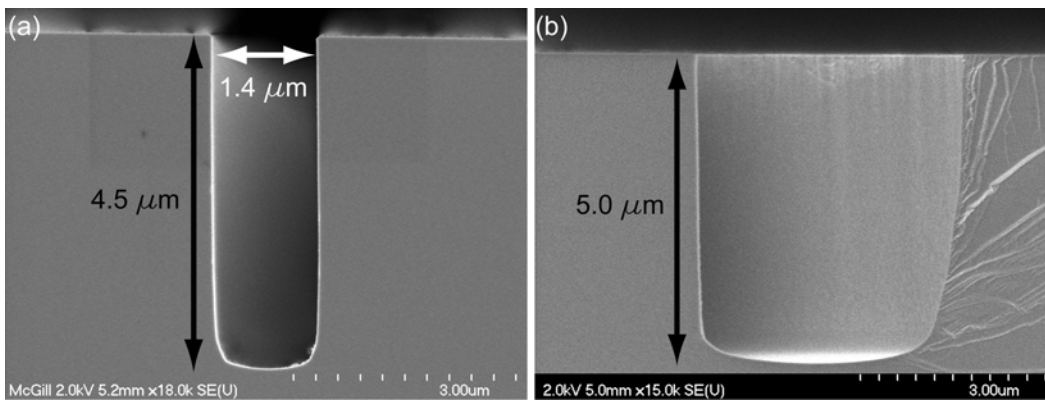


Fig. B.5: Scanning electron micrographs showing (a) the cross-section of a filter mirror and (b) that of a collimating mirror. Because of the collimating mirror curvature, it is possible to see how smooth the trench walls are.

The small sample size also limited the equipment available because the microfabrication laboratory was built to process 6" silicon wafers. Thus, the projection stepper and the automatic coater could not be used. To fit in the reactive ion etcher, the samples were fixed to a 6" silicon wafer with a thermally conductive paste. The etch process is sensitive to residue from SF₆ glass etches and the vacuum chamber has to be cleaned before working with GaAs if SF₆ glass has been processed previously. The full fabrication process is described below. For steps that are repeated, only the parameters that are changed are indicated in the subsequent iterations.

References

- [1] M. J. Madou, *Fundamentals of microfabrication: the science of miniaturization*, 2nd ed. London: CRC Press, 2002.
- [2] S. J. Pearton, F. Ren, T. R. Fullowan, A. Katz, W. S. Hobson, U. K. Chakrabarti, and C. R. Abernathy, "Plasma etching of III-V semiconductor thin films," *Mater Chem Phys*, vol. 32, no. 3, pp. 215-234, Oct. 1992.
- [3] R. E. Williams, *Gallium arsenide processing techniques*, Dedham, MA: Artech House, 1984.

Process Step	Description																																						
Cleaving	The 3" wafers were manually cleaved in 9 squares of 18 mm on the side after being scribed with a diamond pen.																																						
SiO ₂ Removal	A 500 nm layer of SiO ₂ was deposited by PECVD at the CPFC laboratory after epitaxial growth to protect the wafers. It was removed by immersing the samples in a 10% hydrofluoric (HF) acid solution for 20 minutes.																																						
Cleaning	10 minutes immersion in acetone in an ultrasonic bath followed by another 10 minutes in isopropyl alcohol (IPA), also in the ultrasonic bath. The samples were rinsed in DI water and dried with an air gun. Finally, the samples were put 10 minutes in the microwave oxygen plasma asher at 350 W.																																						
Photoresist Coating	Spin coated the samples with 1.4 μm of Shipley 1813 photoresist on the manual coater (Bidtec). The coater program was: <table border="1" data-bbox="630 680 1170 835"> <thead> <tr> <th>Step</th> <th>Speed (rpm)</th> <th>Acceleration (s)</th> <th>Time (s)</th> </tr> </thead> <tbody> <tr> <td>1</td> <td>200</td> <td>0.1</td> <td>5</td> </tr> <tr> <td>2</td> <td>3950</td> <td>0.3</td> <td>30</td> </tr> <tr> <td>3</td> <td>0</td> <td>0.5</td> <td>1</td> </tr> </tbody> </table>	Step	Speed (rpm)	Acceleration (s)	Time (s)	1	200	0.1	5	2	3950	0.3	30	3	0	0.5	1																						
Step	Speed (rpm)	Acceleration (s)	Time (s)																																				
1	200	0.1	5																																				
2	3950	0.3	30																																				
3	0	0.5	1																																				
Soft bake	Heated the samples with a hot plate at 115° C for 60 seconds.																																						
Edge Bead Removal (EBR)	Exposed the samples with the EBR mask on the EVG contact aligner. Set the power to 100 mJ in constant power mode. Developed for 40 seconds with the automatic coater (Site Service) without baking. Manually swabbed the samples edges with acetone.																																						
Filter Mask Exposition	Exposed the samples to 55 mJ with the filter mask.																																						
Post Exposure Bake (PEB)	Baked the samples for 80 seconds on a hot plate at 115° C.																																						
Development	Developed for 40 seconds and baked 90 seconds at 90° C on the automatic coater hot plate.																																						
Hard bake	Baked the samples for 20 minutes on a hot plate at 90° C.																																						
Reactive Ion Etching (RIE)	Etched with the Applied Material 5000 in chamber C. The etch program was: <table border="1" data-bbox="704 1245 1097 1860"> <thead> <tr> <th>Step</th> <th>Variable</th> <th>Values</th> </tr> </thead> <tbody> <tr> <td rowspan="5">1</td> <td>Time</td> <td>15 sec</td> </tr> <tr> <td>Power</td> <td>0 W</td> </tr> <tr> <td>Magnetic Field</td> <td>0 Gauss</td> </tr> <tr> <td>Pressure</td> <td>60 mTorr</td> </tr> <tr> <td>Gas</td> <td>60 Cl₂: 60 Ar</td> </tr> <tr> <td rowspan="4">2</td> <td>Time</td> <td>130 sec</td> </tr> <tr> <td>Power</td> <td>235 W</td> </tr> <tr> <td>Magnetic Field</td> <td>70 Gauss</td> </tr> <tr> <td>Pressure</td> <td>60 mTorr</td> </tr> <tr> <td rowspan="4">3</td> <td>Gas</td> <td>60 Cl₂: 60 Ar</td> </tr> <tr> <td>Time</td> <td>10 sec</td> </tr> <tr> <td>Power</td> <td>50 W</td> </tr> <tr> <td>Magnetic Field</td> <td>70 Gauss</td> </tr> <tr> <td></td> <td>Pressure</td> <td>Full Throttle</td> </tr> <tr> <td></td> <td>Gas</td> <td>60 Ar</td> </tr> </tbody> </table>	Step	Variable	Values	1	Time	15 sec	Power	0 W	Magnetic Field	0 Gauss	Pressure	60 mTorr	Gas	60 Cl ₂ : 60 Ar	2	Time	130 sec	Power	235 W	Magnetic Field	70 Gauss	Pressure	60 mTorr	3	Gas	60 Cl ₂ : 60 Ar	Time	10 sec	Power	50 W	Magnetic Field	70 Gauss		Pressure	Full Throttle		Gas	60 Ar
Step	Variable	Values																																					
1	Time	15 sec																																					
	Power	0 W																																					
	Magnetic Field	0 Gauss																																					
	Pressure	60 mTorr																																					
	Gas	60 Cl ₂ : 60 Ar																																					
2	Time	130 sec																																					
	Power	235 W																																					
	Magnetic Field	70 Gauss																																					
	Pressure	60 mTorr																																					
3	Gas	60 Cl ₂ : 60 Ar																																					
	Time	10 sec																																					
	Power	50 W																																					
	Magnetic Field	70 Gauss																																					
	Pressure	Full Throttle																																					
	Gas	60 Ar																																					

Process Step	Description										
Cleaning	See above										
Native Oxide Removal	The samples were dipped 60 seconds in 10 % HF to remove the native oxide.										
Photoresist Coating and EBR	See above										
Waveguide Mask Exposition	Exposed the samples to 60 mJ with the waveguide mask.										
PEB	See above										
Development	Developed for 45 seconds and baked 90 seconds at 90° C on the automatic coater hot plate.										
Hard Bake	See above										
RIE	The time in step 2 was changed to 50 seconds.										
Cleaning and Native Oxide Removal	See above										
Photoresist Coating	Changed the speed in step 2 to 1600 rpm.										
Soft bake and EBR	See above										
Electrode Mask Exposition	Exposed the samples to 70 mJ with the electrode mask.										
PEB	See above										
Toluene Dip	Immersed the samples in toluene for 10 minutes.										
Development	Developed for 60 seconds without baking.										
	Sputtering of 125 nm of aluminum. The program for the MRC sputter was:										
	<table border="1"> <thead> <tr> <th>Variable</th> <th>Value</th> </tr> </thead> <tbody> <tr> <td>Power</td> <td>1.15 kW</td> </tr> <tr> <td>Pressure</td> <td>22.5 mTorr</td> </tr> <tr> <td>Speed</td> <td>13 cm/min</td> </tr> <tr> <td># of scans</td> <td>2</td> </tr> </tbody> </table>	Variable	Value	Power	1.15 kW	Pressure	22.5 mTorr	Speed	13 cm/min	# of scans	2
Variable	Value										
Power	1.15 kW										
Pressure	22.5 mTorr										
Speed	13 cm/min										
# of scans	2										
Aluminum Sputtering											
Liftoff	Overnight immersion in acetone										
Cleaning	See above										
Photoresist Coating	Photoresist coat used as a protective layer during aluminum sputtering on the samples back sides. Changed the speed in step 2 to 1600 rpm.										
Soft bake	See above										
Aluminum Sputtering	Deposition of 250 nm of aluminum on the back of the samples. The number of scans was increased to 4.										
Cleaning	See above										